UNIVERSITÀ
DEGLI STUDI
FIRENZE

DOTTORATO DI RICERCA IN SCIENZE CHIMICHE

CICLO XXXI

COORDINATORE Prof. BAGLIONI PIERO

LINEAR AND NONLINEAR OPTICAL TECHNIQUES AND NOVEL PHOTOACOUSTIC MODALITIES FOR THE NON-INVASIVE ANALYSIS AND MONITORING OF ARTWORKS.

Settore Scientifico Disciplinare FIS/07

Dottorando
Dott. *Dal Fovo Alice*

Tutore
Prof. *Fontana Raffaella*

Coordinatore
Prof. *Baglioni Piero*

Anni 2015/2018

To my family

Index

Abstract

The diagnosis of Cultural Heritage objects relies on several analytical modalities, which have proven significantly useful for the chemical and physical characterization of pictorial materials. The documentation and monitoring of artworks turns relevant especially in the context of irreversible restoring operations, like the cleaning process. In order to preserve the artworks' integrity, techniques not involving direct contact, damaging radiation, sampling or pre-treatments are generally preferred. However, the presence of high scattering pictorial materials may hamper the visualization of the internal structures by means of non-invasive established modalities, like Optical Coherence Tomography (OCT), thus making the in-depth analysis of paintings a challenge still open.

The aim of this research was to overcome the limits of the currently applied methodologies through the combined application of novel and traditional non-invasive techniques. Specifically, the potential of nonlinear optical microscopies (Multi-Photon Excitation Fluorescence – MPEF; Second and Third Harmonic Generation – SHG, THG; Fluorescence Lifetime Imaging Microscopy – FLIM) and photoacoustic modalities (PhotoAcoustic Signal Attenuation Analysis – PAcSAA; Near Infrared - PhotoAcoustic Imaging – NIR-PAI) was investigated, and a new scientific method for the non-invasive in-depth analysis of painted artworks was defined. It was then demonstrated that the synergic application of several analytical methodologies (Fibre Optics Reflectance Spectroscopy – FORS; Laser Induced Fluorescence – LIF; Vis-NIR Scanning Multispectral Reflectography – Vis-NIR SMR; micro-Raman Spectroscopy; Optical Coherence Tomography – OCT), may provide chemical and physical information on a variety of artistic materials – i.e. painting layers, varnishes, glues, wood – without endangering the integrity of the artwork.

Preface

Today, the diagnosis of Cultural Heritage (CH) objects involves several analytical techniques, which are applied for the chemical and physical characterization of the constituting materials, as well as for the monitoring of restoring operations. Being the preservation of the object's integrity a priority in artworks conservation, non-invasive techniques are generally applied to avoid any damage. However, data obtained by means of such methodologies is not always exhaustive or completely unambiguous. There are also cases in which non-invasive techniques do not provide the information requested, specifically in presence of highly scattering materials, which may significantly reduce the penetration of the radiation probe. Concerning conservation treatments and studies of authenticity in paintings, though, the in-depth analysis turns definitely relevant – e.g. for the detection of pictorial detachments, internal discontinuities and, especially, for the identification and quantification of foreign materials. Moreover, the knowledge of the chemical composition, as well as the visualization of the objects' stratigraphy, may provide a considerable support in the context of restoring operations.

When the superficial layer (generically called *patina*) infringes the ethical standards of art conservation, compromising the legibility of the painted surface and/or not fulfilling its protective/aesthetic function anymore, it is generally thinned or selectively removed. This delicate and irreversible operation, called *cleaning*, is often performed on pictorial retouching covering the historical painting, or on aged varnishes, which have lost transparency and elasticity. The cleaning may greatly benefit from the monitoring of the whole restoring process, providing the measurement of the in-depth extent of the unwanted materials before, during and after their selective removal. Such information becomes essential for future conservation treatments, as well as for not compromising further historical interpretations. At present, few techniques

provide insight into paintings' internal structure, most of them based on sampling. However, non-invasive techniques could provide similar in-depth information without endangering the artworks integrity.

In the last decades, a non-invasive optical technique, originally developed for ophthalmology applications, namely Optical Coherence Tomography (OCT), has been successfully applied to painting in-depth analysis. Providing high-resolution cross-sectional imaging of semi-transparent objects, OCT has proven particularly effective for the stratigraphic visualization of varnish layers, in some cases enabling also the discrimination between aged and new varnish.[1] Furthermore, it was demonstrated that, by coupling confocal microscope optics with an OCT setup, it is feasible to focalize the beam inside the sample rather than on the outer surface, thus overcoming problems related to highly reflecting varnishes.[2] However, in-depth imaging of paint layers with OCT is at present restricted to specific cases, namely low scattering pictorial media with high degree of transparency to the radiation used (usually, the Near Infrared – NIR-spectral range).[3]

Another method recently tested for the 3D imaging of paintings is Nuclear Magnetic Resonance (NMR). A breakthrough for its application in the Cultural Heritage field has been the development of single-sided NMR sensors,[4] which combine open magnets and surface Radio Frequency (RF) coils to generate a magnetic field inside the object under investigation. *In situ* experiments were performed with a single-sided NMR sensor by spanning several millimetres in depth with a resolution better than 10 μm,[5] providing axial profiles of paintings. Nevertheless, despite the effectiveness of some applications, NMR presents some limits related to signal detection and lack of homogeneity in the magnetic field generated by the magnets and coils.

In the last years, THz radiation has been tested for the non-invasive inspection of paintings. The high penetration capability (0.1 – 10 THz) through a wide

variety of pictorial materials, usually opaque to both visible and infrared wavelengths,[6] makes non-ionizing THz radiation an effective probe for bulk analysis. In 2009, Terahertz Time-Domain Spectroscopy (THz-TDS) was applied in reflection mode for in-depth imaging of canvas paintings.[7] The necessity for complex and expensive instrumentations, often including femtosecond (fs = 10^{-15} s) lasers, lock-in amplifiers and THz spectrometers, represents one of the main drawbacks of THz set-ups. Furthermore, the relative low axial resolution achievable with THz radiation makes this method unfitting for in-depth measurement in pictorial layers.

In more recent years, Nonlinear Optical Microscopies (NLOM), including Multi-Photon Excitation Fluorescence (MPEF), Second and Third Harmonic Generation (SHG and THG), and Fluorescence Lifetime Imaging Microscopy (FLIM), have been tested for non-invasive in-depth analysis of artworks. NLOM are cutting-edge methodologies based on nonlinear optical processes, in which molecules simultaneously interact with two or more photons within the same quantum event. Such phenomena may be observed when a given material is excited by a tightly-focused fs-pulsed laser, propagating through a high numerical aperture microscope objective, enabling both good penetration capability and micrometric axial resolution. NLOM techniques[6,8-15] may provide compositional and structural information based on the detection of fluorophores (by MPEF),[9] crystalline or highly organized structures without inversion symmetry (by SHG)[10] or local differences in refractive index and dispersion, i.e. interfaces (by THG).[6] In CH diagnosis, NLOM has been applied for 3D imaging of protective layers, in support of the cleaning operation performed on natural and synthetic varnishes. It was demonstrated that NLOM makes feasible the in-depth monitoring of varnish degradation due to aging[11] or laser ablation.[12] Cross-section of pictorial layers were obtained through the application of femtosecond pump-probe microscopy in the nonlinear

modality,[13,14] and MPEF imaging has been applied for the determination of thickness of egg-tempera layers.[15] A recent work has shown the comparison between OCT and NLOM for the study of painting materials.[8]

Based on these antecedents, the main observed limitation of NLOM imaging seems to be related to the presence of highly scattering and/or absorbing media (pigments), which obstruct the detection of the NLOM signal. Nevertheless, the potential of nonlinear modalities in probing pictorial materials has not been fully investigated. The systematic application of NLOM on several painting materials, using different devices, may provide the information missing.

The aim of this PhD project was to define a new methodology for the scientific non-invasive analysis of paintings and the monitoring of restoring operations, based on the multi-modal application of several techniques on a number of pictorial materials. The research involved the systematic testing of novel non-invasive modalities, based on nonlinear and photoacoustic processes.

This work was carried on at the Istituto Nazionale di Ottica (INO) Consiglio Nazionale delle Ricerche (CNR),[i] and is part of the wider European IPERION CH Project (Integrated Platform for the European Research Infrastructure ON Cultural Heritage - H2020 Research Infrastructure Program on Cultural Heritage (GA 654028, WP6), which aims at evaluating the state of the art of NLOM in Cultural Heritage applications and assessing the capabilities of this family of techniques for characterizing and imaging composite multi-layer structures in CH samples/objects.

The first year was focused on testing the potential of NLO-imaging in the non-destructive determination of thickness and composition of multi-layer painted mock-ups. In this context, MPEF, SHG, THG, and FLIM were applied using a custom-made laser scanning microscope.[ii] Measurements were performed on

[i] R. Fontana, Cultural Heritage (CH) Group.

[ii] R. Cicchi, F. Quercioli, R. Mercatelli (CNR-INO).

specifically designed multi-layered samples (egg-tempera paints covered with protective materials and laid on a wooden support). These samples were selected for round robin tests in the framework of IPERION Project (WP6) and distributed among the project's partners for NL analysis, by means of different operating systems and modalities. The reliability of NL results was evaluated by comparison with UV-Vis stratigraphic analysis[iii] on micro-samples, and NL measurements were complemented with other well-established techniques, such as X-Ray Fluorescence (XRF), Optical Coherence Tomography (OCT), confocal microscopy, laser scanning micro-profilometry, Fibre Optics Reflectance Spectroscopy (FORS), and Scanning Multispectral Reflectography (SMR) in the visible and near-infrared region. During these primary tests, some limits in the visualization of the painting internal structure through NL imaging were encountered, possibly due to the intense scattering of the paint layer and to auto-absorption of the emitted fluorescence. The first observations paved the way for further analyses, which were carried out during the second year of research, by using different NL setups on an enlarged number of samples, in collaboration with foreign research laboratories. A two-month research period was spent at the Instituto de Quimica Fisica Rocasolano (IQFR), in collaboration with the Instituto de Estructura de la Materia (IEM), Consejo Superior de Investigaciones Cientificas (CSIC),[iv] Madrid. For this study, a set of acrylic tempera paints laid on glass supports was prepared and measured using a multi-analytical approach, involving several laser-based techniques, such as MPEF,[9] one-photon Laser Induced Fluorescence (LIF),[16] micro-Raman spectroscopy,[16] and Laser Induced Breakdown Spectroscopy (LIBS).[17] MPEF was specifically applied for the evaluation of paints thickness, and results were compared with OCT measurements, showing a good

[iii] G. Lanterna, Opificio delle Pietre Dure, Florence.
[iv] M. Castllejo, M. Oujja, M. Sanz, A. Martinez Hernàndez (IQFR-CSIC), M. V. Cañamares (IEM-CSIC).

correspondence in most cases. Based on those results, a first approach for the correct interpretation of the MPEF response was defined.[18]

In collaboration with the Institute of Electronic Structure and Laser, Foundation for Research and Technology Hellas (IESL-FORTH),[v] another research aimed at testing a new method for the evaluation of paint layers thickness was carried on, based on the detection of the attenuated acoustic waves generated by the material after light absorption. Results obtained on acrylic paints through the application of the new method, named PhotoAcoustic Signal Attenuation Analysis (PAcSAA),[19] were compared with the previously performed OCT, showing excellent agreement.

During the third year, the photoacoustic effect was further tested in the framework of H2020 Laserlab Europe – Transnational Access (EC-GA 654148), in collaboration with IESL-FORTH. The main objective was to investigate further the potential of both Photo-Acoustic Signal Attenuation Analysis (PAcSAA)[iv] and Nonlinear Optical Microscopy (NLOM),[vi] for the non-destructive diagnosis of paintings. The study involved a set of acrylic-tempera samples on canvas and glass, composed of layers of different thickness previously characterized by means of non-invasive optical techniques at CNR-INO. An imaging modality, called PhotoAcoustic Signal Attenuation Imaging (PAcSAI)[20], combined with near infrared photoacoustic imaging, was developed for both the acquisition of cross-sectional information of painted layers and the visualization of drawings underneath the painted surface, by using the fundamental and second harmonic wavelength of a Nd:YAG laser source. During the same project, MPEF was applied on acrylic paints covered with a varnish (mastic) layer, aiming at testing nonlinear imaging on multi-layer samples.

[v] G. Tseverelakis, G. Zacharakis, In-vivo imaging Laboratory (IESL-FORTH).
[vi] V. Tsafas, G. Filippidis, Nonlinear microscopy Laboratory (IESL-FORTH).

Further nonlinear measurements were carried on at CNR-INO with a new version of the custom-made microscope equipped with a tunable fs-laser. Measurements were systematically performed on a larger set of samples, including the above mentioned acrylic paints, egg-tempera paints, several protective materials, and wood. Taking advantage of the conspicuous dataset, a new approach for the interpretation of nonlinear fluorescence responses, named Second Derivative Spline Distance (2DSD), was defined. 2DSD is based on a purposely developed algorithm, which accounts for the uncertainties deriving from refractive index variations and the instrumental specifications – i.e. objective numerical aperture. The reliability of MPEF results were assessed by comparison with the previously performed Optical Coherent Tomography, showing optimal consistency. Specifically, in case of highly scattering/absorbing paints, the estimation of layers' thickness was not possible by means of OCT, except when the upper surface of the glass/canvas support was taken as reference. In-depth measurements were instead feasible with MPEF, regardless the visualization of the interface paint/support, thus demonstrating the possibility to overcome the limits of OCT in the visualization of opaque materials.

Contents

The present thesis is organized in three parts:

PART 1: A description of the physical principles of nonlinear optical processes (second- and third- order polarizations) is reported, with a focus on one- and multi-photon excitation fluorescence, followed by a brief description of the basic instrumentation commonly used for nonlinear microscopy. A literature overview of the main applications in Cultural Heritage science is then reported, ranging from the analysis on protective materials, binders and overpaintings

(related to the monitoring of the cleaning process), to the visualization of wood microstructures in wooden objects and the analysis of degradation in metal-based artefacts. At the end, the last findings on the possible damage induced by high-intensity fs-lasers used in nonlinear optical microscopies, and specifically on painting layers, are presented.

PART 2: The results of the application of nonlinear modalities on a variety of materials used in paintings are shown. Each section presents a description of the analysed materials and the instruments used. The first section concerns the application of third harmonic generation for the stratigraphic analysis of several materials used as *protectives* or *consolidants* (varnishes and adhesives, in comparison with OCT). The second section is focused on the micro-analysis of different wood species (used as paintings substrates or in wooden artistic objects), through the combined application of MPEF and SHG in imaging modality. In the third section, a systematic study on painting layers composed of a variety of pigments and binders is reported, based on a multi-analytical approach involving multi-photon excitation fluorescence and a number of optical linear techniques. The method 2SDS for the interpretation of MPEF measurements is also described in comparison with OCT analysis.

PART 3: The photoacoustic method is introduced with a description of the physical effect. Results obtained through PAcSAA, PAcSAI and NIR-PAI are presented and discussed in comparison with OCT.

Finally, the conclusions of the whole research project are drawn, highlighting the advantages and drawbacks of the new methodologies, as well as the perspectives for future studies.

References

[1] H. Liang, M. G. Cid, R. G. Cucu, G. M. Dobre, A. Gh. Podoleanu, *En-face* optical coherence tomography - a novel application of non-invasive imaging to art conservation, Opt. Express 13, 16, 6133 (2005).

[2] R. Fontana, A. Dal Fovo, J. Striova, L. Pezzati, E. Pampaloni, M. Raffaelli, M. Barucci, Application of non-invasive optical monitoring methodologies to follow and record painting cleaning processes, Appl. Phys. A 121, 957–966 (2015) doi:10.1007/s00339-015-9505-5.

[3] P. Targowski, M. Gòra, M. Wojtkowski, Optical Coherence Tomography for Artwork Diagnostics, Laser Chemistry (2006), ID 35373, 11 pages (2006) doi:10.1155/2006/35373.

[4] B. Blümich, J. Perlo, F. Casanova, Mobile single-sided NMR, Prog. Nucl. Magn. Reson. Spectrosc., 52, 197-269 (2008).

[5] F. Presciutti, J. Perlo, F. Casanova, S. Glöggler, C. Miliani, B. Blümich, B. G. Brunetti, A. Sgamellotti, Noninvasive nuclear magnetic resonance profiling of painting layers, Appl. Phys. Lett. 93, 033505 (2008) doi:10.1063/1.2963026.

[6] G. Filippidis, M. Massaouti, A. Selimis, E.J. Gualda, J. M. Manceau, S. Tzortzakis, Nonlinear imaging and THz diagnostic tools in the service of cultural heritage, Appl. Phys. A 106(2), 257-263 (2012) doi:10.1007/s00339-011-6691-7.

[7] A. J. L. Adam, P. C. M. Planken, S. Meloni, J. Dik, TeraHertz imaging of hidden paint layers on canvas, Opt. Express 17(5), 3407-3416 (2009).

[8] H. Liang, M. Mari, C. S. Cheung, S. Kogou, P. Johnson, and G. Filippidis, Optical coherence tomography and non-linear microscopy for paintings – a study of the complementary capabilities and laser degradation effects, Opt. Express, 25, 19640-19653 (2017).

[9] G. Filippidis, G. J. Tserevelakis, A. Selimis, C. Fotakis, Nonlinear imaging techniques as non-destructive, high-resolution diagnostic tools for cultural heritage studies, Appl. Phys. A, 118, 417–423 (2015), doi:10.1007/s00339-014-8357-8.

[10] G. Latour, J. P. Echard, M. Didier, M.C. Schanne-Klein, *In situ* 3D characterization of historical coatings and wood using multimodal nonlinear optical microscopy**,** Opt. Express, 20, 24623–24635 (2012), doi:10.1364/OE.20.024623.

[11] G. Filippidis, M. Mari, L. Kelegkouri, A. Philippidis, A. Selimis, K. Melessanaki, M. Sygletou, C. Fotakis, Assessment of In-Depth Degradation of Artificially Aged Triterpenoid

Paint Varnishes Using Nonlinear Microscopy Techniques, Microsc. Microanal., 21, 510–517 (2015) doi:10.1017/S1431927614013580.

[12] M. Oujja, S. Psilodimitrakopoulos, E. Carrasco, M. Sanz, A. Philippidis, A. Selimis, P. Pouli, G. Filippidis, M. Castillejo, Nonlinear imaging microscopy for assessing structural and photochemical modifications upon laser removal of dammar varnish on photosensitive substrates, Phys. Chem. Chem. Phys., 19, 22836-22843 (2017) doi:10.1039/c7cp02509b.

[13] T. E. Villafana, W. P. Brown, J. K. Delaney, M. Palmer, W. S. Warren, M. C. Fischer, Femtosecond pump-probe microscopy generates virtual cross-sections in historic artwork, Proc. Natl. Acad. Sci. USA, 111, 1708–1713 (2014) doi:10.1073/pnas.1317230111.

[14] T. E. Villafana, W. Brown, W. S. Warren, M. Fischer, Ultrafast pump-probe dynamics of iron oxide based earth pigments for applications to ancient pottery manufacture, Proc. of SPIE, , 9527, 9 (2015) doi:10.1117/12.2184758.

[15] A. Dal Fovo, R. Fontana, J. Striova, E. Pampaloni, M. Barucci, M. Raffaelli, R. Mercatelli, L. Pezzati, R. Cicchi, Nonlinear optical imaging techniques (NLO) for painting investigation, Proceedings of LACONA XI Lasers in the Conservation of Artworks XI, P. Targowski et al. (Eds), NCU Press Torun (2017) doi:10.12775/3875-4.10.

[16] M. Oujja, C. Vázquez-Calvo, M. Sanz, M. Álvarez de Buergo, R. Fort, M. Castillejo, Laser-induced fluorescence and FT-Raman spectroscopy for characterizing patinas on stone substrates, Anal. Bioanal. Chem., 402:1433–1441 (2012) doi:10.1007/s00216-011-5319-2.

[17] A. Giakoumaki, K. Melessanaki,D. Anglos, Laser-induced breakdown spectroscopy (LIBS) in archaeological science - applications and prospects, Anal. Bioanal. Chem., 387:749–760 (2007) doi:10.1007/s00216-006-0908-1.

[18] A. Dal Fovo, M. Oujja, M. Sanz, A. Martínez-Hernández, M.V. Cañamares, M. Castillejo, R. Fontana, Multianalytical non-invasive characterization of phthalocyanine acrylic paints through spectroscopic and non-linear optical techniques, Spectrochim Acta A, Molecular and Biomolecular Spectroscopy, Elsevier, 208, 262-270 (2018) doi:10.1016/j.saa.2018.09.040.

[19] G. J. Tserevelakis, A. Dal Fovo, K. Melessanaki, R. Fontana, G. Zacharakis, Photoacoustic signal attenuation analysis for the assessment of thin layers thickness in paintings, J. Appl. Phys. 123, 123102-9 (2018) doi:10.1063/1.5022749.

[20] A. Dal Fovo, G. J. Tserevelakis, A. Papanikolaou, G. Zacharakis, R. Fontana, Combined photoacoustic imaging to delineate the internal structure of paintings, Opt. Letters 44, 4, pp. 919-922 (2019) https://doi.org/10.1364/OL.44.000919.

PART 1. Nonlinear techniques: physical principles and applications

*1. **Nonlinear optics***

NonLinear Optics (NLO) is the study of phenomena that occur as a consequence of the modification of a material's optical properties, following its interaction with light.[1] The term *nonlinear* refers to the nature of the material response to the applied optical field, meaning that the intensity of the generated signal tends to increase nonlinearly with the intensity of the incident light beam. In nonlinear processes, two or more incident photons may simultaneously interact with atoms or molecules within the same quantum event. Such physical effects are strictly dependent on the intensity of light and may be observed with the use of monochromatic and coherent light sources generating beams of high intensity (>10^{12} W/cm^2). Not surprisingly, the beginning of NLO studies is often considered to be right after the demonstration of the first working laser (Maiman, 1960), with the discovery of second harmonic generation by Franken *et al.* in 1961.[2] Specifically, the use of femtosecond (fs) pulsed lasers, tightly-focused inside materials by high numerical aperture microscope objectives, enables the generation of nonlinear signals, while ensuring both good penetration capability and high axial resolution (in the range of micrometres).

The main difference between nonlinear and linear optics relies on the dependence of polarization $\tilde{P}(t)$ (dipole moment per unit volume) of a material system upon the strength $\tilde{E}(t)$ of the applied electric field. In linear optics, the induced polarization depends linearly on the electric field strength, as described by the relationship

$$\tilde{P}(t) = \chi^{(1)}\tilde{E}(t) \quad (1)$$

where the constant of proportionality $\chi^{(1)}$ represents the linear susceptibility.[vii]

In nonlinear optics, the response is described by expressing the polarization $P(t)$ as a power series in the field strength $E(t)$, as

$$\begin{aligned} P(t) &= \chi^{(1)}\, E(t) + \chi^{(2)} E^2(t) + \chi^{(3)} E^3(t) + \cdots \\ &\equiv P^{(1)}(t) + P^{(2)}(t) + P^{(3)}(t) + \cdots \end{aligned} \tag{2}$$

where $\chi^{(2)}$ and $\chi^{(3)}$ are the second- and third-order nonlinear optical susceptibilities, and $P^{(2)}(t) = \chi^{(2)} E^2(t)$ and $P^{(3)}(t) = \chi^{(3)} E^3(t)$ express second- and third-order nonlinear polarization, respectively. Hence, nonlinear optical signals are the consequence of the polarization induced by a specific order of interaction in the Eq. (2). The nonlinear susceptibilities are bulk properties depending on the energy levels involved. In general, if the strength of the applied electric fields does not exceed the magnitude of the coulombic electric field inside the atoms or molecules ($E_{at} = 5.14 \times 10^{11}$ V/m)[viii], the use of a perturbative approach for the theoretical description of the nonlinear phenomena is justified.

1.1. Nonlinear optical processes

Depending on the optical and chemical properties of the material, the interaction with a focused laser beam may generate nonlinear scattering phenomena (harmonic generation) or nonlinear absorption with consequent emission of fluorescence (multi-photon excitation fluorescence). The order of the polarization determines the nature of the nonlinear interaction.

[vii] For simplicity, fields $\tilde{E}(t)$ and $\tilde{P}(t)$ are considered to be scalar quantities.

[viii] The characteristic atomic electric field strength is $E_{at} = e/(4\pi\varepsilon_0\alpha_0^2) = 5.14\times10^{11}$V/m, where e is the charge of the electron and α_0 is the Bohr radius of the hydrogen atom. (R. W. Boyd, 2003).[1]

1.1.1. Second-order polarization

The second-order polarization process is schematically described in Fig. 1, showing two photons of frequency ω, which are converted in one photon of frequency 2ω in a single quantum-mechanical process. An example of second-order nonlinear process is Second-Harmonic Generation (SHG).

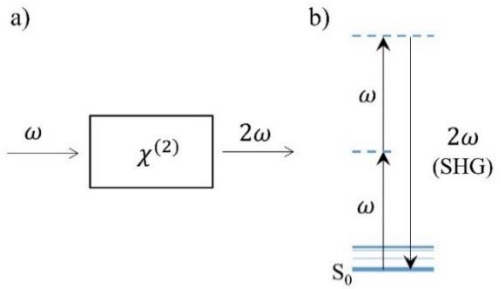

Fig. 1. Second Harmonic Generation. a) Sketch of the process. b) Energy-level diagram, describing the SHG frequency ω doubling process, from the atomic ground state S_0 (solid line) to the virtual levels (dashed lines), with the emission of a 2ω photon.

In terms of the polarization components, the second-order polarization can be explained as follows.

Assuming that the incident laser beam, whose electric field strength $E(t)$ at frequency ω, is represented by

$$E(t) = Ecos(\omega t) \tag{3}$$

using Euler's formula it becomes

$$E(t) = Ee^{-i\omega t} + c.c. \tag{4}$$

where *c.c.* stands for complex conjugate and i is the imaginary unit.[1]

According to Eq. (2), if the incident beam interacts with a material having nonzero second-order susceptibility $\chi^{(2)}$, the nonlinear polarization generated inside the material is $P^{(2)}(t) = \chi^{(2)}E^2(t)$ or

$$P^{(2)}(t) = 2\chi^{(2)}EE^* + (\chi^{(2)}E^2e^{-2i\omega t} + c.c.) \quad (5)$$

The second-order polarization is given by two contributions, the first at zero frequency (first term) and the second at 2ω frequency (second term). This latter contribution can lead to the generation of the second-harmonic frequency.

Second-order polarization is proportional to the square of the electromagnetic field, being the nonlinear susceptibility $\chi^{(2)}$ a proportionality constant related to the polarizability of the molecule $\langle\beta\rangle = \chi^{(2)}/N_s$, where N_s is the molecules density, and the brackets denote an averaged orientation. Thus, $\langle\beta\rangle$ is maximal for aligned molecular dipoles and becomes zero for molecules with antiparallel orientation, the contributions of which interfere destructively due to their phase shift.[3] Similarly, SHG is possible only in presence of polarizable molecules with specific symmetry properties, namely without a centre of inversion – i.e. non-centrosymmetric molecules. In fact, it is observed that for centrosymmetric molecules the nonlinear susceptibility $\chi^{(2)}$ vanishes. This principle can be theoretically verified by considering the second-order polarization produced in a molecule with inversion symmetry. In such case, if the sign of the applied electric field $E(t)$ changes, the induced second-order polarization $P^{(2)}(t) = \chi^{(2)}E^2(t)$ also changes. Hence, $P(t)$ is replaced by

$$-P^{(2)}(t) = \chi^{(2)}[-E(t)]^2 \quad (6)$$

which shows that

$$-P^{(2)}(t) = \chi^{(2)}E^2(t) \quad (7)$$

Being $P^{(2)}(t) = \chi^{(2)}E^2(t)$, $P^{(2)}(t)$ must be equal to $-P^{(2)}(t)$, which occurs only if $P^{(2)}(t)$ vanishes identically, meaning that

$$\chi^{(2)} = 0 \quad (8)$$

This result is described in Fig 2. The waveform of the incident monochromatic electromagnetic wave of frequency ω (2a) produces an identical waveform in a medium with linear response (2b), whereas in case of a nonlinear medium with centre of symmetry (2c), the polarization leads to the waveform distortion, with only odd harmonics of the fundamental frequency. Finally, for the case of a nonlinear, non-centrosymmetric medium (2d), both even and odd harmonics are present in the waveform associated to the atomic response. Furthermore, differently to the centrosymmetric medium, the time-averaged response is nonzero, because the medium responds differently depending on the direction of the electric field.

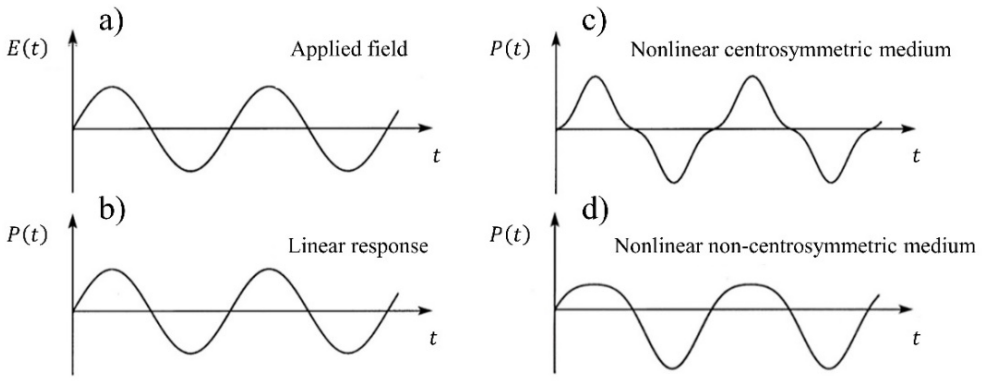

Fig. 2. Waveforms associated with the atomic response (R.W. Boyd, 2003).

Under proper experimental conditions, nearly all of the power of the incident laser beam can be converted into radiation at the second-harmonic frequency. Basing on this principle, one common use of SHG is to convert the output of a fixed-frequency laser to a different spectral region. For example, the Nd:YAG laser operating in the Near Infrared (NIR) spectral region at a wavelength of 1064 nm can be converted through SHG to a 532 nm green laser.

1.1.2. Third-order polarization

Third-order polarization, $P^{(3)}(t) = \chi^{(3)}E^3(t)$, is responsible for several nonlinear phenomena, such as Third-Harmonic Generation (THG) and multi-photon absorption, which gives rise to nonlinear excitation fluorescence.

For the description of the third-order nonlinear interaction, only the case of a monochromatic field, given by Eq. 3, is considered here.

By using the identity $cos^3\omega t = \frac{1}{4}cos3\omega t + \frac{3}{4}cos\omega t$, the nonlinear polarization can be expressed by

$$P^{(3)}(t) = \frac{1}{4}\chi^{(3)}E^3cos3\omega t + \frac{3}{4}\chi^{(3)}E^3cos\omega t \quad (9)$$

The first term describes a response at frequency 3ω, due to an applied field at frequency ω. This term leads to the process of Third-Harmonic Generation (THG), which is illustrated in Fig. 3. Similarly to SHG, in THG process three photons of frequency ω are simultaneously converted in one photon of frequency 3ω.

The phenomenon of THG under tight focusing conditions was firstly explored by Tsang (1995),[4] who demonstrated that the third harmonic process is allowed at an interface within the focal volume of the excitation beam. The THG power can be calculated as a function of the interface uniformity, as done by Y. Barad *et al.*,[5] showing that, when there is either a change in refractive index or third-order nonlinear susceptibility, the third harmonic power does not vanish. Because of this interface effect, THG imaging is possible and specifically suitable for transparent specimens with low intrinsic contrast, being also sensitive to changes in the specimen's nonlinear optical properties.[6]

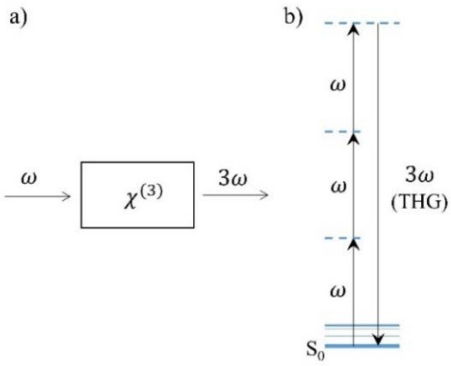

Fig. 3. Third Harmonic Generation. a) Sketch of the process. b) Energy-level diagram, describing the THG frequency ω tripling process. The solid line and the dashed lines represent the atomic ground state S_0 and the virtual levels, respectively.

Both frequency doubling and tripling processes – i.e. SHG and THG – arise from coherent scattering, and the generated signal propagates mainly in the same direction as the incident laser beam. The exact ratio of forward (transmitted) and backward (epi) signal depends on the sample characteristics, but generally, the backward-propagating signal is much weaker than its forward counterpart. Moreover, the epi-collection efficiency critically depends on the microscope field-of-view even at shallow depths, due to the diffusive nature of the backscattered light. The efficiency of the backward detection of THG can be improved through the coherent excitation of a large number of scatterers, or through resonance effects, enabling to overcome the limit of the weak third-order susceptibility in most media. Differently, the higher efficiency of Second Harmonic Generation in biological structures allows for the detection of SHG signals also in backward configuration.[7]

In these nonlinear scattering phenomena, no energy is deposited in the medium and the new photons are generated through a single step quantum process.[1] The interacting material acts as an energy converter of the incident photons, combining a number *N* of photons (2 or 3, for SHG and THG, respectively) of

energy $h\omega$ to emit one photon of energy $Nh\omega$. The Nth harmonic generation intensity scales with the intensity of the fundamental incident radiation I as I^N.

1.2. One- and multi-photon excitation fluorescence

When a laser beam interacts with a material, specific molecules (fluorophores) can be excited by the near-simultaneous absorption of one or two (or more) low-energy photons, which approximately match the energy difference between the excited and the ground state (S_2 and S_0, respectively). After few nanoseconds from the absorption, the excited molecule drops to the ground state, possibly generating the emission of fluorescence (Fig. 4). Multi-Photon Excitation Fluorescence (MPEF) refers to the excitation of a fluorophore when two or more photons arrive within a time window of an attosecond (10^{-18} s) and team up to excite the molecule.[3]. In principle, any combination of photons reaching the energy difference between S_0 and S_2 may generate nonlinear fluorescence. In Fig. 4b, two photons of equal wavelength are used to describe the phenomenon. Once in the excited state, after the transition to the singlet state S_2, the electron movements are the same as in single-photon excitation: the molecule undergoes a non-radiative decay with loss of energy by a sequence of iso-energetic Internal Conversion (IC) to reach S_1, followed by Vibrational Relaxation (VR), in which energy is dissipated in form of heat within the vibrational structure of S_1 electronic state. Generally, most molecules return to the electronic ground state without emission of light, by transferring their energy to the surroundings through collisional quenching and internal photo-conversion. However, after a delay of $\sim 10^{-8}$–10^{-9} s, the relaxation to the ground state may also result in the emission of light (fluorescence), which is characterized by lower energy (i.e. longer wavelength) than the absorbed one, in accordance with a phenomenon known as *Stokes shift*. The emission is

independent from the excitation wavelength, being the radiative decay generated at the lowest vibrational level of the excited state, and absorption/emission spectra are representative of each molecular species.

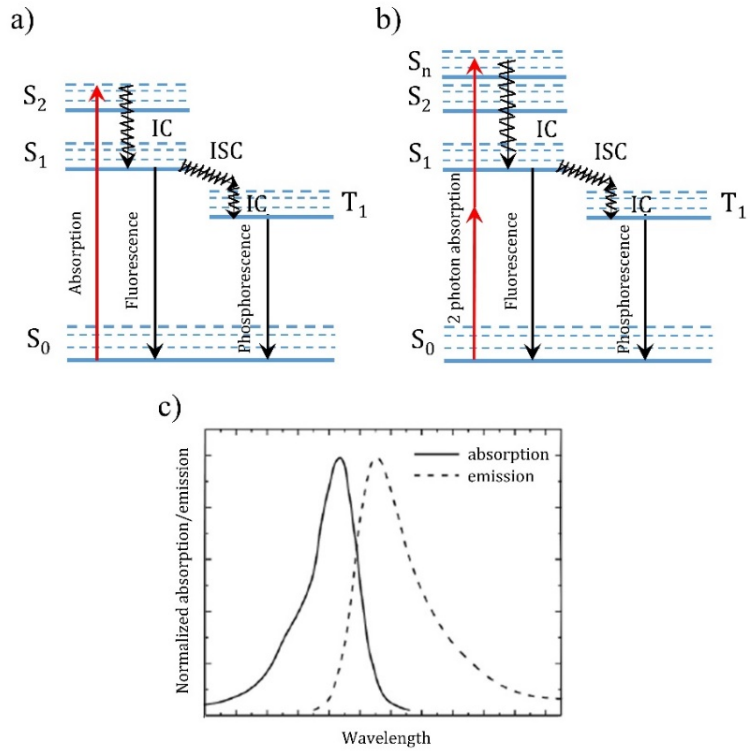

Fig 4. Jablonski diagram of a) single-photon excitation and b) multi-photon excitation, respectively. The electronic energy levels and their vibrational substructure are shown with horizontal lines, whereas the physical processes that cause transitions between these levels are depicted by vertical arrows. The singlet ground, first and second electronic states are labelled S_0, S_1 and S_2, respectively, and the first triplet state is labelled T_1. For each electronic state, the molecule can exist in a multitude of vibrational states indicated by the dashed lines. Internal Conversion (IC) and Inter-System Crossing (ISC) are represented by the jagged arrows. c) *Stokes shift* effect between normalized absorption and fluorescence emission spectra of a fluorophore.

The parameters that characterize a molecule's capacity for light absorption are the *molar extinction* ε (measured at peak absorption per mole and cm of optical path-length) and the absorption spectrum. Moreover, the capacity of a molecule

to fluoresce is determined by the fluorescence quantum yield ϕ or Q_f (dimensionless) and the emission spectrum (Fig. 4c). Hence, the brightness of a fluorophore is determined by the product $\varepsilon\phi$. The time that elapses between the absorption and the emission is called *fluorescence lifetime* (τ), which is typically exponentially distributed and is highly sensitive to the fluorophore environment.

From S_1, another possible event is the emission of a phosphorescent photon. In this case, the excited electron undergoes a sequence of Inter-System Crossing (ISC) to attain the triplet state, before dropping to the ground state through a sequence of vibrational processes. In this case, the lifetime of the excited state is significantly longer than in the fluorescence process, ranging from $\sim 10^{-4}$ s to minutes, or even hours. The drop to the ground state is accompanied by the emission of a photon of lower energy than the exciting one.

For each of these processes, the relative importance of a given decay pathway can be defined by a *quantum yield (Q)*. Specifically, the *fluorescence quantum yield* (Q_f) is expressed by the ratio between the emitted and the absorbed photons – i.e. the fraction of excited states that relaxes via the emission of a fluorescence photon

$$Q_f = k_r/(k_r + k_{nr}) \tag{10}$$

where k_r is the rate of relaxation to the ground state by fluorescence and k_{nr} is the rate of relaxation to the ground state by non-radiative processes.[8]

Similarly, the lifetime of an excited state is defined by:

$$\tau = 1/(k_r + k_{nr}) \tag{11}$$

As a general principle, the main difference between one and two photon absorptions relies on the diverse dependence on the applied field intensity I or, in other terms, on the field amplitude E. In fact, the transition rate of one

photon, as well as the fluorescence intensity, is linearly dependent on the intensity I of the optical field:

$$Abs_{1ph} \propto E^2 \propto I \tag{12}$$

whereas the transition rate of two photons is proportional to the square of the intensity I:

$$Abs_{2ph} \propto E^4 \propto I^2 \tag{13}$$

More generally, the probability of n-photon absorption by a molecule is proportional to I^n, thus increasing by concentrating the incident beam both spatially and temporally to obtain high photon flux (typically 10^{20}–10^{30} photons/cm^{2}s). This is commonly obtained by using a fs-pulsed laser, instead of continuous-wave light sources, tightly focused by a high numerical aperture objective. Hence, under daylight or arc-lamp illumination, the probability of two-photon absorption is virtually zero. That is why the experimental demonstration of Maria Göppert-Mayer's prediction of multi-photon excitation[9] had to await the advent of a mode-locked laser emitting photons intermittently in high-intensity bursts. As a result of the beam focusing, the intensity along the optical axis increases towards the focus and then decreases as the squared distance. Correspondingly, Two-Photon Excitation Fluorescence (2PEF) rises and then dwindles as the distance raised to the fourth power, confining 2PEF to the immediate vicinity of the focal spot (Fig. 5). The effective 2PEF volume, i.e. the volume in which the beam intensity is high enough to produce nonlinear absorption, is less than a femtolitre (10^{-15} litre). This three-dimensionally confined excitation greatly enhances the collecting efficiency, while reducing the out-of-focus photo-damage. The latter is unavoidable in One-Photon Excitation Fluorescence (1PEF), where the excitation occurs also in out-of-focus regions. To obtain optical sections, the

focus beam is scanned across the sample, as in confocal laser-scanning microscopy, but without need of a confocal pinhole. Furthermore, the penetration depth is usually increased, because the typically employed excitation wavelengths fall in the near infrared spectral range, where scattering and absorption losses are low for several materials.

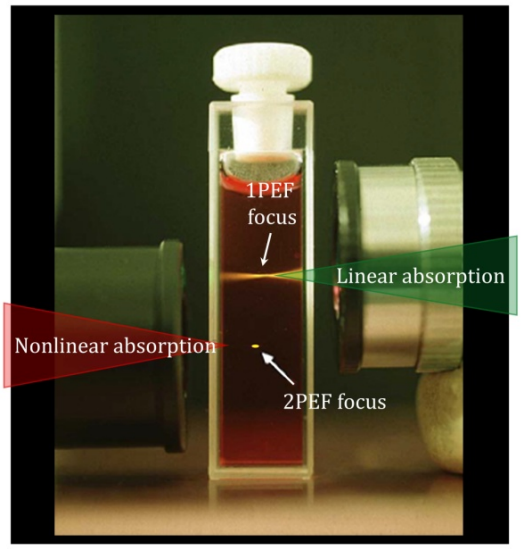

Fig. 5. One- and Two-Photon Excitation Fluorescence in a solution of dye safranin. The linear absorption is produced by the interaction with a green (543 nm) continuous-wave laser (upper objective lens on the right hand side of the sample), generating the expected Gaussian beam pattern of excitation. The lower objective lens on the left focuses a pulsed infrared laser beam (1046 nm), leading to the nonlinear interaction. The excitation volume is confined in a spot (arrow) in which the density of photons is sufficiently high to generate 2PEF (modified image from Brad Amos/Science Photo Library, London).

One- and Two-Photon Excitation Fluorescence emission spectra present the same trend and are both independent of excitation wavelength. On the other hand, the 2PEF absorption spectra can substantially differ from their 1PEF counterparts. In case of two-photon excitation, the *momenta* of the two

excitation photons combine together to give a higher degree of freedom than in single-photon excitation, meaning that nonlinear excitation allows electrons to access excited states like S_2 and S_4, higher than what is accessible with 1PEF, resulting in broader 2PEF absorption spectra for many fluorophores.[3] To compare and quantify 2PEF brightness among different fluorophores, instead of using the product of $\varepsilon\phi$ as in the 1PEF case, a two-photon action cross-section is defined as $\sigma_{2\omega}\phi$, where $\sigma_{2\omega}$ is the 2-photon absorption cross-section and ϕ is the quantum efficiency, as before.[ix]

1.3. Basic instrumentation for nonlinear microscopy

Typically, the detection of the nonlinear responses requires a scanning system enabling the movement of either the laser or the specimen. This can be accomplished in several ways, generally including a pulsed laser, which is introduced into an adapted microscope and directed to the specimen through a high NA objective lens. The scheme of a basic nonlinear microscope setup is depicted in Fig. 6. The raster scanning (xy) of the sample surface can be achieved with the use of galvanometric mirrors, whereas the movement of the focus through the sample in the axial (z) direction is generally controlled by a motorized stage. The signal is amplified and detected in backward direction, passing through the same objective as the incident beam, or collected in forward direction by a second objective.

[ix] For example, rhodamine 6G has a σ2ωϕ of 40 Göppert-Mayer units (GM; 1 GM = 10−50 cm^4 s/photon) at 830 nm.

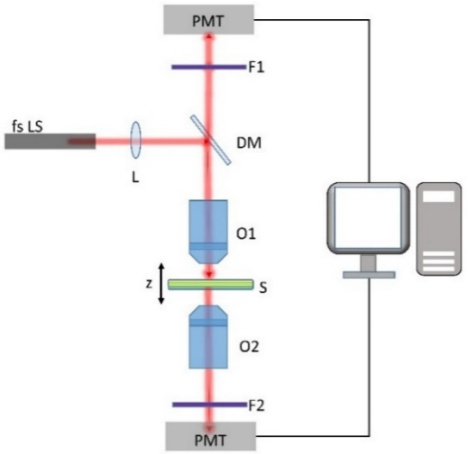

Fig. 6. Basic schematic of a nonlinear microscope: the fs-laser beam (fs LS) is collimated by a lens (L) and partially reflected by a dichroic mirror (DM) to an objective (O1) oriented towards the sample (S), which is placed on a motorized stage (Z). The generated signal is collected both in backwards and forward direction by the objectives (O1 and O2). After passing through the filters (F1 and F2), the output signal enters the photomultiplier (PMT) and is processed by the acquisition system.

1.3.1. Laser sources

The pioneering work of Denk in 1990,[10] introducing the use of a pulsed mode-locked dye laser for the nonlinear excitation of fluorescence in living cells in imaging modality, paved the way for the development of fs-pulsed lasers for nonlinear microscopy applications. Before that, the use of dye lasers was anyway decreasing, due to their toxicity, fast aging, low average power (with a maximum around 10 mW) and limited tuning range – steps greater than ~30 nm requiring a complete dye change.[11] The capability of ultrashort pulsed lasers changed abruptly with the introduction of high quality Titanium-sapphire lasers, thanks to the absence of toxic spills, extended spectral bandwidth (from 690 nm to greater than 1 μm, more than an order of magnitude greater than the best dyes), very short pulse duration (on the order of 10 fs), improved durability with excellent thermal conduction properties, and outstanding energy storage enabling significantly higher average power. Ti:sapphire lasers, based on an

active medium of crystal sapphire (Al_2O_3) doped with titanium ions, present the most efficient emission at around 800 nm and are typically pumped by other lasers at 514 to 532 nm, such as argon-ion and frequency-doubled (Nd:YAG, Nd:YLF, and Nd:YVO) lasers. The potential of Ti:sapphire in ultrashort pulse oscillators was shown by Spence *et al.* in 1991,[12] sparking a revolution in solid-state ultrafast oscillators. In a few years, the development of Kerr lens mode-locked lasers increased the average power to 1 W, while dramatically reducing the pulse duration. Although other sources, such as Yb:YAG, Cr:LiSAF, Nd:YLF, Nd:glass, Cr:fosterite, and fibre-based lasers, have proven useful for multi-photon imaging applications, Ti:sapphire lasers have become the first choice for multi-photon microscopy, despite their still high cost.

1.3.2. Optical resolution in nonlinear microscopes

The interaction volume is determined not only by the focusing properties of the microscope's objective (numerical aperture, NA) and the radiation wavelength used, but also by the nonlinear order of the interaction.[11] The numerical aperture is related to the refractive index n of a medium, as well as with the angular aperture ϑ of a given objective, following the relation $NA = n \cdot sin\vartheta$. By using the maximum angular aperture (around 144º) of an oil-immersion objective (n_{oil} = 1.52), the maximum NA will be 1.45, whereas with a dry – i.e. non-immersion – objective, the maximum NA will be 0.95 (n_{air} = 1.0). The optical resolution is traditionally defined basing on the Rayleigh criterion, which states that two components of equal intensity should be considered resolved when the main intensity maximum of one coincides with the first minimum of the other.[13] The diffraction-limited focusing properties of a high-numerical aperture microscope objective and, subsequently, its optical resolution, can be described by the minimum lateral and in-depth distance

between resolvable points, i.e. the radial and axial coordinate, r and z, respectively:

$$r_0 = 1.22\,\lambda/2n \cdot sin\vartheta = 0.61\,\lambda/NA \tag{14}$$

$$z_0 = 2n\,\lambda/(NA)^2 \tag{15}$$

where r and z are in the same unit as the wavelength λ, of the beam interacting with the medium with refractive index n. According to Eq. 14 and 15, the resolution in radial and axial directions increases when using shorter wavelengths and higher NA.

In general, a signal with nonlinear dependency on the electric field intensity tends to reduce the interaction volume with respect to its linear counterpart, thus increasing the optical resolution. In fact, considering the focal field intensity as Gaussian distribution

$$I(x) = e^{-x^2/2\sigma^2} \tag{16}$$

for which the Full Width at Half Maximum (FWHM) is

$$\text{FWHM} = 2\sigma\sqrt{2\ln(2)} \tag{17}$$

For an Nth order process, the FWHM reduces to

$$\text{FWHM} = \frac{1}{\sqrt{N}}2\sigma\sqrt{2\ln(2)} \tag{17}$$

Hence, as a general rule, the interaction volume of a Nth order nonlinear process decreases by a factor of $\sqrt{N}$, with respect to the linear interaction volume at the same optical wavelength.

However, in multi-photon absorption processes, the excitation of the one-photon equivalent electronic transition of the fluorophore requires a longer wavelength, that scales with the nonlinearity of the process as

$$\lambda^{(n)} = N\lambda^{(1)} \tag{18}$$

where (n) denotes the order of the process.
Thus, in multiphoton absorption processes, the decrease in resolution from the increase in wavelength is compensated only in part by the decrease in the interaction volume, due to the nonlinearity of the interaction. Effectively the interaction volume for a N-photon absorption process increases by a factor of $\sqrt{N}$, relative to its single-photon absorption counterpart.[11]

In conclusion, NLOM offers several advantages with respect to other linear optical techniques, which can be summarized as follows. The use of a single femtosecond laser source enables the simultaneous generation of all the nonlinear phenomena (SHG, THG, MPEF) in the focal volume of the examined object: this entails that several information – chemical, structural, morphological, optical – can be obtained in one single measurement. Moreover, the nonlinear dependence of the generated signal intensity on the excitation light intensity entails that the efficient nonlinear interaction is confined in the focal volume of the laser beam, thus providing intrinsic axial resolution. Out-of-focus damages (i.e. photobleaching phenomena) are drastically diminished, which is a priority for CH studies. In specific, the minimal disturbance to the analysed specimen is ensured by nonlinear scattering process, such as SHG and THG, since no energy is deposited in the medium. Finally, in NLOM the penetration depth is generally high, enabling deeper probing capability, thanks to the use of long wavelengths (typically in the near infrared range).

References

[1] R. W. Boyd, Nonlinear Optics, Second Edition, the Institute of Optics, University of Rochester, New York, USA, Academic Express (2003).

[2] P. Franken, A. Hill, C. Peters, G. Weinreich, Generation of Optical Harmonics, Phys. Rev. Letters, 7 (4), 118–119 (1961) doi:10.1103/PhysRevLett.7.118.

[3] M. Oheim D. J. Michael, M. Geisbauer, D. Madsen, R. H. Chow, Principles of two-photon excitation fluorescence microscopy and other nonlinear imaging approaches, Adv. Drug Deliv. Rev., 58 (7), 788-808 (2006) https://doi.org/10.1016/j.addr.2006.07.005.

[4] T. Y. F. Tsang, Optical third-harmonic generation at interfaces, Phys. Rev. A, 52, 4116-4125 (1995).

[5] Y. Barad, H. Eisenberg, M. Horowitz, Y. Silberberg, Nonlinear scanning laser microscopy by third harmonic generation. Appl. Phys. Lett. 70, 922-924 (1997) doi: 10.1063/1.118442.

[6] J. A. Squier, M. Müller, G. J. Brakenhoff, K. R. Wilson, Third harmonic generation microscopy, Opt. Express, 3, 9, 315-324 (1998).

[7] D. Débarre, N. Olivier, E. Beaurepaire, Signal epidetection in third-harmonic generation microscopy of turbid media, Opt. Express 15(14), 8913–8924 (2007).

[8] M. A. Omary, H. H. Patterson, Luminescence, Theory, Reference Module in Chemistry, Molecular Sciences and Chemical Engineering, Encyclopedia of Spectroscopy and Spectrometry (Third Edition), Elsevier, 636–653 (2017) https://doi.org/10.1016/B978-0-12-803224-4.00193-X.

[9] M. Göppert-Mayer, Über Elementarakte mit zwei Quantensprüngen, Annals of Physics., 9 (3), 273–95 (1931) doi:10.1002/andp.19314010303.

[10] W. Denk, J. H. Strickler, W. W. Webb, Two-photon laser scanning fluorescence microscopy, Science 248, 73 (1990).

[11] J. Squier, M Muller, High resolution nonlinear microscopy: A review of sources and methods for achieving optimal imaging, Rev. Sci. Instrum., 72, 2855-2867 (2001) doi:10.1063/1.1379598

[12] D. E. Spence, P. N. Kean, W. Sibbett, 60-fsec pulse generation from a self-mode-locked Ti:sapphire laser, Opt. Lett., 16, 42 (1991).

[13] M. Born and E. Wolf, Principles of Optics, 6th ed. Pergamon, Oxford (1980).

2. Applications of NLOM in Cultural Heritage science: state-of-the-art

In the last years, NonLinear Optical Microscopies (NLOM) are spreading in several scientific fields, but originally their use was restricted to biomedical applications, mainly for in vivo imaging and mapping of subcellular structures. Specifically, Second Harmonic Generation (SHG) has proven useful for the analysis of stacked membranes and arranged proteins with organized structures, such as collagen,[1,2] as well as for probing membrane-potential-induced alignment of dipolar molecules.[3] Third Harmonic Generation (THG), being generated from regions with optical discontinuities,[4] has been used for detecting structural and anatomical changes of biological samples at cellular or sub-cellular level.[5,6] Since 1990,[7] Multi-Photon Excitation Fluorescence (MPEF) has been playing a pivotal role in the study of biological matter, in conjunction with confocal microscopy, for a variety of applications, ranging from the tracking of individual molecules within living cells to the observation of whole organisms.[8]

More recently, nonlinear imaging techniques have been introduced in the field of Cultural Heritage for the analysis of several types of artworks.[9] Their application ranges from the study of varnish protective layers, oils, synthetic glues and overpaintings, to the visualization and characterization of wood microstructures, and identification of corrosion layers in metal-based objects. The potential to provide compositional and structural information of different materials makes these non-destructive high-resolution modalities a promising tool for art diagnostics.

As regards paintings, some tests have been performed on painted mock-ups characterized by different binding media and pigments, exploiting the relative transparency of most pictorial materials in the near infrared region. The final aim of such applications is to obtain the micrometric surface mapping and the in-depth profiling of thin films of pictorial materials on the basis of refractive

index changes, variation of optical activity and presence of fluorophores. This information may turn definitely useful for the analysis of painted objects, as well as for the monitoring of restoring operations, like the cleaning process, which irreversibly modifies the morphology and thickness of the superficial layers.

2.1. Varnishes, oils and glues

In 2008, Filippidis *et al.* applied Three-Photon Excitation Fluorescence (3PEF) and Third Harmonic Generation imaging for the determination of thickness in natural and synthetic varnish layers laid on glass cover-slips.[9] A diode-pumped Yb-doped solid state laser with central wavelength at 1028 nm was used for exciting 3PEF and THG signals, which were collected simultaneously in backwards and transmission modes, by using two different objective lens placed at both sides of the sample. Several natural (mastic and colophony) and synthetic (Vinavil®) varnishes were studied. Preliminary UV-Vis absorption analysis attested the transparency of all the materials at 514 nm and maximum absorption of UV wavelengths. The fluorescence emission excited at 343 nm was also investigated, showing a maximum at 428 nm and 408 nm for mastic and colophony, respectively, whereas, when exciting at 514 nm, no emission was detected. These results confirmed that the nonlinear fluorescence observed by irradiating the two natural varnishes with the fs-laser at 1028 nm was a three-photon excitation process. The absorption of Vinavil was less than 3% at 343 nm and, consequently, no fluorescence was detected. Concerning the acquisition of THG in transmission mode in a multi-layered sample, the refractive index mismatch between the media allowed distinguishing different interfaces (air/Vinavil, Vinavil/mastic, mastic/glass, glass/air). 3PEF signals arising only from the mastic layer provided complementary information on a

single measurement, enabling the evaluation of the layers' thickness. Two overlaying layers of natural varnishes, colophony and mastic resulted not distinguishable by THG, due to the too low difference between the respective refractive indexes. However, by exploiting the different absorptivity, two different levels of nonlinear fluorescence signal were observed (Fig. 1).

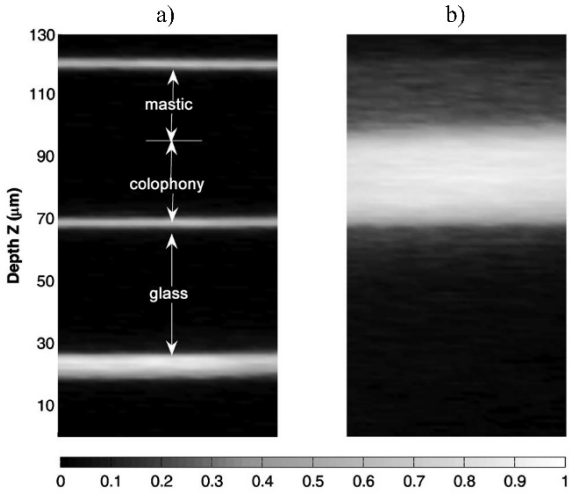

Fig. 1. Sections a) by THG signal and b) by 3PEF analysis of a multi-layered sample with mastic and colophony showing the interfaces, and the different nonlinear fluorescence, respectively. (G. Filippidis *et al.*, 2008)

In 2009,[10] Gualda *et al.* determined the thickness of varnish layers over painting samples, using a combination of THG and MPEF imaging modalities in the reflection mode, with an excitation wavelength of 1028 nm. The painting layers were prepared with different pigments and binders, including ready-made acrylics (lemon yellow, ochre yellow), oil-tempera (ochre yellow with linseed oil), and egg-tempera (titanium white and barium chromate). All paints were covered with colophony resin. Nonlinear fluorescence and THG signal of colophony were preliminary measured on a single-layer sample. In some cases, the presence of the paint underneath the varnish made possible the detection of THG in reflection mode, although most of the signal is generally transmitted in

forward direction due to the coherent nature of THG. It was observed that the absorption behaviour of the different pigments to the excitation wavelength strongly influences the generation and detection of nonlinear signals from the varnish. In fact, all panting materials showed absorption at the fundamental laser wavelength (1028 nm) and different interaction at 514 and 343 nm. By contrast, the minimal absorption of colophony in the visible and infrared spectral regions indicated that the main contribution to the nonlinear fluorescence process was due to three-photon excitation. Furthermore, it was observed that the damage threshold for paintings was around 20 mW laser power (less than 0.4 nJ per pulse). In presence of ochre yellow and barium chromate substrates, air/colophony and colophony/pigment interfaces were detectable through THG in reflection mode (with a clear visualization in case of air/colophony interface). The higher refractive index mismatch between ochre yellow and colophony, with respect to barium chromate and colophony, increased the efficiency of THG process. It is worth to mention that only the visualization of the outer structures of the model paintings was feasible, due to the strong absorption of the pigments, thus making the detection of THG in transmission mode not possible.

Concerning MPEF, the signals showed different intensity values depending not only on the pigment, but also on the binding medium. In fact, strong fluorescence signals from linseed oil and egg were observed, but no signal was detected from acrylics. This indicates that, in specific cases, MPEF may provide complementary information about the painting technique.

A further combined application of THG and 3PEF was performed by Nevin *et al.* (2010)[11] for the analysis of multi-layer samples composed of triterpenoid varnishes (dammar and mastic) over linseed oil, laid on glass support. Results obtained through nonlinear measurements were integrated with Confocal Raman Microscopy (CRM) for a chemical characterization of the samples as a

function of depth. CRM spectra, acquired in the fingerprint region (between 500 – 1900 cm^{-1}) and in the C–H stretching region (2600 – 3200 cm^{-1}) at different depths, were integrated with multi-photon measurements. Using a fs-laser at 1028 nm, strong THG signals were observed at the interfaces between air and varnish, oil and glass, glass and air, whereas weaker signals were detected at interfaces between varnish and oil. This was ascribed to the smaller refractive index mismatch between the organic media and auto-absorption of THG signal by the sample itself (Fig. 2a). 3PEF analysis was useful for a distinction between materials but with significant limits of interpretation, because the fluorescence emitted by mastic, dammar and linseed oil was not easily distinguishable (Fig. 2b).

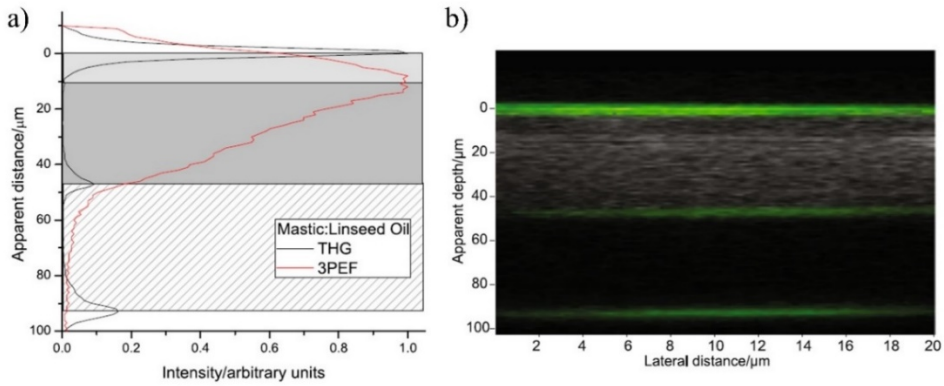

Fig. 2. a) THG and 3PEF signal in a multi-layered sample of mastic/linseed oil on glass; the thickness of the different materials are indicated in light grey for mastic, dark grey for linseed oil, and diagonal lines for glass support. b) Reconstructed image of the same sample showing THG signal at the interfaces (green lines) and 3PEF signal (greyscale). Mastic and oil are characterized by similar 3PEF intensities. (A. Nevin *et al.*, 2010)

Another study involving layers of natural varnishes was carried out by Filippidis *et al.* in 2015, for the in-depth determination of the affected regions due to artificial aging.[12] Single photon Laser Induced Fluorescence (LIF)

measurements and Raman spectroscopy were used for the integrated investigation of the degradation in dammar and mastic. The artificial aging was obtained by exposing the varnishes to a mercury discharge lamps for 61 days (~ 29 lux × 106 hours), equivalent to 50 years of exposure in museum conditions.[13,14] Nonlinear analysis was performed using a fs- laser at 1028 nm, and MPEF and THG signals were collected simultaneously in backward and transmission modes, respectively. The sample was analysed before and after the aging. As regards the dammar varnish, three different layers were distinguished through THG measurements indicating the interface between the different media (dammar/air, glass/dammar, air/glass). The visualization of the stratigraphy was complemented by MPEF signal, which was mainly attributed to three- and four-photon excitation – i.e. absorption at 343 and 257, respectively. Furthermore, MPEF measurements provided in-depth information related to the affected region of the dammar due to artificial aging (Fig. 3a and b).

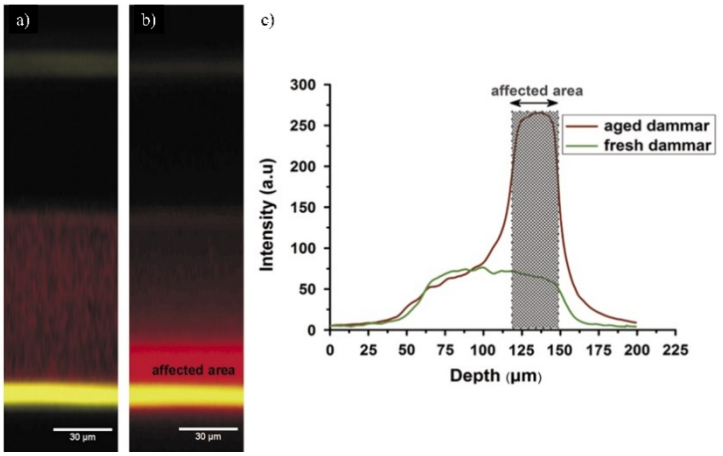

Fig. 3. Multimodal nonlinear imaging of (a) fresh and (b) aged dammar varnish sample. THG and MPEF signals are highlighted in yellow and red colours, respectively. c) Plots of the pixel brightness distribution of the cross sectional images a) and b) across a vertical line (green and dark red line, respectively). The grey region denotes the affected area as a function of depth from the surface of the aged dammar sample. (G. Filippidis *et al*., 2015)

Plots of the pixel brightness distribution across a central vertical line for the two image were performed, showing a significant increase in the MPEF signal from the surface until a depth of 31 μm in the aged dammar sample (Fig. 3c).
As regards mastic, the extension of the affected region due to artificial aging was found to be around one third of that of the dammar sample. Such difference was attributed to the higher absorption coefficient of mastic at 360 nm, which coincides with the emission peak of the mercury lamps, and to the exponential decrease of the incident light intensity as a function of the sample thickness.

In another study,[15] THG and SHG in transmission and reflection mode were applied conjunctly to the analysis of lining glues, enabling the determination of thickness layers and the discrimination between different materials. Different types of natural and synthetic lining glues (beeswax-based paste, rabbit skin glue, starch glue, Beva 371®, Lascaux 498 HV®, Mowilith®, Vinavil®) were casted on thin cover-slips for the analysis. In all cases, the excitation wavelength was 1028 nm and the average laser power on the specimen was 30 mW (0.6 nJ per pulse), to prevent the samples from damage. THG signals were collected in transmission mode using a 340-nm coloured glass filter, while SHG signals were detected in the backward direction using a 514-nm interference filter. THG signal was proved effective for the evaluation of layers thickness through the visualization of the interfaces, whereas SHG measurements provided complementary information related to the composition of the glues, specifically about the presence or absence of collagen and starch granules. As expected, the only materials producing SHG signals were rabbit skin glue, beeswax paste and starch glue, all containing compounds with non-zero second-order nonlinear susceptibility. In one case (Vinavil), a small portion of the material was mechanically removed and the THG measurements before and after the treatment were compared in order to quantify the entity of the removal (Fig. 4).

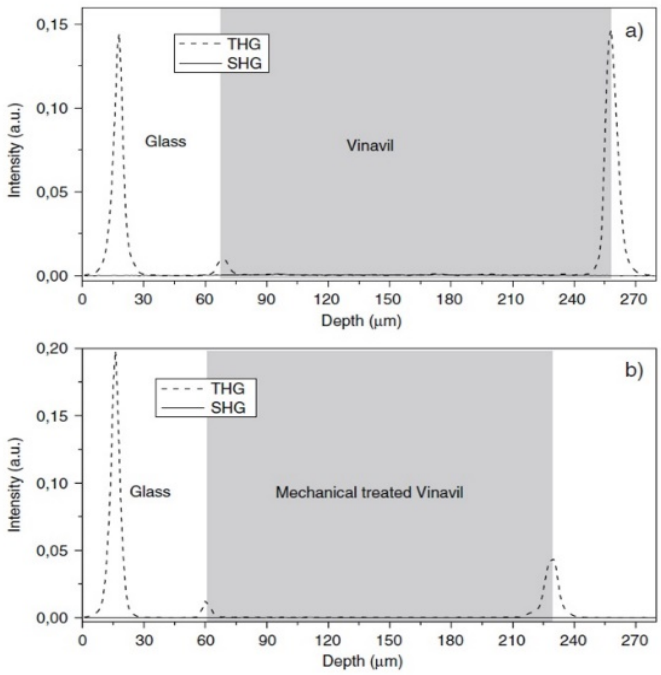

Fig. 4. Vinavil sample nonlinear spot measurements showing the THG signal arising from the interfaces air/glue and glue/glass, before (a) and after (b) the mechanical removal of glue. The thickness reduction of the layer was quantified, resulting around 20 μm. (G. Filippidis *et al.*, 2009)

2.2. Overpaintings - Monitoring of the cleaning process

A. Selimis *et al.*[16] in 2009 and P. Vounisiou *et al.* in 2010[17] applied multi-photon excitation fluorescence on samples simulating real cases of overpaintings for the monitoring of the laser-removal of organic and inorganic acrylic paint layers. A thin layer of polymer imitating the original acrylic surface was covered with the acrylic paint to simulate the real case of an over-layered modern painting. The polymer was poly-methyl methacrylate (PMMA) and Paraloid B72 (copolymer of ethyl-methacrylate), doped with aromatic compounds (1,4-Di[2-(5-phenyloxazolyl)] benzene: POPOP), whose strong fluorescent emission allows the employment of Laser-Induced Fluorescence (LIF) for the detection of modifications generated into the substrate upon the

laser-assisted removal. Hence, the evaluation of the extent of the laser induced photochemical modifications at the substrate was obtained by measuring the fluorescence emitted by the polymer. Laser Induced Fluorescence (LIF) and MPEF were applied for the in-depth monitoring of photochemical and structural alterations. Nonlinear measurements were performed using a femtosecond laser oscillator with emission wavelength 1028 nm.

LIF allowed for the detection of changes in POPOP fluorescence spectra after the irradiation of the overlaying acrylic paint with several pulses at specific laser fluence, showing when the photochemical changes induced at the polymer substrate took place, once the overpainting was removed. Then, the irradiated layer was analysed by MPEF, enabling the analysis of the in-depth extent of fluorescence before and after the irradiation. It was observed that the laser treatment affected the fluorescence properties within a depth of around 11 μm from the sample surface (Fig. 5).

A further study on polymeric coatings was performed by Filippidis *et al*. in 2014,[18] for the assessment of the affected region during laser cleaning. A thin film of Paraloid B72 was irradiated with a single-pulse at 248 nm (fluence 400 mJ/cm^2) and the subsequent swelling of the polymer was analysed with THG imaging using a fs-laser at 1024 nm. It was observed that the swelling interfaces could not be precisely determined with a single measurement, since the laser light was intensely scattered from this roughish surface. The propagation of the excitation beam was limited by scattering effects, thus obstructing the THG signal generation inside the material. To overcome this problem, the sample was reversed and THG signals were collected from each side of the sample: the visualization and the quantitative determination of the contour of the laser-induced swelling/bulk material interface was then feasible.

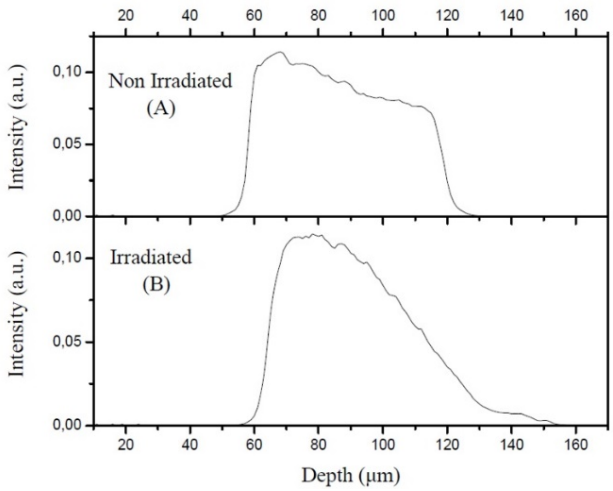

Fig. 5. MPEF measurement on POPOP before and after irradiation with excimer laser. The MPEF intensity profile (top graph) of the non-irradiated sample shows a FWHM of 58.8 μm, whereas the FWHM after laser irradiation (bottom graph) was reduced to 47.6 μm. The laser treatment affected the fluorescence properties on a thickness of nearly 11 μm from the sample surface. (A. Selimis *et al.*, 2009)

In 2017, Oujja *et al.*[19] used the same photosensitive polymer for assessing structural and photochemical modifications upon laser removal of dammar varnish. Different wavelengths (266, 248 and 213 nm) and pulse durations in the ranges of nanosecond (10^{-9} s), picosecond (10^{-12} s) and femtosecond (10^{-15} s) were explored to find the right conditions for partial or total removal of the varnish layer. Using a tightly focused femtosecond laser at 1028 nm as excitation source, THG and MPEF responses were combined to characterize the extent of morphological and photochemical modifications in the varnish layer, as a function of depth. THG signals marked the thickness reduction under laser ablation, whereas changes in intensity in MPEF signals were ascribed either to the dammar or to the photosensitive under-layer, and their dependence on the laser ablation parameters was defined. As an example, the results obtained through bimodal nonlinear imaging of a dammar/POPOP sample before and after laser ablation at 266 nm are reported in Fig. 6. By using 115, 346 and 692

pulses of 150 ps, the varnish layer was gradually reduced until the complete removal, and then analysed. The vertical displacement of the position of the air/dammar interface was detected through THG.

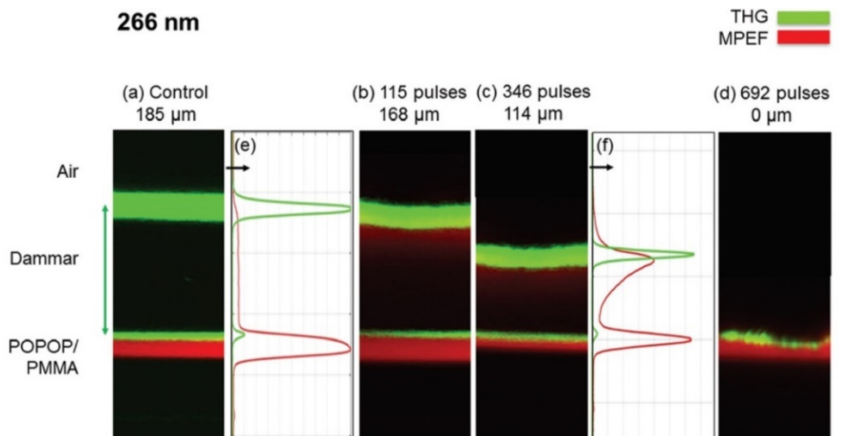

Fig. 6. Cross sectional multimodal nonlinear imaging of a POPOP/PMMA sample coated with dammar upon irradiation at 266 nm, 150 ps (F = 310 mJ cm^{-2}) with an increasing number of pulses, from 0 (a) to 115 (b), 346 (c) and 692 (d). Red and green areas correspond to MPEF and THG signals, respectively. The thicknesses of the initial and the remaining dammar layer are reported over the images. The horizontal dimension of the images is 100 µm. Next to the nonlinear images are displayed the corresponding plots of the pixel brightness distribution e) and f). The intensities of the MPEF and THG signals are normalized to the value obtained at the corresponding control region. (M. Oujja *et al.*, 2017)

It was observed that the MPEF signal arising from the dammar layer increased in intensity with the number of pulses, due to oxidative degradation following the exposure to the UV laser light. It is worth mentioning that affected region measured through MPEF resulted considerably larger than the mean penetration depth, estimated around 12 mm for 266 nm laser ablation,[20] thus showing the capability of the NLM technique to evaluate the real extent of the photochemical changes induced by laser. Furthermore, NLM measurements showed that the absorption coefficient of varnish at the ablation wavelength plays a more crucial role than that of the pulse duration: the increased UV light

absorption due to aging reduces the extent and the in-depth dimension of the photochemical modifications induced by the photo-ablation, thus highlighting the advantages of using ablation wavelengths that are strongly absorbed by the material.

2.3. Wood microstructures

In 2012, the *in situ* application of nonlinear modalities (SHG and 2PEF) enabled both the imaging and the chemical characterization of wood microstructures inside a historical violin.[21] In the same study, the analysis of multi-layered model samples including varnish films, cochineal, sandarac, plaster was performed. Pixel-wise images were recorded using a femtosecond Ti:Sapphire laser tuned to 860 nm and scanned within the sample.

Both 2PEF and SHG signals were detected in backward direction: despite the higher efficiency of SHG detection in the forward direction, signals can be recorded also in the backward direction when enhanced by specific structures or backscattered by strong scattering media, as in the case of wood microstructures – i.e. cellulose. SHG and 2PEF were performed on thin shavings (about 30 μm thick) of Acer wood, using a high-pass GG455 filter, revealing the well-known wood structure, specifically the wood fibres and groups of medullar rays (Fig. 7a and b). SHG signals were ascribed to crystalline cellulose, due to the hierarchical ultrastructure and the parallel orientation of the molecular chains, whereas 2PEF signals were attributed to lignin. The analysis was then applied on a locally damaged area of a historical violin, clearly revealing the cracks in the 485 nm spectral range (Fig. 7c). The study showed that nonlinear imaging may turn useful to obtain quantitative information on wood composition for a comparison between different species and to study the effects of treatment or aging on wood microstructure. Indeed, such microscopic properties are key

parameters to better characterize the macroscopic mechanical properties of wood.

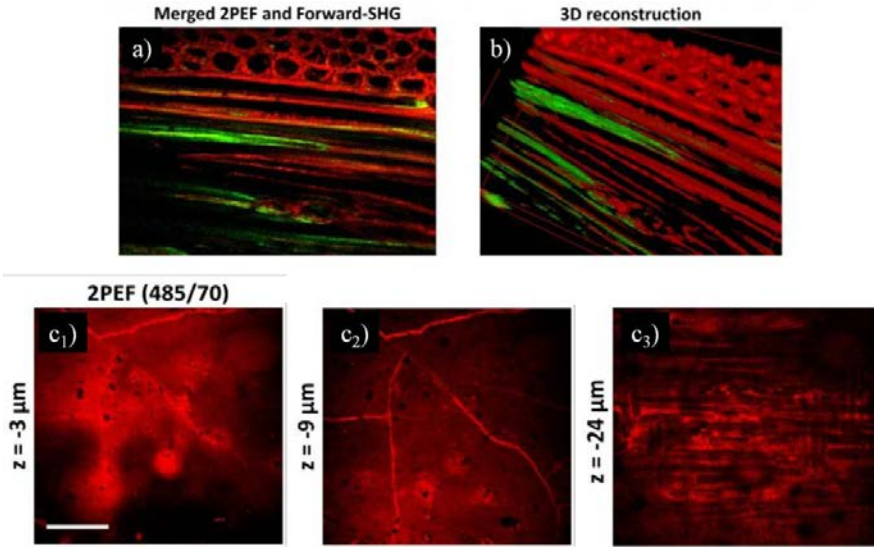

Fig. 7. 2PEF measurement on a wood specimen. Merged 2PEF (red) and forward-SHG (green) image (a) and 3D reconstruction (b) of the same region. 2PEF signal ($c_{1\text{-}3}$) filtered at 485 nm, acquired on a damaged area of a historical violin showing the micrometric cracks – scale bar 100 µm. (Latour *et al.*, 2012)

2.4. Metal-based artefacts

In 2013,[22] MPEF imaging was applied to the study of silver-based artefacts to identify the corrosion layers – i.e. chlorargyrite, the mineral form of silver chloride (AgCl). The analysis was performed on reference silver-based alloys, purposely treated with an aging procedure for accelerated degradation. MPEF signals were generated by irradiating the samples with a pulsed laser at 1028 nm, and acquired in backward direction. Emission measurements at an excitation wavelength of 257 nm allowed to spectrally characterize the fluorescence emission of chlorargyrite. On this basis, the MPEF signal was ascribed to a four-photon absorption process, and the subsequent 3D

reconstruction enabled not only to evaluate of the corrosion layer thickness, but also to analyse the morphology and density of AgCl crystals (Fig. 8).

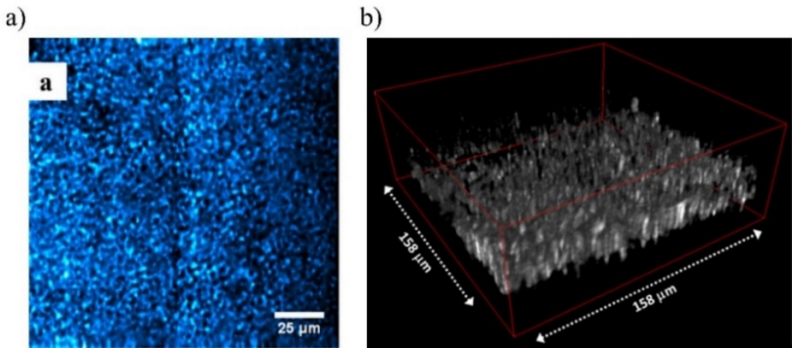

Fig. 8. a) Maximum z-projection MPEF image of the chlorargyrite layer surface. b) 3D reconstruction of 50 sequential optical planes, separated by a distance of 1 µm, of MPEF signal generated from the AgCl layer. (F. Faraldi et al., 2013)

2.5. Painting layers

Only few nonlinear analyses on painting layers have been carried out in the last years. In 2014, Filippidis *et al.*[18] performed THG and measurements on two painted samples on glass support, made with an ultramarine blue acrylic tempera, the first, and an egg tempera layer with titanium white (TiO_2) covered by colophony varnish, the second. The ultramarine acrylic layer was measured with a fs-laser emitting at 1560 nm. The detection of THG signals in imaging mode enabled both the determination of the thickness (58 µm) and the evaluation of the particle distribution in the acrylic medium. Since the refractive index mismatch between the pigment and the acrylic binder is minimal, the main contribution to the effective generation of THG was attributed to the abrupt change of the third-order susceptibility value. Moreover, a small portion of the pigment fluorescence, at 520 nm, allowed for the enhanced contrast among ultramarine particles/aggregates and the surrounding acrylic environment (Fig. 9a).

A multimodal image combining THG and MPEF signals was acquired on the multi-layer painted sample (Fig. 9b). Both signals were recorded in the reflection mode, using a 1028 nm excitation wavelength. The THG measurements revealed the thickness of the varnish layer (around 35 µm), whereas the nonlinear fluorescence signal, arising more strongly from the painting layer than from colophony, enabled the discrimination of the composition between the two different materials.

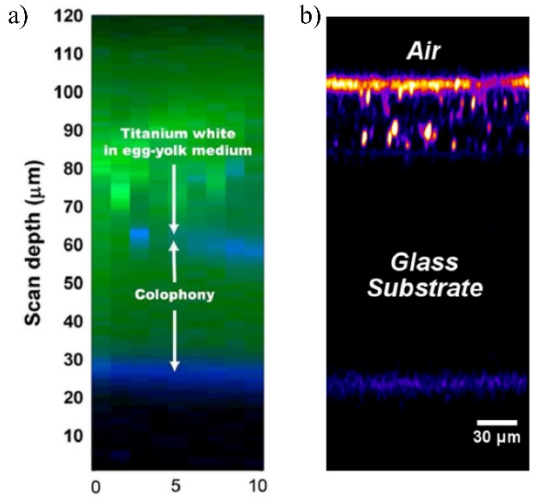

Fig. 9. a) Section of a multilayer model painting sample: blue and green areas represent THG and MPEF signals, respectively. The scanning lateral dimension of the recorded image is 10 µm). b) THG cross-sectional imaging of a layer composed of ultramarine blue pigment in acrylic binder, on glass support. (G. Filippidis *et al.*, 2014)

A research line, which goes in parallel with those previously described, concerns pump-probe microscopy analysis for the non-destructive 3D imaging of paintings with molecular and structural contrast (Villafana *et al.* 2014).[23] Briefly, pump-probe microscopy uses a sequence of ultrafast pulses (typically 0.2 ps, in duration) to first electronically excite molecules and then probe their response at a later time (up to about 100 ps) with a second laser. As the pump pulse moves a fraction of the ground state population into electronic excited states, a corresponding hole in the ground state spectral distribution is created.

In response to the excitation, population distributions in both ground and excited states rearrange (excited state population tends to relax back to the ground state). The changes in population can be monitored by applying a second delayed (probe) pulse. Each molecular process causes a specific pump-probe delay as a function of the pump intensity, making the detected signals molecular signatures.[24] With respect to biological tissues and skin imaging, the application of this technique on artworks is more challenging, due to the wide variety of organic dyes and inorganic minerals contained in artistic colorants, which hamper the achievement of the correct pump-probe contrast. However, by using an increased spectral range (form the NIR to the visible) of both the pump and the probe beams, with a variable time delay between the pump-probe pulses, it is possible to perform *in situ* 3D imaging of paintings with molecular specificity.

In Villafana's work, a Ti:Sapphire mode-locked laser emitting in the NIR at a repetition rate of 80 MHz was used. An adjustable optical path length in the probe optical arm controlled the inter-pulse delay between the pump pulse train (intensity-modulated) and the probe pulse (unmodulated). Any nonlinear interaction of the pump laser with the sample transferred the modulation from the pump to the probe. A photodiode and a lock-in amplifier with a reference at the modulation frequency detected changes in the probe intensity. Tests were carried out on a set of mock-up paintings, including two different blue pigments, synthetic ultramarine and lapis lazuli, covered or mixed with red pigment (quinacridone) to create a purple hue. Virtual cross-sections were obtained after the assessment of the pump-probe wavelength combination and interpulse delay characteristic of each colour. Such parameters served to separate the blue pigments from quinacridone red. Then, virtual cross-sections were obtained by combining the enface xy images (perpendicular to the beam axis) acquired at different depths (z direction).

Using the same approach, nonlinear pump probe microscopy was applied to a real case, a 14th century painting and on iron oxide based earth pigments in ancient pottery,[25] after chemical characterization of components. The main results are reported in Fig. 10. A pump-probe delay dataset was acquired using a combination of wavelengths (710 and 810 nm), and a false-coloured image was created. A pump-probe volume dataset was taken with a fixed 0.2 ps delay. Four different materials were detected and false colours were assigned according to the signal delay: cyan for negative signal (corresponding to lapis lazuli), red and yellow for positive (iron oxide/mordant and gold, respectively).

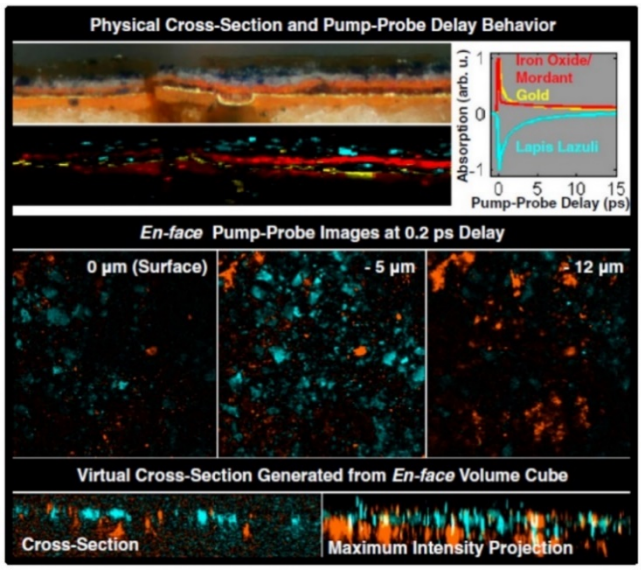

Fig. 10. Up-left: optical microscope cross-section of the painting layer in comparison with the false-coloured image created on the basis of the pump-probe delay showing lapislazuli (cyan), iron-oxide (red) and gold (yellow) components. Up-right: graph showing the cumulative pump-probe traces of all identified pigments. Middle: enface pump-probe xy images (185×185 μm^2) acquired at different depth (surface; - 5 µm; - 12 µm). Bottom-left: xz slice taken from the volume data showing a positive component mixed within the lapis lazuli layer (most likely iron oxide) with another positive component underneath (most likely gold and possibly, underlying mordant). Bottom-right: maximum intensity projection of the entire volume cube highlighting the composition. (T. E. Villafana *et al.* 2014)

2.6. Laser degradation effects in nonlinear microscopies

Main advantages and disadvantages of nonlinear techniques in the analysis of artworks were reported by Liang *et al.* in 2017,[26] focusing on the degradation effects induced in painting materials by the irradiation used in nonlinear microscopies. Specifically, different laser intensities were applied on painting materials showing absorption at the wavelength used. Possible damage due to high laser intensities resulted significantly influenced by the different absorption properties. Photo-damage effects were found to be more common in paint layers, since most pigments absorb the excitation wavelength commonly used for nonlinear applications (typically up to 1200 nm), whereas high transparent media, like protective layers (varnishes and glues), underwent negligible alterations when examined through nonlinear techniques. The fluorescence emitted by painting materials was attributed to a combination of single and multi-photon absorption processes, in contrast to protective layers, where multi-photon absorption is the predominant process.

Differently, the risk of photo-damage is negligible in case of coherent scattering nonlinear phenomena, such as harmonic generation processes (SHG and THG), since they do not imply energy deposition in the medium, with subsequent minimal sample disturbance. The new photons are generated through a single step quantum process, the interacting material acting as an energy converter for the incident photons. However, the same high intensity beam causing harmonic generation may also be absorbed by the medium through Multi-Photon Excitation Fluorescence, thus eventually causing photo-damage.

It is worth underlining that, by setting the laser power under the damage threshold, which can be determined through experimental measurements on samples, it is feasible to acquire nonlinear signals with sufficiently high Signal-to-Noise Ratio (SNR), without causing any damage to the sample (see results in Part 2). Moreover, depending on the objective lens and excitation wavelength

used, the size of laser spot ranges from one to few microns, thus reducing the possible area of damage. Concerning MPEF analysis reported in this thesis, the efficiency of the excitation wavelength and the laser power under the threshold of damage was defined for each paint.

References

[1] R. Gueta, E. Tal, Y. Silberberg, I. Rousso, The 3D structure of the tectorial membrane determined by second-harmonic imaging microscopy, J. Struct. Biol., 159, 103–110 (2007).

[2] P. J. Campagnola, A. C. Millard, M. Terasaki, P. E. Hoppe, C.J. Malone, W. A. Mohler, Three-dimensional high-resolution second-harmonic generation imaging of endogenous structural proteins in biological tissues, Biophys J 82, 493–508 (2002).

[3] D. A. Dombeck, M. Blanchard-Desce, W. W. Webb, Optical recording of action potentials with second-harmonic generation microscopy, J Neurosci 24:999–1003 (2004).

[4] J. Squier and M. Müller, High resolution nonlinear microscopy: A review of sources and methods for achieving optimal imaging, Rev. Sci Instt. 72, 2855 (2001) doi: 10.1063/1.1379598.

[5] E. J. Gualda, G. Filippidis, G. Voglis, M. Mari, C. Fotakis, N. Tavernarakis, In vivo imaging of cellular structures in Caenorhabditis elegans by combined TPEF, SHG and THG microscopy, J Microsc 229:141–150 (2008).

[6] D. Debarre, W. Supatto, A.M. Pena, A. Fabre, T. Tordjmann, L. Combettes, M. C. Schanne-Klein, E. Beaurepaire, Imaging lipid bodies in cells and tissues using third-harmonic generation microscopy, Nature Methods 3:47 53 (2006).

[7] W. Denk, J. H. Strickler, Two-photon laser scanning fluorescence microscopy, Science, 248: 73–76 (1990) doi: 10.1126/science.2321027.

[8] A. Diaspro, P. Bianchini, G. Vicidomini, M. Faretta, P. Ramoino, C. Usai, Multi-photon excitation microscopy, BioMed.Eng. OnLine, 5, 36 (2006).

[9] G. Filippidis, E. J. Gualda, K. Melessanaki, and C. Fotakis, Nonlinear imaging microscopy techniques as diagnostic tools for art conservation studies, Opt. Lett., Vol. 33, No. 3 (2008).

[10] E. J. Gualda, G. Filippidis, K. Melessanaki, C. Fotakis, Third Harmonic Generation and Multi Photon Excitation Fluorescence imaging microscopy techniques for the online art conservation diagnosis, Appl. Spec., 63, 280, (2009).

[11] A. Nevin, D. Comelli, I. Osticioli, G. Filippidis, K. Melessanaki, G. Valentini, R. Cubeddu, C. Fotakis, Multi-photon excitation fluorescence and third-harmonic generation microscopy measurements combined with confocal Raman microscopy for the analysis of layered samples of varnished oil films, Appl. Phys. A 100, 599–606 (2010) doi:10.1007/s00339-010-5644-x.

[12] G. Filippidis, M. Mari, L. Kelegkouri, A. Philippidis, A. Selimis, K. Melessanaki, M. Sygletou, C. Fotakis, Assessment of in-depth degradation of artificially aged triterpenoid paint varnishes using nonlinear microscopy techniques, Microsc. Microanal 21, 510–5175 (2015) doi:10.1017/S1431927614013580.

[13] N. S. Cohen, M. Odlyha, R. Campana, G. M. Foster, Dosimetry of paintings: determination of the degree of chemical change in museum exposed test paintings (lead white tempera) by thermal analysis and infrared spectroscopy. Thermochim Acta 365, 45–52 (2000).

[14] D. Saunders, L. Kirby, A comparison of light-accelerated ageing regimes in some galleries and museums, Conservator 25, 95–104 (2001).

[15] G. Filippidis, K. Melessanaki, C. Fotakis, Second and third harmonic generation measurements of glues used for lining textile supports of painted artworks, Anal. Bioanal. Chem. (2009) doi: 10.1007/s00216-009-3060-x.

[16] A. Selimis, P. Vounisiou, G. J. Tserevelakis, K. Melessanaki, P. Pouli, G. Filippidis, C. Beltsios, S. Georgiou and C. Fotakis, In-depth assessment of modifications induced during the laser cleaning of modern paintings, SPIE Europe 2009 Optical Metrology O3A (2009.

[17] P. Vounisiou, A. Selimis, G. J. Tserevelakis, K.Melessanaki, P. Pouli, G. Filippidis, C. Beltsios, S. Georgiou, C. Fotakis, The use of model probes for assessing in-depth modifications induced during the laser cleaning of modern paintings, Appl. Phys. A, 100: 647–652 (2010) doi: 10.1007/s00339-010-5647-7.

[18] G. Filippidis, G. J. Tserevelakis, A. Selimis, C. Fotakis, Nonlinear imaging techniques as non-destructive, high-resolution diagnostic tools for cultural heritage studies, Appl. Phys. A (2014) doi:10.1007/s00339-014-8357-8.

[19] M. Oujja, S. Psilodimitrakopoulos, E. Carrasco, M. Sanz, A. Philippidis, A. Selimis, P. Pouli, G. Filippidis, M. Castillejo, Nonlinear imaging microscopy for assessing structural and photochemical modifications upon laser removal of dammar varnish on photosensitive substrates, Phys. Chem. Chem. Phys., 19, 22836 (2017) doi: 10.1039/c7cp02509b.

[20] D. Ciofini, M. Oujja, M. V. Canamares, S. Siano, M. Castillejo, Spectroscopic assessment of the UV laser removal of varnishes from painted surfaces, Microchem. J., 124, 792 (2016).

[21] G. Latour, J.-P. Echard, M. Didier, M.-C. Schanne-Klein, In situ 3D characterization of historical coatings and wood using multimodal nonlinear optical microscopies, 20, 22, Optics Express 24623, (2012).

[22] F. Faraldi, G. J. Tserevelakis, G. Filippidis, G.M. Ingo, C. Riccucci, C. Fotakis, Multi photon excitation fluorescence imaging microscopy for the precise characterization of corrosion layers in silver-based artifacts, Appl. Phys. A, 111:177–181 (2013) doi:10.1007/s00339-013-7548-z.

[23] T. E. Villafana, W. P. Brown, J. K. Delaney, M. Palmer, W. S. Warren, M. C. Fischer, Femtosecond pump-probe microscopy generates virtual cross-sections in historic artwork, Stanford University (CA) PNAS, 111, 5, 1708–1713 (2014).

[24] T. Ye, D. Fu, W. S. Warren, Nonlinear absorption microscopy, Photochem Photobiol 85(3):631–645 (2009).

[25] T. E. Villafana, W. Brown, W. S. Warren, M. Fischer, Ultrafast Pump-Probe Dynamics of Iron Oxide Based Earth Pigments for Applications to Ancient Pottery Manufacture, Optics for Arts, Architecture, and Archaeology, Proc. of SPIE Vol. 9527, 952709 (2015) doi: 10.1117/12.2184758.

[26] H. Liang, M. Mari, C. S. Cheung, S. Kogou, P. Johnson, and G. Filippidis, Optical coherence tomography and non-linear microscopy for paintings – a study of the complementary capabilities and laser degradation effects, Opt. Express (2017), 2519640-19653.

PART 2. Nonlinear measurements and results

On the basis of the previous applications on Cultural Heritage, a systematic study for testing the potential of nonlinear optical techniques in probing paintings was performed. Analyses were complemented with a set of linear techniques for the chemical and physical characterization of a variety of materials, including pigments dispersed in different binders, protectives, glues and wood.

1. Protectives and consolidants

1.1. Introduction

Mechanical properties and aesthetic appearance of painted artworks may be significantly compromised by structural discontinuities, detachments and chemical alteration of the superficial layers due to aging and environmental agents. The cohesion and adherence among the constituting materials is commonly restored through the application of an adhesive material, called *consolidant*, which is generally injected inside the damaged layers. Furthermore, to prevent the paint layer from deterioration, as well as to improve its aesthetic appearance,[1] a thin film of transparent material (*protective* or *varnish*) is often laid or vaporized over the surface. A variety of natural and synthetic polymeric materials have been used in the past and are still routinely employed for the consolidation and protection of paintings.

Acting as the interface between the painting and the environment, varnishes are strongly susceptible to chemical alterations due to photo-oxidation, leading to loss of flexibility and darkening/yellowing of the material, with a subsequent decrease of transparency and legibility of the under-surface.[2,3] It is then common to partially or totally remove the altered varnish and to replace it with

a new transparent material.[4] The knowledge of the thickness of the layer to remove can support the cleaning operation, as well as provide a scientifically supported monitoring of the removal. At present, OCT is one of the most established techniques for non-invasive in-depth analysis of paintings.[5,6] It provides cross sectional views (tomograms) of layers showing moderate absorption and/or scattering properties to the probing light, with axial resolution ranging from 1 to 10 μm. Making use of low intensity radiation, usually below 2 mW at the surface of the object,[7] the examination is non-contact and harmless to all known types of artworks. The major constraint of OCT concerns the limited visibility inside objects composed by materials with low transparency to the incident laser wavelength.[7] Nonlinear microscopy modalities may represent a promising alternative to OCT, enabling major penetration capability and sensitivity with the use of pulsed fs-lasers and high-numerical aperture objectives. In this work, the sensitivity of THG analysis in the detection of signals generated at the interfaces between materials with similar refractive indexes was investigated and the results were compared, in terms of resolution and contrast, with those obtained by means of OCT. For the analysis, six transparent and semi-transparent materials were selected among the most widespread used protectives and consolidants: mastic and dammar varnishes (Zecchi©, Firenze), synthetic varnish (DV3410Z, Zecchi©, Firenze), Vinavil®, yolk, and beeswax.

Both THG and OCT are stratigraphic techniques based on the detection of signals generated in correspondence of the interfaces between different media – i.e. when the incident radiation experiences a refractive index mismatch. The main difference between the two techniques concerns the type of interaction between the laser beam and the medium. THG analysis is a result of a frequency-tripling process involving coherent light-scattering at the interfaces

between materials with third-order nonlinear susceptibility. Due to the refractive index mismatch between air and the medium, the axial dimensions of the THG image result compressed and have to be corrected to measure the real thickness. This is commonly obtained by multiplying the distance measured between two detected interfaces – i.e. apparent thickness – by the refractive index *n* of the analysed materials. Differently, in OCT, the incident radiation is linearly back-scattered by the material, and the optical interference is observed whenever the signal superposes with the reference beam, within the coherence length of the used light source. In this case, the n-mismatch causes a delay of the optical delay path of the reference beam and, therefore, the optical measured distances must be corrected to geometrical distances by dividing by the refractive index of the material (scheme reported in App. 1, Fig. 1).

1.2. Materials

Dammar and mastic resins are complex mixtures of compounds, mainly triterpenoids, which are extracted from the *dipterocarpaceae* tree and *Pistacea lentisca* tree, respectively. Small amounts of hydrocarbon polymers and sesquiterpenoids may be also present.[8] Triterpenoids are alicyclic terpenoid derivatives of triterpene organic molecules[x] consisting of six units of isoprene (C_5H_8). The two resins are characterized by very similar refractive indexes, ranging between 1.52–1.54 in the visible spectral range.[4,9]

The chemical composition of synthetic varnish was provided by the manufacturer (Zecchi©). The 60% of the material is composed of C_9-C_{12} hydrocarbons (n-alkanes, isoalkanes, cyclic, 2% aromatics) and a small fraction of 1-methyl-2-methoxyethyl acetate. Based on similar varnishes, the refractive index is assumed to be around 1.5 for this material.

[x] Terpenoid resins are composed of terpene molecules and can be categorized in two groups, depending on their chemical composition: diterpenoids and triterpenoids.

Vinavil is an aliphatic synthetic glue, obtained with the free radical polymerization of the vinyl acetate monomer, to produce polyvinyl acetate (PVAc). As an emulsion in water, PVAc is used as adhesive for porous materials, especially for wood and paper. The refractive index of Vinavil is around 1.48 for visible light.[5]

Egg yolk is a mixture of particulate granules (mainly proteins, carbohydrates and vitamins) and soluble plasma (low-density globules of unsaturated and saturated acids). Lipoproteins (specifically lipovitellin and lipovitellenin) represent the 70% of yolk solids.[10] The refractive index of yolk for visible light is around 1.35.[11]

Beeswax is a complex mixture of polyesters and hydrocarbons compounds. The main components are palmitate, palmitoleate, and oleate esters of long-chain (30–32 carbons) aliphatic alcohols. The refractive index of beeswax is around 1.45 for visible light.[12]

Considering the small differences in the refractive indexes of the analysed materials, the apparent thicknesses measured with both techniques were corrected for a refractive index between 1.45 and 1.55 for all samples, following what found in literature.[13]

The six materials were laid uniformly over glass cover-slips (140-150 μm thick) for enabling the transmission of THG signals, which were recorded in forward configuration. Materials were casted over the surface of each cover-slip inside two areas, delimited by a reference tape (superimposed layers of Kapton® tape, 50 μm thick) to obtain layers of different thickness and superimposed layers of different materials. In Fig. 1 the schematic representation of the samples (single-layered, SL, and multi-layered, ML) is reported.

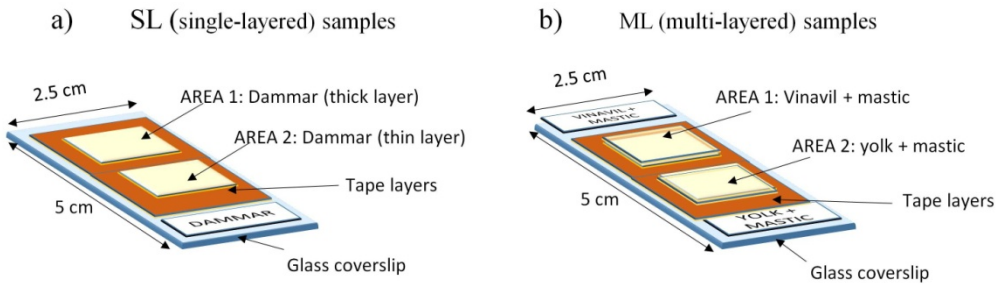

Fig. 1. Schematic representation of the (a) single-layered (SL) and (b) multi-layered (ML) samples prepared for THG and OCT analyses. The materials were casted in Area 1 and 2, delimited by the tape, to produce single layers of different thickness or double-layers by superposing two different materials (delimited by superimposed tape layers).

1.3. Measurements

Nonlinear analyses were performed using a nonlinear microscope developed at IESL-FORTH (Greece), comprising a fs laser (T-Pulse, Amplitude) with 1028 nm central wavelength, 50 MHz repetition rate, 800 mW power, 200 fs pulse duration. In this study, THG images were acquired with a 200 μm z-scanning and 1 μm sampling step on z axis. A detailed description of the setup is reported in Appendix 2.

OCT analysis was performed with a Time-domain confocal OCT prototype developed at INO-CNR (description of the setup in Appendix 1). For each sample, an OCT in-depth profile was acquired (25 mm length, 5 μm sampling step and 1 mm length, 1 μm sampling step in the y and z scanning directions, respectively), resulting in a 5000×1000 pixel tomogram. The signal generated at the glass support (visible at the borders of each cover-slip) was taken as a reference, assuming that 1 pixel corresponds to 1 and 5 μm on z and y axis of the tomographic image, respectively. For the multi-layered samples, the real thickness of the material was calculated by dividing the apparent thickness for the refractive index of the medium.

1.4. Results and discussion

OCT tomograms and THG images were acquired in the central area of each sample (Fig. 2) and are shown together for comparison in Fig. 3-6, after proper scaling. The results acquired on the thin and thick layers of the same material (synthetic varnish sample reported as an example in Fig. 2) enabled to compare the axial resolution of OCT and THG (Fig. 3a and b). Data obtained on the multi-layered samples (mastic + yolk and mastic + Vinavil) allowed for the comparison between the two techniques in detecting different superimposed materials (Fig. 4a and b).

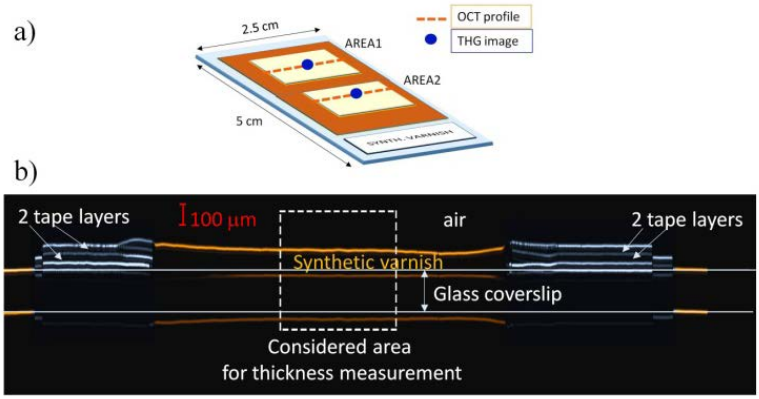

Fig. 2. a) Schematic of samples, showing the acquisition areas for OCT (tomographic image along the orange dashed line profiles) and THG (image centred on the blue circle); b) example of OCT image on synthetic varnish layer for thickness measurements with the dashed-line rectangle highlighting the area surveyed with THG.

The interfaces air/material, material/glass, glass/air (from top to bottom) resulted clearly visible in the XZ images acquired by means of the two techniques on all the analysed samples. To facilitate the comparison between OCT and THG images, the normalized signals intensities are reported in graphs as a function of depth on the right side of Fig. 3 and 4. Blue and orange lines for

THG and OCT signals, respectively, show the peaks of intensity in correspondence of the interfaces encountered by the incident radiation. The apparent thickness of the analysed material is measured as the distance between two consequent intensity peaks (air/material and material/glass interfaces). In THG, such value is multiplied by the refractive index of the material to obtain the real thickness, whereas the value obtained with OCT is divided by the refractive index. Since the signal generated at the interface material/glass was not always clearly visible in OCT tomograms, the borders of the glass cover-slip not covered by the resin were taken as a reference for measuring the real depth – i.e. the real thickness of the superimposed material. In the case of multi-layered samples, the thickness of the upper material layer was divided by its refractive index, as well as the distance between the peaks of signal coming from the upper and lower surfaces of the glass cover-slip.

Thickness values of all the analysed samples are summarized in Table 1, revealing an optimal correspondence among the results provided by the two techniques, not only in terms of sensitivity and signal intensity, but also axial resolution.

Basing on these results, the performance of OCT and THG for in-depth analysis of protectives and consolidants laid on transparent support can be considered comparable. However, the possibility to measure larger areas with OCT (up to 2.5 cm with the current prototype, with respect to the few mm length of the THG acquisitions) makes this technique more suitable for real applications. Furthermore, being in this case the forward detection the only configuration possible for THG, this technique remains at present confined to the measurement of transparent materials. Further implementation is needed for enabling the application of THG on paintings.

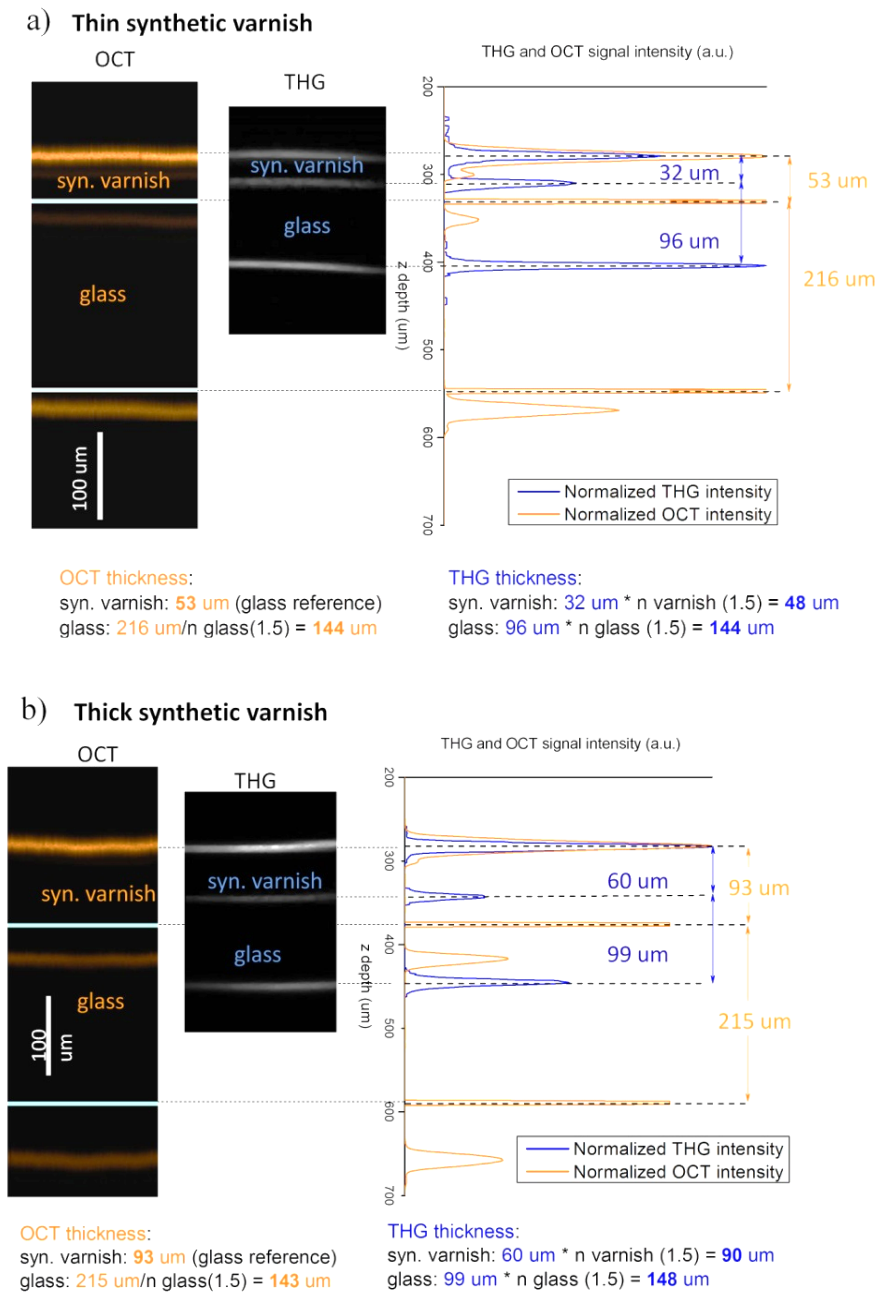

Fig. 3. OCT and THG images acquired on (a) thin and (b) thick layer of synthetic varnish sample. THG and OCT intensity signal as a function of depth (blue line and orange line, respectively) is reported in the graph on the right. The apparent thickness– i.e. the distance between two peaks – is corrected for the refractive index of the material.

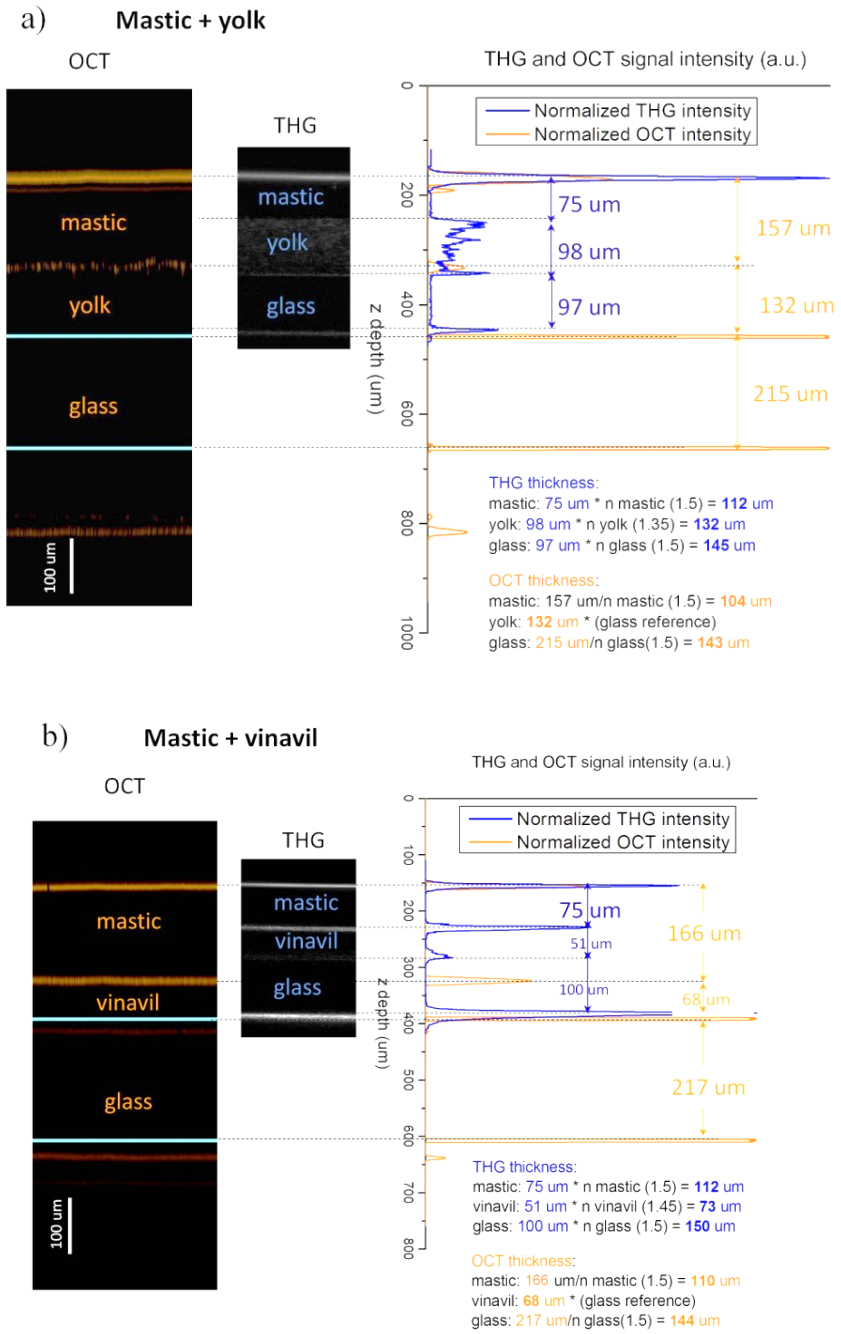

Fig. 4. OCT and THG images acquired on multi-layered samples: (a) mastic over yolk and (b) mastic over Vinavil. THG and OCT intensity signal as a function of depth (blue line and orange line, respectively) are reported in the graph on the right.

Table 1. Comparison between OCT and THG results acquired on all samples. Values are corrected for the refractive index of the analysed material.

			Real thickness (μm) corrected st. error = ± 5	
Sample	Area	**Material**	OCT	THG
SL1	1	Synthetic varnish	53	48
	2		93	90
SL2	1	Dammar	40	38
	2		265	261
SL3	1	Mastic	173	168
	2		375	383
SL4	1	Yolk	127	130
	2		172	178
SL5	1	Beeswax	58	55
	2		185	181
ML	1	Mastic	104	112
		Yolk	132	132
	2	Mastic	110	112
		Vinavil	68	73

References

[1] G. Filippidis, M. Mari, L. Kelegkouri, A. Philippidis, A. Selimis, K. Melessanaki, M. Sygletou, C. Fotakis, Assessment of in-depth degradation of artificially aged triterpenoid paint varnishes using nonlinear microscopy techniques, Microsc. Microanal. 21, 510–5175 (2015).

[2] E. R. De la Rie, Fluorescence of paint and varnish layers, Stud. Conserv. 32, 1 (1987).

[3] M. Elias, P. Cotte, Multispectral camera and radiative transfer equation used to depict Leonardo's sfumato in Mona Lisa, Appl. Opt. 47, 2146 (2008).

[4] A. Nevin, D. Comelli, I. Osticioli, G. Filippidis, K. Melessanaki, G. Valentini, R. Cubeddu, C. Fotakis, Multi-photon excitation fluorescence and third-harmonic generation microscopy measurements combined with confocal Raman microscopy for the analysis of layered samples of varnished oil films, Appl. Phys. A, 100: 599–606 (2010).

[5] C. S. Cheung, M. Spring, H. Liang, Ultra-high resolution Fourier domain optical coherence tomography for old master paintings, Opt. Express 23, 10145–10157(2015).

[6] P. Targowski, M. Iwanicka, B. J. Rouba, C. Frosinini, OCT for examination of artwork, in: W. Drexler, G. Fujimoto (Eds.), Optical Coherence Tomography. Technology and Applications, Springer, Cham Heidelberg New York Dordrecht London, pp. 2473–2495 (2015).

[7] P. Targowski, M. Iwanicka, Optical Coherence Tomography: its role in the non-invasive structural examination and conservation of cultural heritage objects - a review, Appl. Phys. A, 106:265–277 (2012).

[8] P. Dietemann, C. Higgitt, M. Kalin, M. J. Delmann, R. Knochenmuss, R. Zenobi, Aging and yellowing of triterpenoid resin varnishes – Influence of aging conditions and resin composition, J. Cult. Herit., 10, 30–40 (2009).

[9] G. Filippidis, E. J. Gualda, K. Melessanaki, C. Fotakis, Nonlinear imaging microscopy techniques as diagnostic tools for art conservation studies, Opt. Lett., 33, 3 (2008).

[10] T. L. Parkinson, The chemical composition of eggs, J. Sci. Fd Agric., 17 (1966).

[11] M. Doerner, The Materials of the Artist, Harcourt, Brace & Company (1934).

[12] B. Tesfaye, D. Begna, M. Eshetu, Analysis of Physico-Chemical Properties of Beeswax Produced in Bale Natural Forest, South-Eastern Ethiopia, Eur. Biophys. J, 4, 5, 42-46 (2016).

[13] C. S. Sherrer, S. Zumbuehl, F. Delavy, A. Fritsch, R. Kuehnen, Spectrochim. Acta, Part A, 2009, 73, 505–524, doi.org/10.1016/j.saa.2008.11.029.

2. Wood

2.1. Introduction

Wood has been used in artworks production with both structural and decorative function in a variety of objects, ranging from sculptures to substrates in paintings and musical instruments. In the last decades, a number of diagnostic techniques have been applied for the visualization of wood micro-structures and for the identification and quantification of chemical components, which may turn significant for the differentiation of wood species. Degradation is also related to micro-structural features, which become a key parameter to the characterization of the objects' state of conservation.[1] Furthermore, the distribution of specific components – e.g. cellulose – may influence the macro-mechanical properties of wood and its sensitivity to micro-environmental changes.[2] .

The structure of wood basically consists of cells growing in the axis of the trunk (fibres) and developing along the perpendicular direction (medullar rays) from the core to the bark of the tree (Fig. 1a).[3] The arrangement and morphological characteristics of cells determine the anatomical differences between softwoods – i.e. gymnosperms (mostly conifers) – and hardwoods – i.e. angiosperms (flowering plants).[4] The major contribution to the physical and chemical properties of wood is given by tracheids and fibres, which are the main cell types of softwood and hardwood, respectively. In softwoods, around the 90% of the volume consists of tracheids, mainly composing the axial system. The latewood (*summer wood*) can be distinguished from the earlywood (*spring wood*) for its smaller radial dimensions and thicker cells walls, reflecting also in wood density. The rays, constituting the radial or horizontal system, are composed mostly of ray parenchyma cells.[5] Differently from softwood species, hardwoods' axial system presents a variety of cells types (Fig. 1b),

such as vessels (pores), parenchyma, and fibres, whose size, arrangement, pattern and abundance are related to wood macroscopic properties as well. A further diagnostic element for the recognition of wood species is the presence of isolated interruptions inside the cell walls, called *pits*, connecting different cells for the transfer of liquids. Shape and dimension of pits may significantly vary depending on the type of the adjacent cells.

The plant cell is characterized by a globular, more or less elongated bag-shape, with a membrane, the cell wall, consisting of different layers (Fig. 1c): the primary (P) is formed during the surface growth of the cell wall; the secondary (S), growing during the thickening of the wall, is in turn composed of three sub-layers, S1, S2, and S3. The S2 sub-layer may reach a thickness of 5 μm and it is primarily responsible for the physical characteristics of the cell wall. Adjacent cells are connected by an additional layer, called Middle Lamella (ML). ML and the two adjacent P layers are generally difficult to differentiate, forming the Compound Middle Lamella (CML).[1]

A complex chemical matrix of more or less amorphous polysaccharides constitutes the molecular structure of cell walls (Fig. 1d). Highly crystalline micro-fibrils of cellulose are coated with hemicelluloses and pectin (chains of glucans, mannans, and arabinans units), and embedded in a lignin-hemicellulose matrix.[6] While the content of cellulose is more or less the same in both softwood and hardwood species, lignin is present in different quantities depending on the wood group, usually ranging between 18% and 25% in hardwoods, and between 25% and 35% in softwoods.

Cellulose is a linear chain of polysaccharidic molecules – up to 10.000 D-glucose unites, linked by β (1-4) glicosidic bonds – predominantly located in the secondary cell wall. Cellulose approximately reaches the 40-45 % in weight of the dry matter in most of wood species. The crystalline parts of cellulose display one chain conformation, made up of a twofold ribbon.

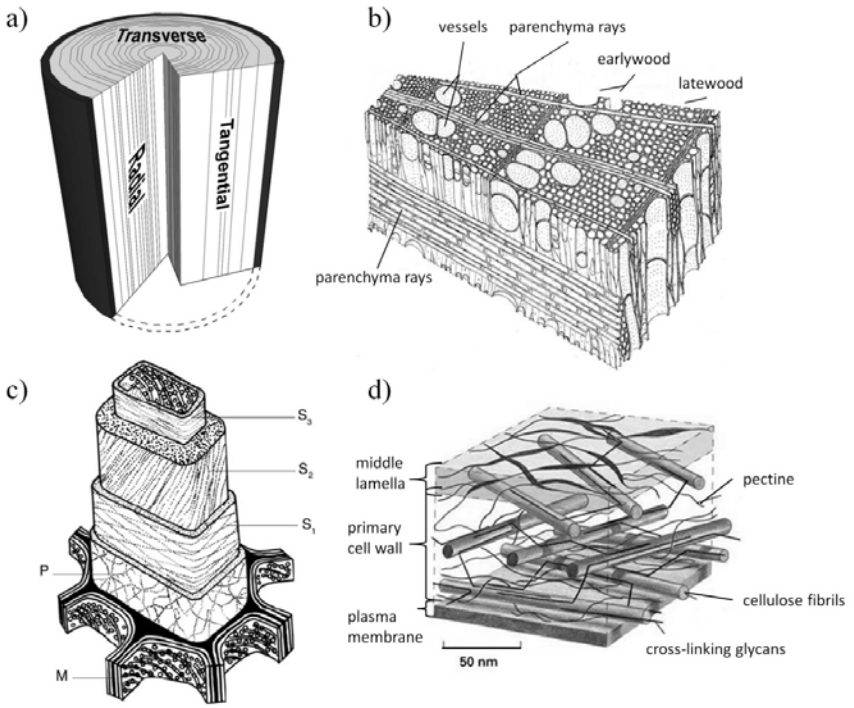

Fig. 1. a) Wood sections (modified from Latour, 2009); b) schematic structure of hardwood (modified from Berti, 2006); c) schematic representation of cell wall layers of a tracheid – M, middle lamella; P, primary cell wall; S_1 S_2, S_3, sub-layers of secondary cell wall (modified from W.A. Cotè, "Wood Ultrastructure – an atlas of electron micrographs"); d) scheme of wood cell's internal structure.

Many packing arrangements are possible, all classifiable in cellulose I (the more abundant, with parallel chains) and II (antiparallel chains).[7] Cellulose I naturally occurs in two distinct crystalline forms, I_α and I_β, showing triclinic and monoclinic symmetry, respectively. These well-ordered molecular chains are present in variable proportions and are organized in microfibrils, with typical diameter ranging from 1.2 to 4.8 nm, and length between 60 and 150 nm.[8] Both the hierarchical structure and the parallel orientation of the molecular chains of cellulose may enable the emission of Second Harmonic Generation signal. The distribution of the microfibrils differs in quantity and arrangement

depending on its location, being more abundant in the sub-layer S2, with respect to S1 and S3.

Another possible source of SHG signal is starch, which is stored as long-term carbon reserves in a wide variety of organs, such as seeds and tubers, and on a temporary basis in the photosynthetic tissues, specifically in the chloroplasts. Starch presents two forms: amylose, long chains of 1:4 linked glucose residues, and amylopectin, shorter chains of 1:4 glucans with branches introduced by a 1:6 linkages. Especially amylose is often highly crystalline and therefore likely to generate second-harmonic signal.[9]

In woody tissues, resistance and rigidity are given by lignin, a complex phenolic compound, which represents the 18-25% and the 25-30 % of the total wood weight in hardwoods and softwood, respectively. Lignin in plant cell shows a strong multi-photon excited fluorescence, which may be enhanced by resonance effects.[9] While lignin is the predominant fluorophore in tracheid cell walls, the polysaccharide components, such as cellulose and starch, are considered to be not fluorescent.[10] Lignin shows a broad range of fluorescence emissions and can be excited with both UV and visible light, emitting blue, green and red fluorescence.[11] This property makes lignin a good emitter of multi-photon excitation fluorescence.[12]

In the last years, nonlinear imaging modalities – mainly MPEF and SHG – have been introduced for the analysis of plant materials, providing key information for the identification of wood microstructures. Among the others, Mizutani *et al.*[13] imaged starch grains in living algal cells by SHG, using a pulsed neodymium laser at 1064 nm. Chu *et al.*[14] used a stage-scanning microscope with chromium forsterite laser at 1230 nm for generating 3D harmonic images of plant cells. Cox *et al.*[9] applied both SHG and 2PEF imaging using a Titanium-sapphire laser with shorter wavelength - between 800 and 850 nm. They found that SHG signals from cellulose are not as strong as in starch, due

to the reverse orientation of glucose residues in the polysaccharidic chains. Specifically, the imaging of cellulose requires rather high laser powers (above optimal values for live cell imaging), whereas starch can be easily imaged at laser fluences compatible with extended cell viability. Moreover, the SHG signal of macromolecular structure of purified cellulose samples was found to be significantly similar to that of collagen from animal tissues, both in terms of morphology and polarization anisotropy.[15] It was also observed that the emission of the signal is strongly dependent on the orientation of the cellulose microfibrils, predominantly developing along the axis of longitudinal arrays of cells.[16] Hence, the use of nonlinear techniques based on polarization-resolved approaches may be exploited to obtain quantitative information, which would turn useful for comparison among different wood species or for studying the effects of treatment or aging on wood microstructure. Furthermore, the acquisition of nonlinear signals in the backward direction enables both the analysis of samples of any thickness, and *in situ* measurements, which is a common requirement in artworks diagnosis. While the backward detection is effective in case of isotropically emitted signals (MPEF), SHG emission is generally more efficient in the forward direction, due to phase-matching conditions. Nevertheless, it has been observed that SHG can be also recorded in the backward direction, in case of signal enhancement, by specific structures or backscattered in thick scattering samples, like wood microstructures.[17] Moreover, Latour *et al.* (2012)[1] demonstrated that well-resolved and well-contrasted 2PEF/SHG images can be obtained with an air objective rather than water-immersion objectives (commonly used in the biomedical field), thus preserving the liquid-sensitive and sometimes porous artworks' materials from damage.

To the best of our knowledge, the first 3D imaging of wood microstructures on a real artwork was performed by Latour *et al.* in 2009,[3] with a purposely

developed full-field time-domain OCT system, reaching axial and transverse resolution of 1.5 and 1 μm, respectively. Nevertheless, the use of red (visible) light, while enabling the visualization of wood fibres, rays, cells, lacked in providing any chemical information. To overcome such limit, some years later, the same author applied nonlinear imaging microscopies for the micrometric analysis of an historical violin (see p. 45-46).

In this study, the application 2PEF-SHG imaging has been expanded to three hardwood species never analysed before with this modality – i.e. Poplar,[xi] Beech and Chestnut – which were selected on the basis of their wide use in Italian artistic production.

2.2. Materials

All wood fragments of Poplar, Beech and Chestnut were obtained by cutting the trunk in the longitudinal-tangential direction (see Fig. 1a), with a size of around 15×10×5 mm^3. After a week from the extraction, measurements were performed in backwards configuration, and, to respect the non-invasiveness constraints in artworks diagnosis, they were analysed without any treatment, even if the addition of water or a solution of glycerine and water would have eased the observation of the microstructures.[6]

2.3. Measurements

The setup used for the analysis is the upgraded version of the nonlinear microscope developed at CNR-INO, equipped with a dual output Yb-based fibre fs-laser (Camaleon Discovery, Coherent Inc., Santa Clara, CA, US). A detailed description of the setup can be found in Appendix 2. Based on previous

[xi] Poplar is the wood species composing the support of the painting samples presented in section 3. *Painting layers*.

studies,[1] the excitation wavelength was set at 840 - 850 nm (depending on the wood species), with a pulse duration of 140 fs and a repetition rate of 80 MHz, with a power on the specimen ranging from 50 and 100 mW. Nonlinear signals coming from the sample were revealed with a detection system based on two photomultiplier tubes (Hamamatsu H7422). The filter used for the SHG detection is Semrock 420/10 nm BrightLine single-band bandpass filter, while MPEF images were acquired with a long pass 452 nm Semrock, according to previous observation on 2PEF emission spectral range of lignin. For each analysed area, SHG and MPEF signals were detected and displayed in form of intensity images, which were merged together with a dedicated software as colour channels of the same image. Specifically, the SHG and the MPEF images were assigned to the red and the green channel, respectively, thus enabling the distinction among components generating different nonlinear signals (mainly starch, cellulose and lignin) in a single image, as well as allowing the visualization of micrometric features characteristic of each species.

2.4. Results and discussion

2.4.1. Poplar (Populus)

Poplar has cells of peculiar size and shape (Fig. 2 and 3). Vessels are generally small (50-100 μm – dimensions slightly vary between latewood and earlywood zones), with circular or polygonal shape, uniformly distributed inside the growth rings. Parenchyma rays are generally homogenous and mono-seriated (composed of one single series of cells), and pits between rays and vessels are bigger than in other wood species. The grey-scaled intensity images (Fig. 2a and b) are acquired without any optical filter, and thus do not allow the distinction between SHG and MPEF. The same micro-structures observed in these images, i.e. bordered pits organized in lines, probably connecting

tracheids and vessels, are also visible in the merged SHG/MPEF image (c), where the predominant nonlinear fluorescence (green) signal is indicative of the presence of lignin.

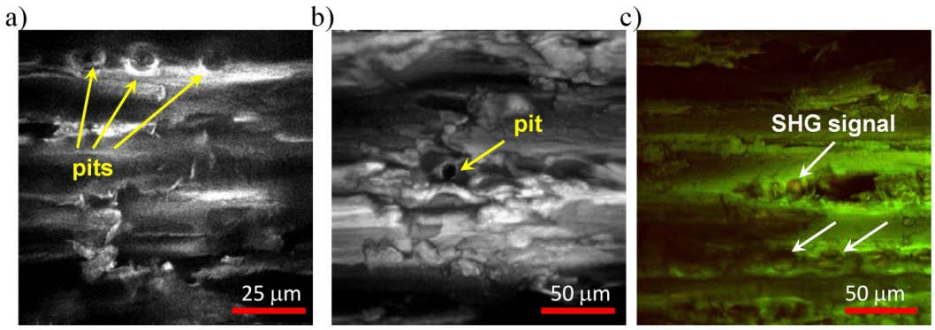

Fig 2. NL images of Poplar sample (excitation wavelength 840 nm). Bordered pits are pointed out by yellow arrows. Grey-scaled images a) 100×100 µm^2 and b) 200×100 µm^2 are acquired with no optical filters and, thus, show both SHG and MPEF signals, indistinctively. c) Merged image 200×100 µm^2 enabling the distinction between MPEF (green channel) and SHG (red channel, very weak) signals, attributed to lignin and starch, respectively.

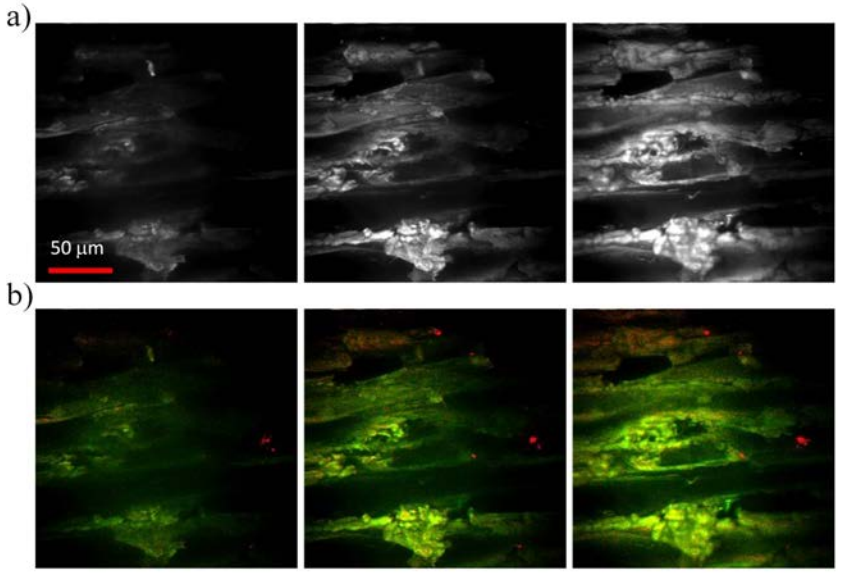

Fig 3. a) Poplar grey-scaled NL images (200×200 µm^2) and b) corresponding SHG/MPEF merged images acquired at different depth inside the wood slice (5 µm step) highlighting the presence of secondary harmonic emitters.

In Fig. 2 the SHG signal is almost absent, except for some traces (red) inside the pits (c) ascribable to starch, which is more likely to accumulate in these empty spaces than crystalline cellulose.

A slightly more intense SHG signal can be observed in the red areas of the combined SHG/MPEF stacks (Fig. 3a) acquired on the same poplar sample at different focusing depths (steps of 5 μm along the in-depth direction), in comparison with the respective grey-scaled images (Fig. 3b). In this case, the SHG is intense and confined to small spots, probably located in the secondary cell walls of tracheids. Weaker signals are distributed in the upper part of the analysed area.

2.4.2. Beech (Fagus sylvatica)

Vessels in Beech can be found isolated or in form of aggregates of 2-6 units, are generally numerous, uniformly distributed inside the growth rings, with size ranging between 50 and 75 μm. Pits between vessels are usually organized in horizontal lines, and those between rays and vessels are big and abundant. Rays, generally composed of several series of cells (up to 25), are clearly visible in three of the analysed areas, as shown in Figures 4a (size: 100×100 μm^2), 4b and 4c (size: 200×200 μm^2). The SHG/MPEF stacks of the same areas acquired at steps of 5 μm in depth are reported in Fig. 5. Differently from Poplar, SHG signal in Beech results diffused inside wood cells (red areas), especially inside rays and around the fibres. Possible sources of SHG are crystalline cellulose and especially starch (in form of crystalline amylose), which is generally abundant in Beech, specifically in the area underneath the bark (where this sample was extracted). Lignin is distributed in the secondary wall layers of fibres, closely following the direction of the cellulose microfibrils, which are as well responsible for the lamellar structure.[18]

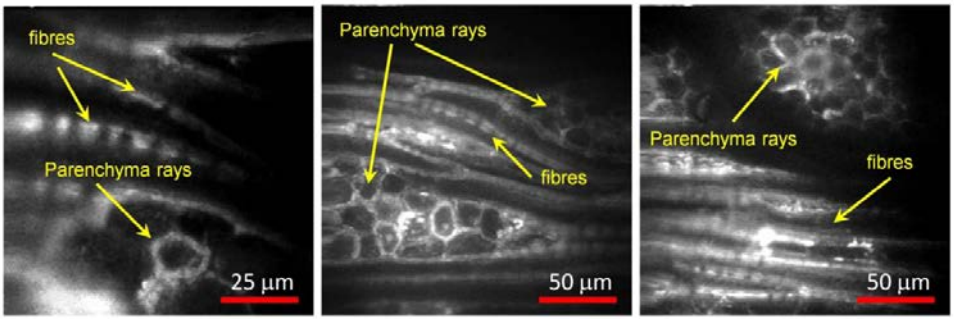

Fig. 4. Beech NL images (excitation wavelength 850 nm) showing the aggregates of parenchyma rays in transverse section and the fibres in tangential section. MPEF and SHG signals generated from lignin and cellulose/starch are both present (no filters used for this acquisition).

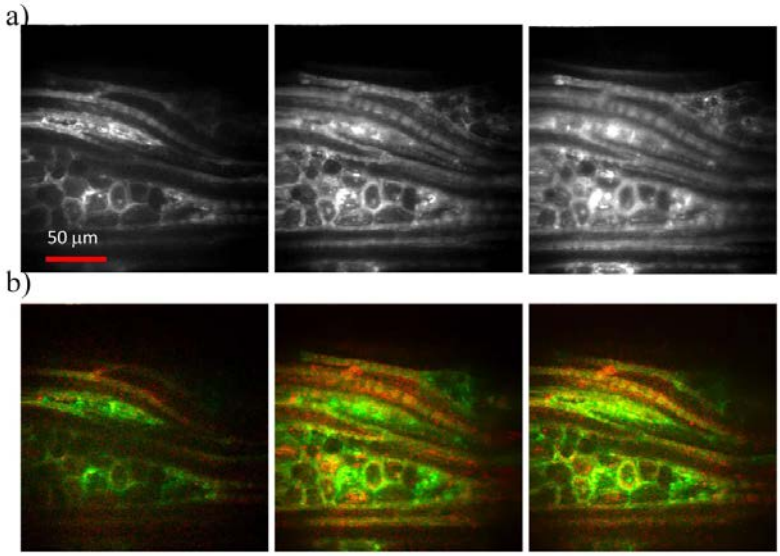

Fig 5. a) NL images (excitation wavelength 850 nm) and b) corresponding SHG/MPEF stacks of Beech acquired at steps of 5 µm in depth, showing the morphology of rays and fibres, as well as the distribution of SHG and nonlinear fluorescence emitters.

2.4.3. Chestnut (Castanea sativa)

Chestnut presents big vessels (300-500 µm) in the earlywood, forming porous circles, whereas vessels in the latewood are significantly smaller and arranged in oblique lines. With respect to the previously described species, pits between

cells in Chestnut are generally bigger. External deformations of parenchyma radial and axial cells, called *tyloses*, may partially occlude the adjacent vessels. Tyloses were observed in Chestnut samples, as shown in Fig. 6b, inside parenchyma rays in transverse section. SHG signal, possibly emitted by crystalline cellulose, was detected mainly in small aggregates, as it can be observed in Fig. 6a and c.

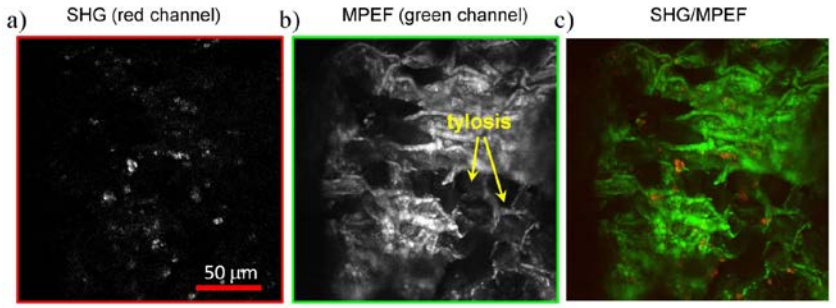

Fig. 6. (a) Chestnut SHG, (b) MPEF and (c) merged SHG/MPEF images (excitation wavelength 800 nm, FOV 200×200 µm^2, resolution 1024×1024 pixels). Tyloses are visible inside the parenchyma rays.

Second harmonic signal is also evident in the SHG/MPEF image (xy) with orthogonal views xz and yz (Fig. 7b), acquired with a scanning depth of 80 µm. Similar features can be observed in Fig. 8.

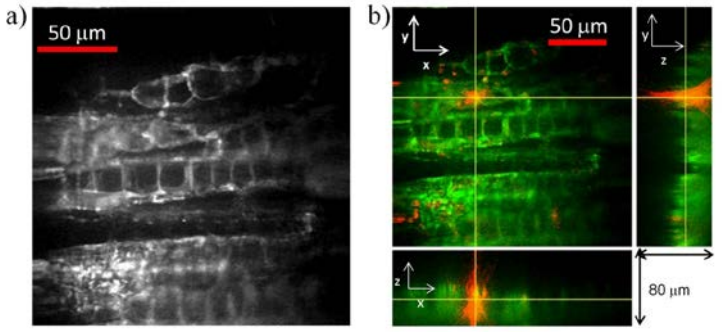

Fig. 7. (a) Grey-scale nonlinear intensity image of Chestnut, and (b) orthogonal views of SHG/MPEF merged image showing the presence of isolated aggregates of material strongly emitting SHG signal (red), and nonlinear fluorescence signal (green) generated by lignin.

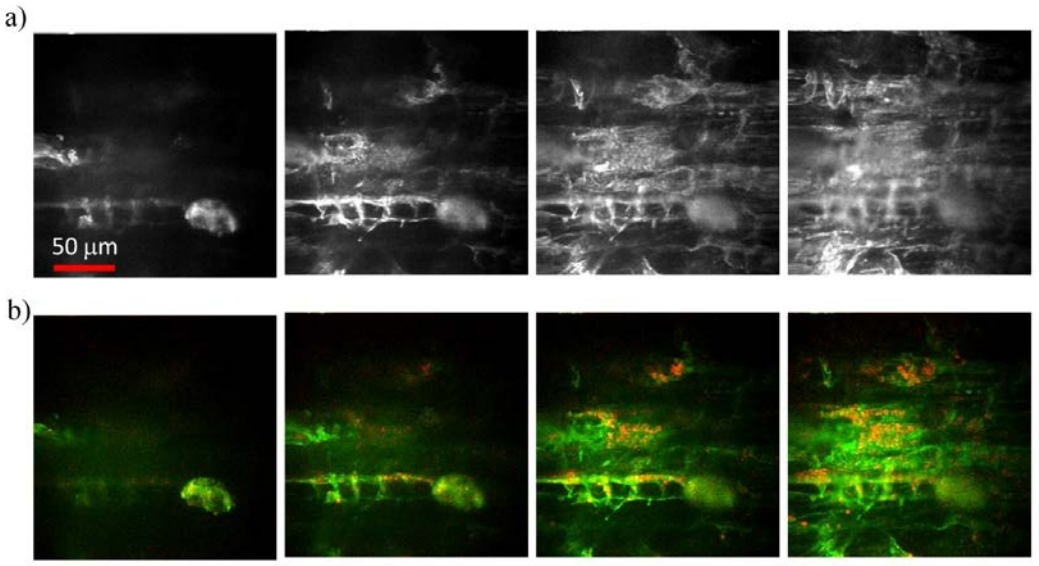

Fig. 8. (a) Chestnut grey-scale nonlinear intensity images obtained as an average of 15 simultaneous acquisitions (200×200 µm^2), with a z-step of 5 µm, in comparison with (b) MEPF/SHG images, showing the distribution of the nonlinear signals.

These results demonstrate that the combined application of SHG and MPEF imaging microscopy allows for the simultaneous visualization at the micrometre scale of different nonlinear signal emitters (starch, cellulose and lignin). Similar multimodal imaging has been performed with CARS microscopy by using C=C vibration at 1600 cm^{-1} as a lignin marker and C-O-C vibration at 1100 cm^{-1} as a cellulose marker.[19] However, implementation of CARS microscopy is not as straightforward as SHG and MPEF microscopies, which require only one femtosecond laser beam. SHG/MPEF imaging provides a simple means for 3D *in situ* mapping of wood cell walls at the micrometre scale, which may enable a significant insight into their organization. One possible perspective is to perform polarization-resolved SHG imaging to determine the orientation of cellulose microfibrils[20,21] and to improve their visibility in cell walls. The analysis of wood deterioration is also envisaged in

view of future application of SHG/MPEF imaging on wooden artworks, as well as the recognition of other wood species on the basis of the visualization of their micro-morphology.

References

[1] G. Latour, J.-P. Echard, M. Didier, M.-C. Schanne-Klein, In situ 3D characterization of historical coatings and wood using multimodal nonlinear optical microscopies, 20, 22, Opt. Express, 24623-24635 (2012) doi:10.1364/OE.20.024623.

[2] G. Latour, I. Gusachenko, L. Kowalczuk, I. Lamarre, and M. C. Schanne-Klein, In vivo structural imaging of the cornea by polarization-resolved second harmonic microscopy, Biomed. Opt. Express 3(1), 1–15 (2012) doi:10.1364/BOE.3.000001.

[3] G. Latour, J.-P. Echard, B. Soulier, I. Emond, S. Vaiedelich, and M. Elias, Structural and optical properties of wood and wood finishes studied using optical coherence tomography: application to an 18th century Italian violin, Appl. Opt. 48(33), 6485–6491 (2009).

[4] M.C. Popescu, C.M. Popescu, G. Lisa, Y. Sakata, Evaluation of morphological and chemical aspects of different wood species by spectroscopy and thermal methods, J. Mol. Struct., 988, 65–72 (2011) doi:10.1016/j.molstruc.2010.12.004.

[5] M. Fujita, H. Harada, Ultrastructure and formation of wood cell wall, in: D.N.S. Hon, N. Shiraishi (Eds.), Wood and Cellulosic Chemistry, Marcel Dekker (2001).

[6] S. Dammström, L. Salmén, P. Gatenholm, On the interactions between cellulose and xylan, a biomimetic simulation of the hardwood cell wall, BioRes, 4 (2009).

[7] A. Rencurosi, J. Rohrling, J. Pauli, A. Potthast, C. Jager, S. Pÿrez, P. Kosma, and A. Imberty, Polymorphism in the Crystal Structure of the Cellulose Fragment Analogue Methyl 4-O-Methyl-b–D-Glucopyranosyl-(1-4)-b–D–Glucopyranoside Angew. Chem. Int. Ed., 22, 41 (2002).

[8] S. Berti, M. Fioravanti, N. Macchioni, La struttura anatomica del legno ed il riconoscimento dei legnami italiani di più ricorrente impiego, Ed. Nardi Berti, CNE-INVALSA (2006)

[9] G. Cox, N. Moreno, and J. Feijó, Second-harmonic imaging of plant polysaccharides, J. Biomed. Opt. 10(2), 024013-6 (2005).

[10] L. A. Donaldson, K. Radotic, Fluorescence lifetime imaging of lignin autofluorescence in normal and compression wood, J. Microsc., 251, 2, 178–187 (2013) doi:10.1111/jmi.12059.

[11] D. Djikanović, A. Kalauzi, K. Radotić, M. Jeremić, Deconvolution of lignin fluorescent spectra: A contribution to the comparative structural studies of lignins, Russ. J. Phys. Chem. A 81: 1425–1428 (2007).

[12] I. Vazquez-Cooz and R. W. Meyer, Fundamental differences between two fibre types in Acer, IAWA J. 29, 129–141 (2008).

[13] G. Mizutani, Y. Sonoda, H. Sano, M. Sakamoto, T. Takahashi, and S. Ushioda, Detection of starch granules in a living plant by optical second harmonic microscopy, J. Lumin. 87, 824–826 (2000).

[14] S.-W. Chu, I.-H. Chen, T.-M. Liu, P. C. Chen, and C.-K. Sun, Multimodal nonlinear spectral microscopy based on a femtosecond Cr:forsterite laser, Opt. Lett. 26, 1909–11 (2001).

[15] A. C. Millard and P. J. Campagnola, Macromolecular structure of cellulose studied by second-harmonic generation imaging microscopy, Optic Letters 28, 22 (2003).

[16] I. Gusachenko, V. Tran, Y. G. Houssen, J.-M. Allain, and M.-C. Schanne-Klein, Polarization-resolved second-harmonic generation in tendon upon mechanical stretching, Biophys. J. 102(9), 2220–2229 (2012).

[17] D. Débarre, N. Olivier, and E. Beaurepaire, Signal epidetection in third-harmonic generation microscopy of turbid media, Opt. Express 15(14), 8913–8924 (2007).

[18] J. Fromm, B. Rockel, S. Lautner, E. Windeisen, and G. Wanner, Lignin distribution in wood cell walls determined by TEM and backscattered SEM techniques, Journal of Structural Biology 143 77–84 (2003) doi:10.1016/S1047-8477(03)00119-9.

[19] B.-C. Chen, J. Sung, and S.-H. Lim, Chemical imaging with frequency modulation coherent anti-Stokes Raman scattering microscopy at the vibrational fingerprint region, J. Phys. Chem. B 114(50), 16871–16880 (2010).

[20] R. M. Brown, Jr., A. C. Millard, and P. J. Campagnola, Macromolecular structure of cellulose studied by second-harmonic generation imaging microscopy, Opt. Lett. 28(22), 2207–2209 (2003).

[21] O. Nadiarnykh, R. B. Lacomb, P. J. Campagnola, and W. A. Mohler, Coherent and incoherent SHG in fibrillar cellulose matrices, Opt. Express 15(6), 3348–3360 (2007).

3. Painting layers

3.1. Introduction

MPEF analyses were performed on a number of samples simulating modern and ancient paints, by using three different nonlinear setups.[xii] Two sets of samples were prepared: the first, consisting of paint layers laid on glass cover slips; the second, more complex, realized by superposing different materials (varnishes and lacquers) over the paint, laid on a wooden support. Painting layers were prepared with two binders, acrylic and egg yolk, for simulating modern and ancient paintings, respectively. The chemical and optical characterization of pictorial materials through the multi-modal application of non-invasive optical techniques was a concurrent objective of this work. To this purpose, measurements were performed by means of several non-invasive modalities, including micro-Raman spectroscopy, Vis-NIR Fibre Optics Reflectance Spectroscopy (FORS), Laser Induced Fluorescence (LIF), and Scanning Multispectral Reflectography (SMR). The acquired dataset turned useful for the comprehensive interpretation of the nonlinear results, which are reported in the following sections. Then, the theoretical basis of the new Second Derivative Spline Distance (2DSD) approach for the interpretation of backwards detected MPEF z-responses is explained (§ 3.5.2), with a description of the procedure for the evaluation of the apparent thickness through the processing of the nonlinear fluorescence z-profiles. The correction formula to compute the real thickness of a material layer from the measured apparent one is also reported and demonstrated. Finally, the results obtained with different nonlinear setups and setting parameters are shown, starting from the single-layered samples and concluding with the multi-layered ones, in comparison with OCT analysis (paints on glass) and stratigraphic analysis (paints on wood).

[xii] CNR-INO, Florence; IQFR-CSIC, Madrid; IESL-FORTH, Heraklion, Crete.

3.2. Samples

3.2.1. Acrylic paints on glass support

The set consists of eighteen acrylic paints (Extra-fine acrylic colours, Maimeri Brera©, IT) laid on glass cover-slips (2.5×5 cm^2, 140 μm thickness). Commercial acrylic paints were chosen due to their wide diffusion in modern art, versatility, ease of use and speed of drying. The thickness of each paint layer was preliminarily assessed with OCT, resulting in the range of 22-65 μm. The acrylic tempera are listed in alphabetic order in Table 1, with relative acronyms, colour indexes and chemical composition (as declared by the manufacturer). Each pigment is referenced with two colour indexes, namely the generic name (GN) and constitution number (CN). According to the globally recognized *Colour Index Database*,[xiii] colour indexes are descriptors used for pigments classification to facilitate their identification in the industrial/commercial field. Differently, CIEL*a*b* coordinates[1-3] (reported in Fig. 1 with the bright-field images of the samples) are colorimetric parameters obtained by measuring the spectral reflectance factor with Fibre Optics Reflectance Spectroscopy (FORS) in the Vis spectral region with standard D65 illuminant and 2° observer. The selected paints show a variety of hues and chemical compounds, allowing for the acquisition of data on a representative and exhaustive dataset.

[xiii] Colour Index Database (Society of Dyers and Colourists and American Association of Textile Chemists and Colorists) - https://colour-index.com. Accessed in February 2018.

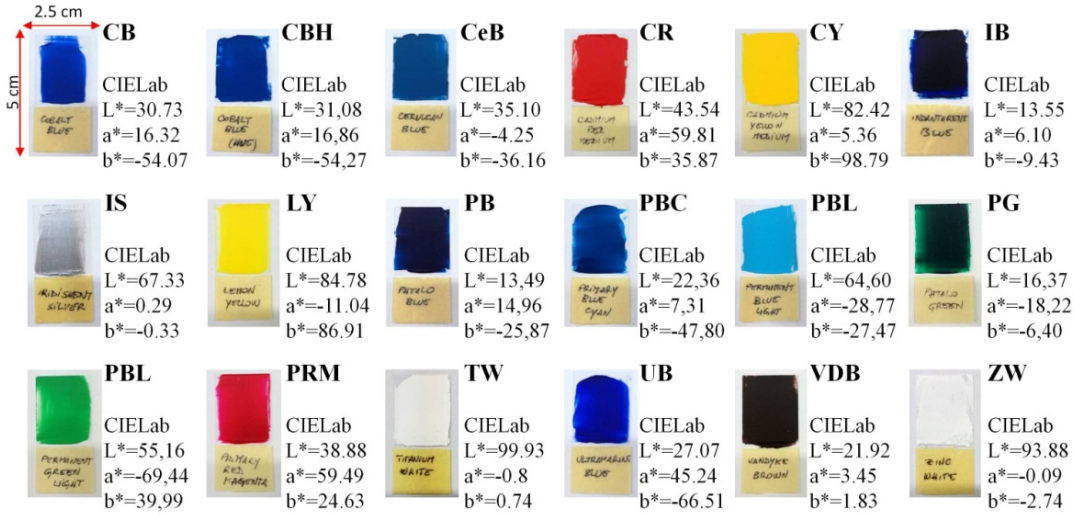

Fig. 1. Acrylic tempera paint layers applied on glass cover-slips. CIEL*a*b* values, computed from FORS measurements, are also reported (see text).

Table 1. Acrylic tempera paints (Maimeri Brera©) with the acronyms used through the text, commercial codes (colour indexes) and chemical composition declared by the manufacturer.

PIGMENT with acronym	**Chemical composition and commercial code (Maimeri Brera©)**
Cobalt Blue (CB)	**Cobalt(II) Aluminate** [$CoAl_2O_4$], inorganic, PB28 – 77346
Cobalt Blue (Hue) (CBH)	**Sodium Polysulphide-Aluminosilicate,** inorganic, PB29 – 77007**, Titanium Dioxide** [TiO_2], inorganic, PW6 – 77891**, Copper Phthalocyanine β** [$C_{32}H_{16}CuN_8$], inorganic, PB15:3 – 74160
Cerulean Blue (CeB)	**Cobalt, Chromium Oxide** [CoO, Co_2O_3, Co_3O_4; CrO,Cr_2O_3, CrO_2, CrO_3, CrO_5], inorganic, PB36 – 77343
Cadmium Red Medium (CR)	**Cadmium Selenide Sulphide** [Cd_2SSe], inorganic, PR108 – 77202
Cadmium Yellow Medium (CY)	**Cadmium Sulphide** [CdS], inorganic, PY35 – 77205
Indanthrene Blue (IB)	**6,15-Dihydro-5,9,14,18-anthrazinetetrone** [$C_{28}H_{14}N_2O_4$], organic, PB60 – 69800

Iridescent Silver (IS)	**Synthetic Iron Oxide** [Fe_2O_3], inorganic, **Mica** [$X_2Y_{4-6}Z_8O_{20}(OH, F)_4$], inorganic, *X* = K, Na, or Ca or less commonly Rb, or Cs; *Y* = Al, Mg, or Fe or less commonly Mn, Cr, Ti, Li; *Z* = Si or Al, may include Fe^{3+} or Ti PW20 – 77019
Lemon Yellow (LY)	**Benzimidazole** [$C_7H_6N_2$], organic, PY175 – 11784
Phthalo Blue (PB)	**Copper Phthalocyanine α** [$C_{32}H_{16}CuN_8$], inorganic, PB15:1 – 74160
Primary Blue Cyan (PBC)	**Copper Phthalocyanine β** [$C_{32}H_{16}CuN_8$], inorganic, PB15:3 – 74160
Permanent Blue Light (PBL)	**Titanium Dioxide** [TiO_2] inorganic PW6 – 77891, **Chlorinated Phthalocyanine [**$C_{32}H_3Cl_{13}CuN_8$ to $C_{32}HCl_{15}CuN$], organic, PG7 – 74260, **Copper Phthalocyanine β** [$C_{32}H_{16}CuN_8$], inorganic, PB15:3 – 74160
Phthalo Green (PG)	**Chlorinated Phthalocyanine [**$C_{32}H_3Cl_{13}CuN_8$ to $C_{32}HCl_{15}CuN$], organic, PG7 - 74260
Permanent Green Light (PGL)	**Arydile yellow** [azo coupling of aniline and acetoacetanilide], organic, PY97 – 11767, **Titanium Dioxide** [TiO_2], inorganic, PW6 – 77891, **Chlorinated Phthalocyanine [**$C_{32}H_3Cl_{13}CuN_8$ to $C_{32}HCl_{15}CuN$], organic, PG7 – 74260
Primary Red Magenta (PRM)	**Quinacridone** [$C_{20}H_{12}N_2O_2$], organic, PV19 – 73900
Titanium White (TW)	**Titanium Dioxide** [TiO_2], inorganic, PW6 – 77891
Ultramarine Blue (UB)	**Sodium Polysulphide-Aluminosilicate** [Na_3P, $xAl_2O_3.ySiO_2$], inorganic, PB29 – 77007
Van Dyke Brown (VDB)	**Iron Oxide,** inorganic, PBr7 – 77492, **Carbon black,** inorganic, PBk7 – 77266, **Quinacridone** [$C_{20}H_{12}N_2O_2$], organic, PV19 - 73900
Zinc White (ZW)	**Zinc Oxide** [ZnO], inorganic, PW4 – 77947

As an example of chemical-physical characterization by means of combined application of non-invasive optical techniques, analyses performed on six of the analysed acrylics – i.e. Copper-Phthalocyanine (Cu-Pc) paints (molecular structure reported in Fig. 2) - are reported in the following section. Three Cu-Pc paints are pure polymorphic form of Cu-Pc: Primary Blue Cyan (PBC, β form),

Phthalo Blue (PB, α form), and Phthalo Green (PG, chlorinated Pc); the remaining three, Cobalt Blue Hue (CBH), Permanent Blue Light (PBL), and Permanent Green Light (PGL), are mixtures of Cu-Pc and different organic compounds, like aniline and acetoacetanilide, and the inorganic compound titanium dioxide.

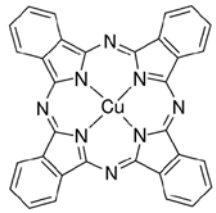

Fig. 2. Copper phthalocyanine molecule. A Cu^{2+} cation occupies the central cavity of the macrocycle forming covalent bonds with N.

Cu-Pc, referenced as PB15 and PG7 (class 74),[xiv] are blue and green pigments widely used by various artists between 1935 and 1990 (inter alia, Magritte, Picasso, Lichtenstein, Mondrian, Kandinsky and Pollock).[4,5] Pc-Cu paints have been also used in the context of conservation treatments in form of pictorial retouchings in historical paintings to replace original colours, which were found out to be toxic or unavailable.[5] Phthalocyanines owe their success to their remarkable properties, such as ease of use, low cost of manufacture, excellent lightfastness, heat stability up to 550 °C and good resistance to most solvents.[6] The partial solubility of Cu-Pc in aromatic solvents, though, may lead to colour changes (blue towards green) due to crystallization defects occurring during the transition from α- to β- polymorphic form with concurrent growth in crystals size.[6] Since aromatic compounds, especially toluene and xylene, can be used as solvent agents in restoring operations – i.e. the cleaning – the risk of deterioration of Cu-Pc pigments is significantly high, making crucial the identification of Cu-Pc paints before any restoration treatment.

3.2.2. Egg-tempera paints on wooden support

The samples were originally prepared for H2020 IPERION CH Project (WP6) with the aim of evaluating the efficiency of nonlinear microscopy techniques on a wide range of pictorial materials. Based on historical literature,[xiv] the samples were designed to simulate real paintings on wooden support. Using three different colours, red, yellow and blue, three sets of samples, labelled R, Y and B, respectively, were realized (Fig. 3). Each colour set presents three versions (A, B and C) characterized by different layers thickness, obtained by increasing the number of superimposed stratifications (thin layers for A, medium for B and thick for C). Each set is composed of 24 square samples (3×3 cm^2), for a total number of 72 samples. Up to now, the analysis has involved only version A (RA, YA and BA). Further experiments are planned for the thicker versions.

Each sample consists of a sequence of material layers, which are superimposed as follows (from bottom to top): wooden support (a "sandwich" structure made of fir and poplar), preparation layer (prepared with sifted gypsum, dispersed in a solution of rabbit skin glue and water), underdrawings (realised with lead and tin stylus, natural carbon, iron-gall ink), first pictorial layer (egg tempera with three different pigments R, B and Y), second pictorial layer to simulate pictorial retouchings (three different commercial oil-tempera[xv]), and finally a selection of materials used as protective layers (natural and synthetic varnishes by Zecchi© – Florence, white egg, and multi-layer coatings). The scheme of the stratification is shown in Fig. 3.

[xiv] Cennino Cennini, *Il libro dell'arte, o Trattato della pittura di Cennino Cennini da Colle di Valdelsa,* Felice Le Monnier Editore, Firenze, 1859.

[xv] Old Holland Classic Oil Colors by Kremer (Ruby lake – R set –, Quinacridon-Anthanthrone, colour index: PR209-PR168; Blue lake – B set –, Phthalocyanine, colour index: PB15; Indian yellow-orange lake extra – Y set –, Azo condensation-Diketo Pyrrolo Pyrrole, colour index: PY95-PR251).

Scheme of the internal stratification for RA, YA and BA:
A1: preparation + underdrawings
A2: preparation + underdrawings + egg-tempera
A3: preparation + underdrawings + egg-tempera + lake
A4: preparation + underdrawings + egg-tempera + varnish (dammar)
A5: preparation + underdrawings + egg-tempera + lake + varnish (dammar)
A6: preparation + underdrawings + egg-tempera + varnish (synthetic varnish)
A7: preparation + underdrawings + egg-tempera + protein layer (white egg)
A8: preparation + underdrawings + egg-tempera + multi-layer coating (white egg + dammar)

Fig. 3. Left: Minium, Cadmium yellow and Egyptian blue pigments during preparation of the egg-tempera; middle: set of 72 samples (middle), simulating egg-tempera painting on wooden support; right: bright-field images of the analysed samples RA2, YA2, BA2. Below, description of samples layers for R, Y and B sets (version A).

Wood was chosen as support for its historical and physical suitability for egg-tempera paintings. Besides, the presence of wood in the samples enables the application of SHG analysis for the visualization of wood microstructures – crystalline cellulose (SHG signal) and lignin (2PEF signal) in wood cell walls (see Ch. 2, *Wood*). The three pigments by Kremer© (Germany), selected due to their diffusion in historical artworks, as well as for specific optical properties, are the following: lead minium (red lead, Pb_3O_4) – cod. 42500; cadmium yellow medium (cadmium sulphide, CdS) – cod. 21051; Egyptian blue (blue copper silicate chemically classified as the mineral cuprorivaite, $CaCuSi_4O_{10}$) – cod.

10060. Pigments in form of powder were finely grinded and then mixed with the binder (beaten and filtered egg yolk).

Minium is an orange-red pigment, anciently obtained as oxidation product of lead minerals, extracted by smelting lead ore and, later, by heating lead white (basic lead carbonate) in air. Nowadays, it is obtained by heating at high temperature (about 480° C) of litharge or white lead. Minium can be dispersed in oil and egg binders, but is quite unstable and liable to discoloration in the presence of air pollutants, such as hydrogen sulphide. Moreover, it may darken when exposed to humidity and light. With respect to other binders, few colour changes are observed when the pigment is dispersed in oil medium. However, given the high level of toxicity of red lead, this pigment has been gradually removed from the market and replaced by others not toxic pigments presenting a similar hue.

Cadmium sulphide refers to a number of yellow–orange–red compounds sharing a common structure based on CdS. By substituting Cd or S with various elements including Zn, Hg, and Se, a variety of hues can be obtained. Such chromatic properties are due to CdS 2.42 eV band gap that can be modulated by the progressive substitution of Cd with one of the former elements (e.g. Zn to obtain pale yellow cadmium zinc sulphide pigments).[7] Cadmium yellow, cadmium red and cadmium orange are brilliant pigments with good permanence and tinting power, which have been widely used since 1840, especially by painters like Claude Monet, Vincent Van Gogh, Edvard Munch and Jackson Pollock. As a first step, cadmium yellow was prepared with an acid solution of cadmium salt (either chloride or sulphate), which was heated with hydrogen sulphide gas, until a powder with hues ranging from lemon yellow to deep orange was obtained. Although cadmium sulphide is not particularly toxic when used as pigment (median lethal dose LD50 > 5000 mg/kg), the intense exposure to cadmium vapours from welding may be harmful. Once cadmium’s toxicity

had been determined, the production of cadmium-based pigments has gradually decreased, with partial replacement by azo-pigments, which are both cheaper and non-toxic.

Egyptian blue is a copper silicate, chemically classified as the mineral cuprorivaite ($CaCuSi_4O_{10}$), rarely found in nature but synthetically obtained since ancient times, specifically since the 4th Egyptian Dynasty (around 2500 BC). Thanks to its chemical composition, Egyptian blue is stable in all media and does not undergo any colour change when applied to various organic media. Strong light does not influence its colour either, as it may be observed in samples that have survived for millennia in both dry and damp environments, still exhibiting an intense hue with no evidence of photo-bleaching. Recently, a further remarkable property of this pigment was characterized, namely the exceptionally high level of emission quantum efficiency in the near infrared (λ_{max} = 910 nm; ΦEM= 10.5 %) and the long excited lifetime (107 μs), which makes cuprorivaite an excellent candidate as luminescent label for a number of applications.[8]

As already mentioned, MPEF measurements were performed only RA, YA and BA sets. However, many difficulties were encountered in the analysis of paints thickness, due to the complexity of the samples. The results reported in the following sections concern only few samples of the entire set.

3.2.3. Acrylic and egg-tempera paints on glass, covered with varnish

An additional series of paints laid on glass cover-slips was prepared, specifically for verifying the efficiency of MPEF in detecting two different superposed materials – i.e. by measuring their respective thickness. To this purpose, four paint samples were covered with a protective varnish (Fig. 4). Some of the already described paints were used: one acrylic paint (Primary Red Magenta in sample 1), and the three egg tempera (Minium, sample 2, Cadmium

yellow, sample 3, and Egyptian blue, sample 4). All paints were covered on half of their surface with a layer of mastic varnish (see p. 55 for a description of the material), using an industrial tape (Kapton©) as thickness reference during the preparation. MPEF responses on mastic varnish were analysed separately.

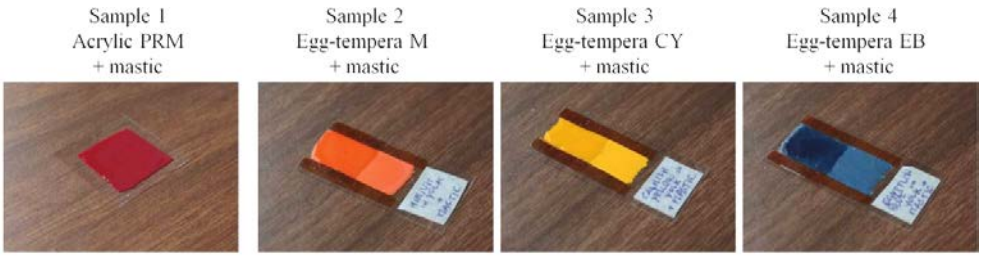

Fig. 4. Acrylic and egg-tempera paints on glass, covered with mastic varnish. (PRM: Primary Red Magenta, M: Minium, CY: Cadmium Yellow, EB: Egyptian Blue).

3.3. Non-invasive optical and chemical characterization of paints

Among the various spectroscopic techniques, Raman spectroscopy, Vis-NIR Fibre Optics Reflectance Spectroscopy (FORS), Laser Induced Fluorescence (LIF), and Scanning Multispectral Reflectography (SMR) in the Visible and Near Infrared spectral region are well-established and widely used for the study of the optical behaviour and chemical composition of paint materials. The description of the instruments used for the application of each technique is reported in Appendix 1.

Briefly, Raman spectroscopy[9] allows for the assignment of molecular composition according to the vibrational frequencies of chemical bonds present in both inorganic and organic compounds. Vis-NIR FORS is used to probe pigments and identify molecular functional groups, i.e. absorption bands due to overtones and combinations of fundamental vibrations.[10] When applied in combination with Raman spectroscopy, FORS facilitates the identification of chemical compounds, especially

when the detection of the Raman signal is hampered by the intense fluorescence emitted by binders and varnishes,[11] or when different pigments show similar Raman spectra (like in the case of several phthalocyanine paints analysed in this study). On the other hand, LIF[12,13] is based on the detection of the fluorescence emitted by molecules electronically excited with a coherent monochromatic laser source. Natural organic pigments and dyes, as well as synthetic organic and inorganic pigments, may fluoresce due to the presence of delocalized electrons in molecules containing multiple aromatic rings, long chains of conjugated double bonds or di-azo bonds.[14] Since LIF results are not always unambiguous, the support of other spectroscopic methods may be necessary for a full material analysis. An insight into the fluorescent properties of paints was provided by nonlinear Fluorescence Lifetime Imaging Microscopy (FLIM), which is a nonlinear modality which measures the time-decay of the fluorescence intensity exhibited by fluorescent emitters,[15] yielding information on the molecular microenvironment of a molecule and on its energy exchanges. Finally, Vis-NIR SMR[16,17] provides imaging of large areas of an object giving both spatial and spectral information, which can be used for a band to band comparison. This allows for the quantitative and qualitative identification of areas with different composition, related to natural degradation, past restoring intervention, preparatory sketches. Furthermore, having a significant number of bands, the technique yields spectral reflectance information for pigment identification.

In the following sections, results obtained on the acrylic paints through micro-Raman, FORS, LIF, SMR are reported firstly (§§ 3.4.1 – 3.4.4). Then, results acquired on the egg-tempera samples by means of FORS, SMR, and FLIM are presented (§§ 3.4.5, 3.4.6).

3.4. Results: optical and chemical characterization of paints

3.4.1. Micro-Raman Spectroscopy on acrylic paints

The chemical composition of the acrylic paints was determined through comparison with spectral information reported in literature and databases available online.[18-20] For brevity's sake, results are reported with a focus on six copper phthalocyanines (Cu-Pc) paints. The main Raman bands assigned for each Cu-Pc pigment, together with their respective intensities, are reported in Table 2, while the chemical compositions are summarized in Table 3.

Table 2. Main Raman bands of six analysed copper phthalocyanine paints.

Paint (acronym)	**Main Raman bands [cm^{-1}] and relative intensity*, λ_{exc} = 532 nm**
Primary Blue Cyan (PBC)	231w, 255w, 590m, 680m, 747w, 951w, 1037w, 1137w, 1341w, 1451m, 1527s, 1595w, 2672w, 2870w, 2976w, 3056w
Phthalo Blue (PB)	
Phthalo Green (PG)	142w, 162w, 505m, 685s, 818w, 978w, 1080m, 1200w, 1284m, 1340w, 1388m, 1503s, 1536s
Cobalt Blue Hue (CBH)	230m, 260m, 548s, 583m, 680m, 747w, 808w, 951w, 1096m, 1145w, 1450m, 1530s, 1584w, 1644w, 2192w
Permanent Blue Light (PBL)	143w, 231m, 255m, 450s, 590s, 609s, 680s, 747w, 831w, 951w, 1008w, 1037w, 1137m, 1341s, 1451s, 1527s, 1595w, 2870w, 3056w
Permanent Green Light (PGL)	153w, 309m, 505w, 615w, 685s, 818w, 978w, 998w, 1008w, 1080m, 1200m, 1284s, 1332w, 1340m, 1388s, 1455w, 1503s, 1536s, 1591w, 1668w

***** s: strong; m: medium; w: weak

As an example, Fig. 5 shows the Raman spectra acquired in the PB and PBL samples. Spectra of PBC and PB display numerous common bands (the most intense ones are centred at about 590, 680, 1451 and 1527 cm^{-1}), hampering the distinction between the two pigments. Concerning PG, the most significant bands appear at 685, 1503 and 1536 cm^{-1}. Raman analysis on these three pure phthalocyanine pigments (PB, PBC, PG) allowed the assignment of the bands in accordance with literature. The three mixtures (CBH, PBL and PGL) and the

PBC paints show bands ascribed to additional components. The bands at 1332, 1455, 1591 and 1668, cm^{-1} in the PGL spectrum correspond to the pigment Arylide Yellow, PY97.[21] Bands at 260, 548, 583, 808, 1096, 1644 and 2192 cm^{-1} in the CBH spectrum allow identifying the presence of Ultramarine, PB29. Bands at 143, 231, 450, 609 cm^{-1} in PBL, CBH, and PBC (traces) are due to Titanium White, PW6, in rutile form.

Table 3. Chemical composition of the six analysed copper phthalocyanine paints.

	PB15:1	**PB15:3**	**PG7**	**PB29**	**PY97**	**PW6**
	Cu-Pc α [$C_{32}H_{16}CuN_8$]	Cu-Pc β [$C_{32}H_{16}CuN_8$]	Chlorinated Pc [$C_{32}H_3Cl_{13}CuN_8$ to $C_{32}HCl_{15}CuN$]	Ultramarine Sodium Polysulphide-Aluminosilicate	Arylide yellow [azo coupling of aniline and acetoacetanilide]	Titanium Dioxide [TiO_2]
PBC		✓				(traces)
PB	✓					
PG			✓			
CBH		✓		✓		✓
PBL		✓	✓			✓
PGL			✓		✓	

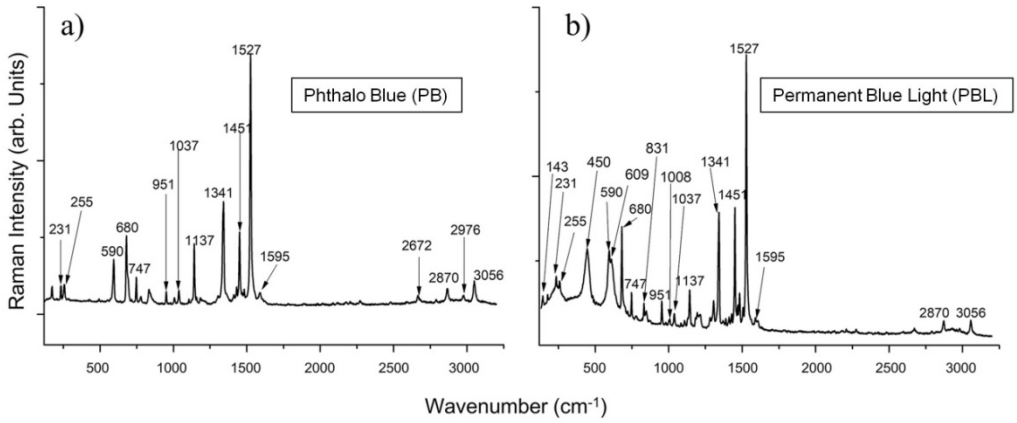

Fig. 5. Micro-Raman spectra of a) Phthalo Blue (PB) and b) Permanent Blue Light (PBL) acrylic paints upon excitation at 532 nm.

Based on micro-Raman results, some discrepancies with the composition declared by the manufacturer were found. The most significant one concerns PGL paint, in which bands of barium sulphate (at 998 cm^{-1}) and calcium sulphate (at 1008 cm^{-1}) where observed, being their presence possibly related to a component added as filler. Also in this case, bands assigned to the Cadmium Yellow pigment (at 153, 309, 615 cm^{-1}) were detected.[22] Furthermore, no traces of titanium dioxide were found in PGL, in contrast with what was reported by the manufacturer.

3.4.2. Fibre Optics Reflectance Spectroscopy (FORS) on acrylic paints

The reflectance spectra of the six acrylic paints are reported in Figure 6 a, b, c, highlighting selected spectral zones for better differentiation of the paint materials. Previous studies[23] have shown that Cu-Pc pigments present specific spectral features, which upon combined analysis with Raman spectroscopy allow discriminating between different compounds. It is observed that all the analysed paints have varying degrees of transparency at 800 nm, which is the wavelength of the femtosecond laser used for MPEF measurements, as well as in the spectral region between 335 and 610 nm, where the induced multi-photon emission can be detected. This variation is important in view of the NLOM measurements performed on the samples, as it provides a series of conditions to test the capacity of thickness determination by this technique. Figure 6b displays the second derivative of the reflectance function for Primary Blue Cyan, Phthalo Blue and Phthalo Green paints in the NIR region between 700 and 900 nm. A possible differentiation between the three paints is based on the identification of the inflection points, which are located at 800, 860 and 900 nm for PBC, PB and PG respectively. Figure 6c shows the spectra of all Cu-Pc paints in the 350-700 nm region. Further

confirmation of the chemical composition of these paints is based on the detection of a shoulder at 410 nm attributed to titanium dioxide in rutile form.[23]

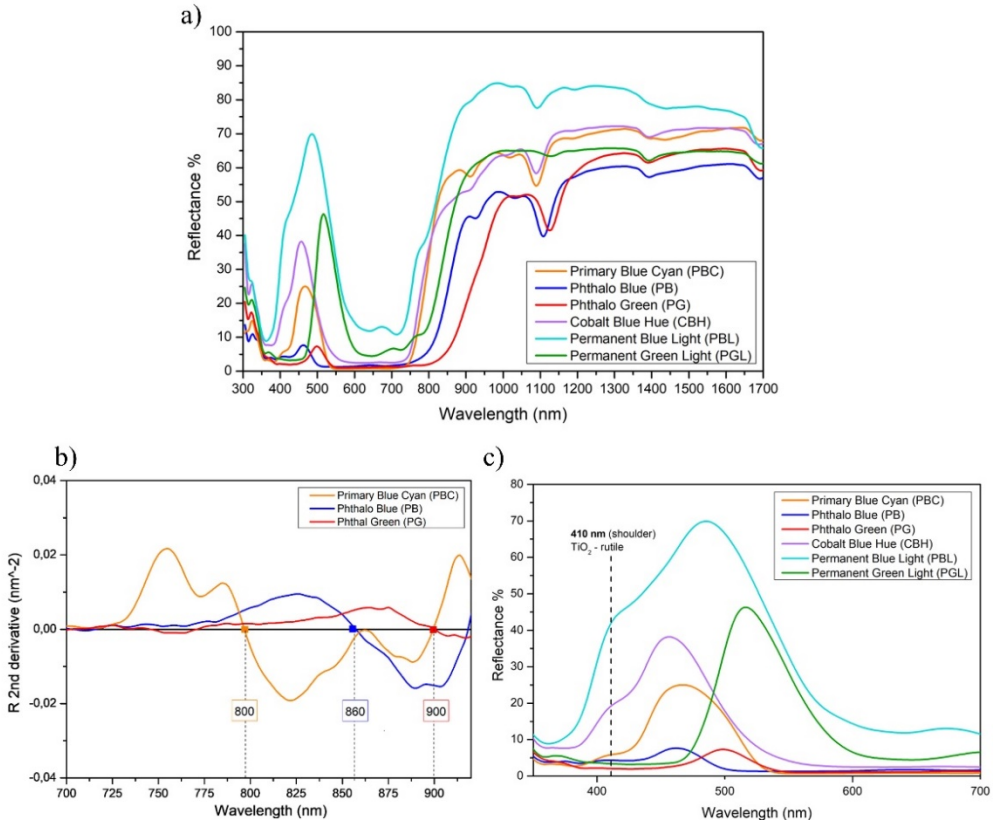

Fig. 6. Reflectance spectra of Cu-Pc paints: a) in the 300-1700 nm spectral range; b) second derivative curves for PBC, PB and PG in the 700-920 nm range, where the zeros of the functions correspond to the position of the inflection points; c) zoom in of the reflectance spectra of Cu-Pc paints in the 350-700 nm. The shoulder at 410 nm highlights the presence of TiO_2 only in PBC, CBH and PBL paints.

3.4.3. Laser Induced Fluorescence (LIF) on acrylic paints

LIF spectra of the six Cu-Pc paints are displayed in Figure 7. The common broad emission band between 280 and 380 nm is attributed to the acrylic binder and it is consistent with previous published studies.[11,24,25] The emission bands at higher wavelengths between 380

and 580 nm are characteristic of each pigment. Specifically, CBH and PBC show very similar fluorescence emissions, with maxima at 400 and 440 nm; PBL and PB display a broad, somewhat structured emission band centred at around 400 nm; PG emits a relatively less intense fluorescence band located between 380 and 550 nm, and PG emits a relatively less intense fluorescence band located between 380 and 550 nm. The emission of these five paints is associated with characteristic fluorescence emission bands of phthalocyanines.[26] PGL shows a band slightly shifted towards longer wavelengths (460-570 nm, centred at 500 nm) with respect to the other pigments, which is associated with azo-compounds emission. The identification of the LIF emission bands collected by excitation at 266 nm, as described above, is necessary to ensure the proper detection of the MPEF signals. Given the wavelength of the femtosecond laser source, it is expected that three-photon absorption at 800 nm would yield similar fluorescence spectra than those collected by one-photon absorption at 266 nm. The detection range of the nonlinear optical microscope is limited by the filter in front of the photomultiplier to the region of 335-610 nm. According to LIF measurements, this implies that MPEF signals include emission from the binder and pigment components of the paints.

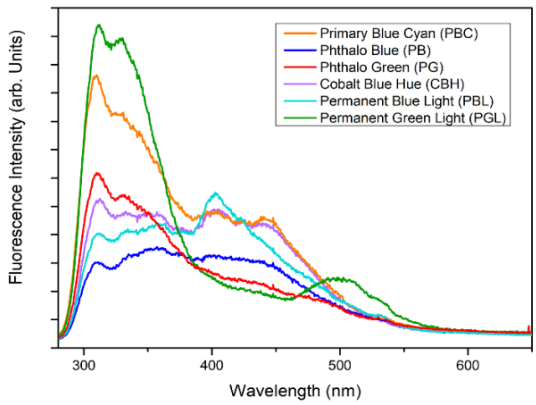

Fig 7. LIF spectra acquired by excitation at 266 nm of the Cu-Pc pigments.

3.4.4. Vis-NIR Scanning Multispectral Reflectography (Vis-NIR SMR) on acrylic paints

The transparency of the paint layers to the excitation wavelength used for MPEF analysis is an essential requirement for thickness measurements. To verify this, three different materials – i.e. iron-oxide earth charcoal, lead stylus and natural carbon – with known characteristics of absorption in the spectral ranges of interest, were used to draw a sequence of lines on a wooden base covered with a preparation layer (gypsum and glue). The acrylic samples were positioned on the prepared surface in order to cover all the three lines of underdrawing and the so-obtained system was scanned with multispectral reflectography. The images corresponding to NIR channels 18 (central λ = 850 nm, $\Delta\lambda$ = 100 nm) and 20 (λ = 1050 nm, $\Delta\lambda$ = 100 nm) were selected from the image-cube and are reported in Fig. 8, in comparison with the RGB image, computed from the visible set.

The results show that the underdrawing lines are visible, or partially visible, underneath most of the samples at both the wavelengths, except for Van Dyke Brown (VDB) and Iridescent Silver (IS), which result always opaque. Low transparency is also found in Indanthrene Blue (IB), Phthalo Green (PG), Permanent Blue Light (PBL) and Titanium White (TW) at 850 nm. The same paints show higher transparency at 1050 nm. In general, the visibility of the graphic lines (especially natural carbon, which is characterized by strong absorption in the NIR) indicates favourable condition for the penetration of the excitation wavelength used for MPEF analysis. Paints' transparency in the region of fluorescence emission is another important requirement for MPEF analysis, which will be discussed in the following section.

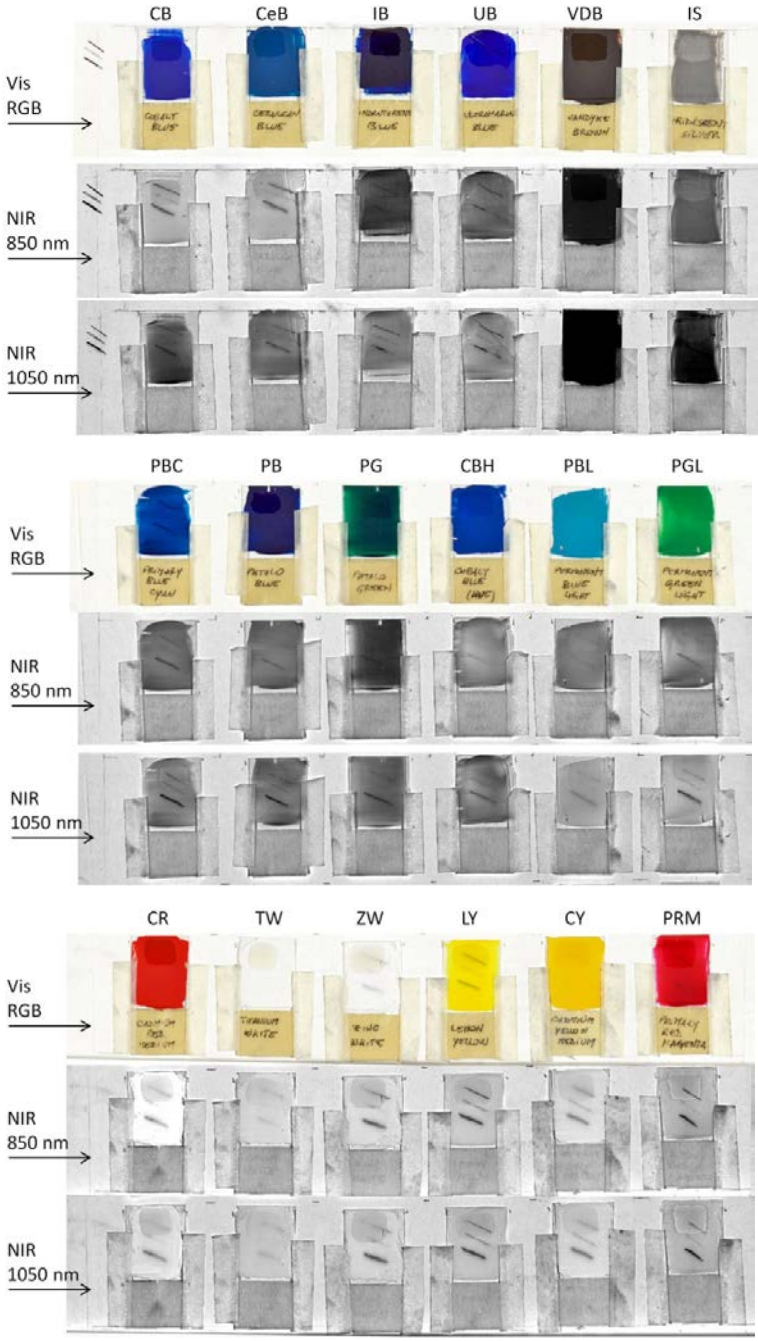

Fig. 8. Multispectral reflectance images at 850 nm and 1050 nm, in comparison with RGB images, showing the visibility of absorbing materials (parallel lines of iron-oxide earth charcoal, lead stylus and natural carbon, from up to down) underneath the painted samples.

3.4.5. Fibre Optics Reflectance Spectroscopy (FORS) and Vis-NIR Scanning Multispectral Reflectography (Vis-NIR SMR) on egg-tempera paints

Egg-tempera samples (RA, YA and BA sets) were analysed with FORS and the multispectral reflectography (Fig. 9 and 10). Results concerning samples R2, Y2, B2 (egg-tempera layers without any protective/overpaint) were especially useful to investigate the optical properties of the three pigments in view of the following MPEF analysis.

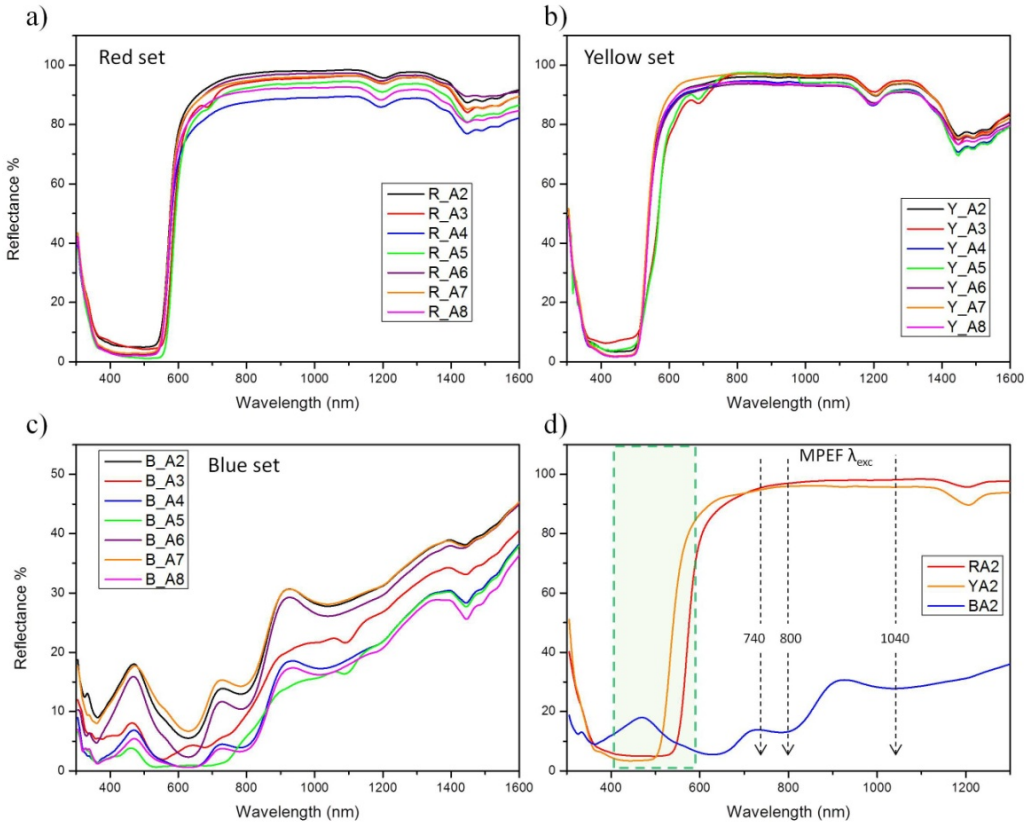

Fig. 9. Reflectance spectra of sample sets RA (a), YA (b) and BA (c). The excitation wavelengths (740, 800 and 1040 nm) and the detection spectral range used with MPEF setup (400-600 nm, dashed green rectangle) are highlighted on RA2, YA2 and BA2 reflectance spectra (d).

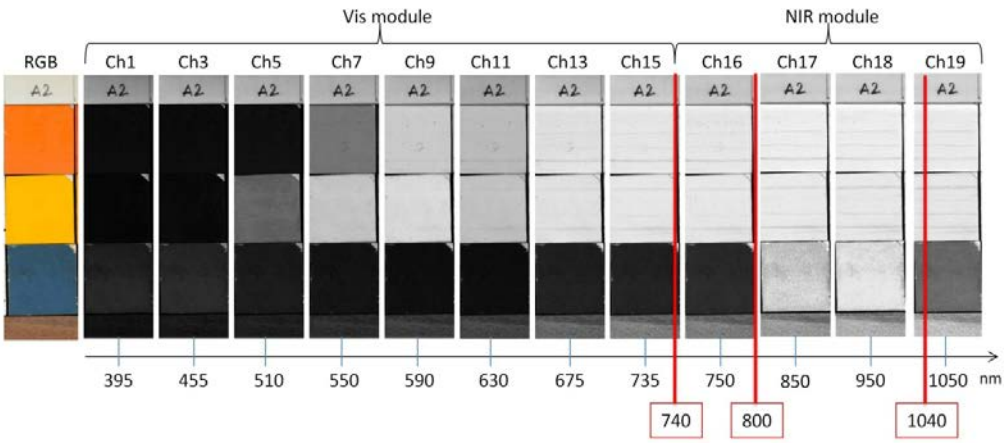

Fig. 10. Samples RA2, YA2, BA2 Multispectral Vis-NIR images (spectral range: 370-1050 nm). Each channel (Vis and NIR modules) corresponds to a specific spectral band (the central wavelength is reported). Images show the variable degrees of transparency of R, Y and B paints, especially in correspondence of the excitation wavelengths of MPEF (pointed out by the red lines).

Red lead (Pb_3O_4) is a semiconductor with an indirect band gap at about 2.1 eV,[27] and its reflectance spectrum (Fig. 9a) is characterized by a typical sigmoidal shape with an inflection point at 570 nm. A sigmoidal shape is also observed in the reflectance profile of the semiconductor Cadmium yellow (CdS),[7,28] with an inflection point at 530 nm (Fig. 9b). A second inflection point at 570 nm and a weak absorption band at 685 nm are visible in the spectra collected on samples YA3 and YA5, containing Indian yellow-orange lake extra (Azo condensation DPP – diketopyrrolo-pyrrole, PY95-PR251).

Reflectance profiles collected on the samples containing Egyptian blue ($CaCuSi_4O_{10}$), reported in Fig. 9c, show absorption bands in the Vis-NIR range (a shoulder at 540 nm and two bands centred at about 630 and 795 nm) attributable to three electronic transitions ($^2B_{1g} \rightarrow {}^2B_{2g}$, ^2E_g, $^2A_{1g}$) related to Cu^{2+} ions in a octahedral ligand field with a square-planar (D4h) symmetry (Fig. 11).[8,29] Such absorption features are partially masked in samples BA3 and BA5, due to the presence of the superimposed layer of blue lake, containing

phthalocyanine (PB15) pigment: reflectance profiles are indeed characterized by a structured absorption band in the Vis-NIR range distinctive of copper-phthalocyanines (see previous sections).

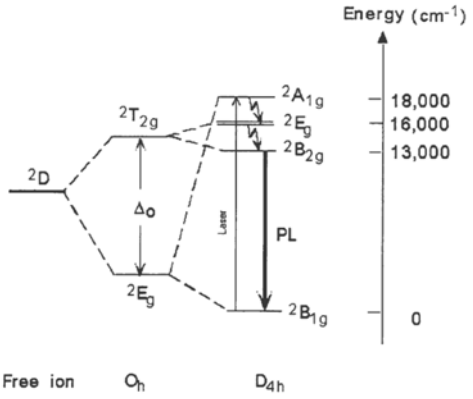

Fig 11. Energy-level scheme for Cu^{2+} in Egyptian blue pigment. (G. Pozza *et al.* 2000)

The fluorescence behaviour of the analysed pigments was briefly investigated in literature. Yolk binder exhibits fluorescence with a peak of emission centred at 500 nm,[30] whereas a low fluorescence quantum yield is expected for inhorganic pigments. Specifically, Minium is an indirect semiconductor, and thus is not considered a strong fluorescent emitter. As Minium dispersed in egg tempera shows an intense fluorescence,[31] the eventual nonlinear fluorescence signal detected with MPEF analysis will be mainly attributed to the organic binder. Concerning Cadmium yellow, Cd-pigments are generally characterized by radiative recombination with emission of fluorescence in the visible range, called Near Band Edge (NBE) emission, as well as emission in the near infrared range attributed to Deep Level Emissions (DLE).[32] Fluorescence emission by Cd yellow is then expected. Finally, Egyptian blue exhibits an intense fluorescence emission band centred at about 910 nm due to the lowest energy electronic transition ($^2B_{1g} \rightarrow {}^2B_{2g}$).[29] Considering the detection range used in MPEF analysis (400 and 600 nm), the main contribution to the eventual

nonlinear fluorescence of Egyptian Blue will be attributed to the egg binder, rather than the pigment. The varying degrees of transparency of the egg-tempera paints between 400 and 600 nm (Fig. 9d) should allow the detection of the emitted fluorescence (from the binder and/or the pigments). It is worth to notice, though, that all samples, especially the red and the yellow ones, show an absorption band in the spectral detection range of nonlinear microscopy. Hence, a possible auto-absorption of the nonlinear fluorescence will be taken into account. Within the spectral range of interest, Minium and Cd-yellow show similar behaviour: both exhibit an absorption band between 350 and 550 nm, with a following rapid increase of the reflectance values (probably due to the reflecting gypsum background), reaching the 90% at 650 nm for Minium and at 600 nm for Cd yellow, remaining between 100% and 80% up to 1700 nm. With reference to the Egyptian blue, the reflectance spectrum shows low reflectance at 740 nm (about 14%) and R = 40% at 1550 nm. This behaviour is observed also in the images obtained with the Multispectral Vis-Nir Scanner (INO-CNR), shown in Fig. 10.

3.4.6. Fluorescence Lifetime Imaging Microscopy (FLIM) on egg tempera paints

The optical properties of the three egg-tempera paints were firstly investigated through fluorescence lifetime microscopy, in order to verify the presence of the nonlinear fluorescence emission at the 740 nm excitation wavelength and to characterize its decay. Such information was taken into account for the further acquisition of the MPEF signal. Different trends in the decay curves were observed (Fig. 12) and the fluorescent lifetime of each paint was computed by deconvolution of the Instrument Response Function (IRF) from the measured fluorescence. This procedure is specifically recommended in case of lifetime close to the time response of the device. The evaluated average values of

fluorescence lifetime for Red lead (Minium), Cadmium yellow and Egyptian blue resulted 240 ps, 170 ps, and over 12 ns, respectively. Specifically, the red and the yellow pigments (Fig. 12a and b) are characterized by a significantly short fluorescence lifetime, which is comparable or smaller than the time window of the system (approx. 200 ps). By contrast, it was noticed that the blue pigment fluorescence lifetime was well above the interval between laser pulses (12 ns), thus showing a constant trend of the decay curve (Fig. 12c). On the basis of the analysed fluorescence lifetime, favourable condition for the detection of MPEF signal from the three pigments can be expected.

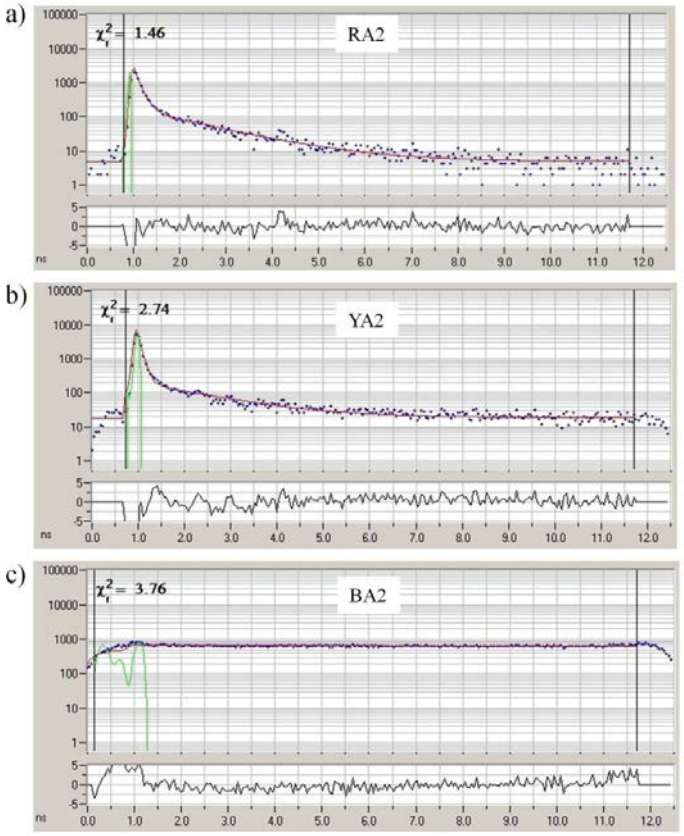

Fig 12. Fluorescence lifetime decay curves of samples RA2 (top), YA2 (middle) and BA2 (bottom). The time (ns) is reported on the x axis and the counts are reported on the y axis. Recorded data (dots), mono-exponential fit (red continuous line), Instrument Response Function, IRF (green continuous line).

3.5. Paint thickness analysis

In-depth imaging was performed with a Time-Domain confocal OCT prototype developed at CNR-INO, which combines confocal microscope optics with the OCT setup.[xvi] The system operates at a wavelength of 1550 nm with axial resolution of 10 μm in air and lateral resolution of 2.5 μm. An area of about 5×5 mm^2 was selected in the middle of the painted surface for thickness measurements. All the OCT profiles (25 mm on x axis and 1 mm on z axis) comprise the paint layer in the central part of the tomogram, as well as a portion of the glass support in the borders – i.e. the portion of cover-slip not covered by the paint. This allows for using the air/glass interface as reference for paint thickness measurements, without uncertainties concerning the knowledge of the refractive index, and overcoming limits of visualizations in case of low paint transparency to the radiation used.[xvii]

3.5.1. Multi-Photon Excitation Fluorescence (MPEF)

The three nonlinear optical microscopes, developed at CNR-INO, IQFR-CSIC and IESL-FORTH (detailed descriptions reported in App. 2), present different specifics, allowing for the determination of the best conditions for MPEF analysis. During the tests, the adequacy of the excitation wavelength was investigated for each paint and the laser power threshold was defined. Two different acquisition configuration (backwards and forwards) were tested for comparison of signal detection. However, the final results here reported were all obtained in backwards

[xvi] See App. 1 for more details.

[xvii] In such cases, values obtained with OCT were compared with an average of 3 measurements performed with a digital comparator (Mahr Extramess©, resolution up to 0.2 μm) in correspondence of the selected central area.

configuration, enabling the application of MPEF to non-transparent materials – i.e. opaque substrates (board, wood, canvas, etc.) – and, in general, to real cases.

3.5.2. Second Derivative Spline Distance (2DSD) method

One of the advantages of multi-photon microscopy is the intrinsic axial resolution, deriving from the nonlinear dependence of the process on the excitation light intensity. This entails that the efficient nonlinear interaction is confined to the focal volume of the laser beam, where the intensity is sufficiently high. Furthermore, the penetration depth is generally improved with respect to other linear microscopy techniques, thanks to the use of longer wavelengths. However, when performing thickness measurements with fluorescence microscopy, several optical factors must be taken into account for a proper interpretation of the results. First of all, as the focusing depth increases, the intensity of the generated signal tends to decrease, with a concurrent decrease of the optical resolution.[33] The loss of intensity and resolution is due to spherical aberration related to the broadening of the Point Spread Function (PSF), which becomes substantial especially at larger depths.[34] Furthermore, variations in the refractive index inside the analysed material induce changes in the optical path of the laser beam: if the refractive index of the sample (n_2) equals that of the of the immersion system (n_1), the focus will be located at the Nominal Focus Position (NFP); differently, in the case of $n_2 > n_1$ (e.g. a specimen placed in air), the focus will be shifted to the a different position, referred to as the Actual Focus Position (AFP).[35] As a consequence of the refractive index mismatch, the axial image will result compressed, and the shape of acquired z-profile will show some distortions, with a concurrent shift of the main maximum of intensity. Hence, in the presence of optically heterogeneous specimens (general condition of real cases),

it is not possible to estimate the thickness of a specimen by measuring the FWHM of the acquired z-intensity profile. Instead, a more complex analysis must be performed in order to determine an object's apparent thickness, which has to be subsequently corrected to obtain the real thickness. The Second Derivative Spline Distance (2DSD) method, described in the following paragraphs, was developed for this purpose. The effects of n-mismatch in confocal microscopy on PSF have been experimentally investigated by several authors,[36-39] but, to the best of our knowledge, only few of them proposed a concrete method for the correction. Kuypers *et al.* (2005)[40] presented a procedure to determine the correct axial thickness of an object (a layer of polymethyl methacrylate, up to 100 μm thick) having higher refractive index than the immersion medium, by using confocal fluorescence microscopy. In that study, the theoretical z-response intensity profiles with n-mismatch between polymer and water were calculated for different nominal focus positions of the incident light beam inside the material, and then compared with the theoretical z-response in case of no n-mismatch. The procedure was verified experimentally through scanning electron microscopy. It was shown that, by increasing the focusing depth, the maximum intensity of the z-response diminishes and shifts away from the interface, while the shape of the response curve is broadened (Fig. 13).

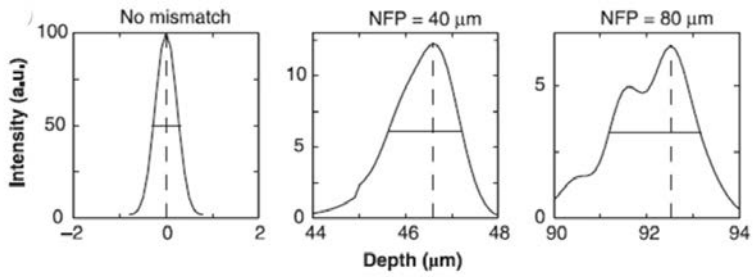

Fig. 13. Theoretical z-response for different Nominal Focus Positions (NFP) in case of water-polymer interface. The Actual Focal Position (AFP) is marked by the dashed line and FWHM is indicated by the horizontal solid line. (Kuypers *et al.* 2005).

According to this study, in case of no n-mismatch, the z-response profile would be symmetric and the thickness of the object would reasonably correspond to the FWHM of the curve.[41] In case of n-mismatch (air/polymer, air/paint, etc.), however, the response z-profile results asymmetric. Hence, it becomes crucial to define how the intensity profile can be related to the layer thickness. Specifically, Kuypers found that, in case of $n_2 > n_1$, the z-response is generally characterized by a sharp rising slope (first edge transition), a slight decrease across the material, and finally a steep slope (second edge transition). Moreover, the deeper the second surface of the specimen is positioned, the broader becomes the z-response and the smoother the transition, while the signal intensity decreases across the object with increasing depths. Such curve shape was observed also in the present study, in the MPEF profiles acquired on the paint layers, which showed more or less pronounced shoulders at the start and at the end of the decreasing central part (see §§ 3.6.2). Kuypers demonstrated that, when an imaging system with invariant PSF is used, the positions of the inflection points of the intensity profile correspond to the positions of the upper and lower surface of the analysed material, thus allowing the measurement of its thickness. Where the slope of the curve suddenly changes, the second derivative shows a local minimum (passing through zero), corresponding to the ascending or descending edge transitions (half-shoulder positions). In our case, the noisy of the MPEF signal produced by the painting layers made necessary the application of interpolation procedures on most of the acquired data plots for a clear identification of the inflection points. Data were processed in Matlab© environment with spline interpolation, providing a flexible way of estimating the underlying regression function, like in kernel regression and k-nearest-neighbours regression. Differently from polynomial interpolation, which uses a single polynomial to approximate the function over the entire defined interval, spline interpolation is achieved by dividing the

interval into multiple sub-intervals ($I_k = [x_k, x_k + 1]$, with $k = 1, \ldots, N - 1$), and choosing for each of them a polynomial degree d, which is usually small. The interpolation on each sub-interval, which uses a linear function (a grade 1 polynomial), can be considered a special case of spline interpolation. It is then imposed that two successive polynomials are smoothly sealed, i.e. observing the continuity of the first derivative $d - 1s$. The so-obtained curve is called spline function and results smoother than those obtained with other methods, easier to evaluate than the high degree polynomials, and not suffering from the Runge phenomenon.[xviii] Since in case of specific conformations of the data to be interpolated (e.g. steps), the interpolating spline may be subject to the Gibbs phenomenon (i.e. wide oscillations near a step), we applied the smoothing spline by defining specific weights w_i and smoothing parameter p, ranging between 0 and 1 (p = 0 and p = 1 producing a least-squares straight-line fit and a cubic spline interpolant, respectively). After the curves' interpolation, the distance between the first descendant and second ascendant inflection points of the second order derivative enabled to measure the apparent thickness (t') of each paint layer.

In the ideal case of axial rays (NA close to 0), with respect to the objective optical axis, the true thickness would be given by $t = nt'$, where n is the refractive index of the specimen. However, this formula is wrong for objective lens with high numerical aperture (NA close to 1), for which a more complex approach is needed. Based on White (1970),[42] we report the calculation for the definition of the correction formula for the general case of a specimen in air, which is geometrically depicted in Fig. 14.

[xviii] Phenomenon related to polynomial interpolation on evenly-spaced nodes with polynomials of high degree. It consists in increasing the amplitude of the error near the extremes of the interval.

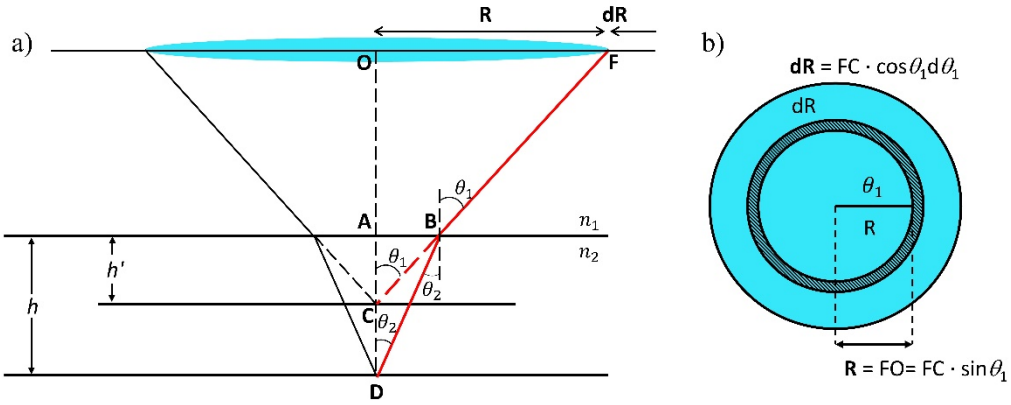

Fig. 14. (a) Vertical and (b) horizontal view of the typical ray path in the measurement of an object thickness with a microscope objective (light blue circles).

A ray of light, DB, coming from the bottom surface of the sample, will undergo a focal shift due to refraction at the top surface before reaching the objective, thus appearing to come from point C (ray CF, apparent thickness), instead of point D (real thickness). Being n_1 and n_2 the refractive indexes of the surrounding medium and sample respectively, with angles θ_1 and θ_2 (Fig. 14), then from the Snell's Law

$$n_1 \sin\theta_1 = n_2 \sin\theta_2 \tag{1}$$

If the true depth of the point D is DA = h and the apparent depth is CA = h', considering the triangles ABC and ABD from simple trigonometric formula, the cathetus AB is given by

$$AB = h' \tan\theta_1 = h \tan\theta_2 \tag{2}$$

The apparent depth (measured) is, then,

$$h' = h\frac{\tan\theta_2}{\tan\theta_1} = h\frac{\sin\theta_2}{\cos\theta_2}\frac{\cos\theta_1}{\sin\theta_1} = h\frac{sin\,\theta_2}{sin\,\theta_1}\frac{cos\,\theta_1}{cos\,\theta_2} \tag{3}$$

Considering that $\cos\theta_2 = \sqrt{1-\sin^2\theta_2}$ for the Pythagorean identity, that $\frac{\sin\theta_2}{\sin\theta_1} = \frac{n_1}{n_2}$ and $\sin\theta_2 = \frac{n_1}{n_2}\sin\theta_1$ from the Snell's Law, the apparent depth can be written as

$$h' = \frac{h\cos\theta_1}{\frac{n_2}{n_1}\sqrt{1-\frac{n_1^2}{n_2^2}\sin^2\theta_1}} = \frac{h\cos\theta_1}{\sqrt{\frac{n_2^2}{n_1^2}\left(1-\frac{n_1^2}{n_2^2}\sin^2\theta_1\right)}} = \frac{h\cos\theta_1}{\sqrt{\frac{n_2^2}{n_1^2}-\sin^2\theta_1}} \quad (4)$$

From Eq. 1 and 3, the true depth h is

$$h = h'\frac{\tan\theta_1}{\tan\theta_2} = h'\frac{\sin\theta_1}{\sin\theta_2}\frac{\cos\theta_2}{\cos\theta_1} = h'\frac{n_2}{n_1}\frac{\cos\theta_2}{\cos\theta_1}$$

For axial rays, $\theta_1, \theta_2 \to 0$ and $\cos\theta_1, \cos\theta_2 \to 1$, and the measured depth h approaches the limit value

$$h \to h'\frac{n_2}{n_1}$$

as the angles approach 0.

When the immersion medium is air ($n_1 = 1$), making the sample's refractive index $n_2 = n$, the approximated formula above mentioned is obtained:

$$h = h'n \quad (5)$$

Eq. 5 does not hold for the large values of θ_1 encountered with objectives of high NA.

Assuming that the full objective aperture is fully illuminated, the weighted mean apparent depth $\overline{h'}$ for all rays from $\theta_1 = 0$ to $\theta_1 = \theta_m$ where $NA = n_0\sin\theta_m$ is given by:

$$\bar{h'} = \frac{\int_0^{\theta_m} h' \cdot 2\pi FC \sin\theta_1 \cdot FC d\theta_1}{\int_0^{\theta_m} 2\pi FC \sin\theta_1 \cdot FC d\theta_1} \tag{6}$$

where *h'* under the integral sign is given by Eq. 4.

To a first approximation, Eq. 6 can be simplified to:

$$\bar{h'} = \frac{\int_0^{\theta_m} h' \cdot \sin\theta_1 d\theta_1}{\int_0^{\theta_m} \sin\theta_1 d\theta_1} \tag{7}$$

The denominator integral is:

$$\int_0^{\theta_m} \sin\theta_1 d\theta_1 = [-\cos\theta_1]_0^{\theta_m} = -\cos\theta_m + 1$$

The numerator integral, considering the expression for h' given by Eq. 4, is:

$$\int_0^{\theta_m} h' \cdot \sin\theta_1 d\theta_1 = \int_0^{\theta_m} \frac{h\cos\theta_1}{\sqrt{\frac{n_2^2}{n_1^2} - \sin^2\theta_1}} \cdot \sin\theta_1 d\theta_1 = -\int_0^{\theta_m} \frac{-h\cos\theta_1 \sin\theta_1}{\sqrt{\frac{n_2^2}{n_1^2} - \sin^2\theta_1}} \cdot d\theta_1 =$$

$$= -h\left[\sqrt{\frac{n_2^2}{n_1^2} - \sin^2\theta_1}\right]_0^{\theta_m} = -h\sqrt{\frac{n_2^2}{n_1^2} - \sin^2\theta_m} + h\sqrt{\frac{n_2^2}{n_1^2}} =$$

$$= h\left[\frac{n_2}{n_1} - \sqrt{\frac{n_2^2}{n_1^2} - \sin^2\theta_m}\right]$$

By gathering the numerator and denominator integrals, the weighted mean apparent depth, given by Eq. 7, becomes:

$$\bar{h'} = \frac{\int_0^{\theta_m} h' \cdot \sin\theta_1 d\theta_1}{\int_0^{\theta_m} \sin\theta_1 d\theta_1} = h\frac{\frac{n_2}{n_1} - \sqrt{\frac{n_2^2}{n_1^2} - \sin^2\theta_m}}{1 - \cos\theta_m} = h\frac{\frac{n_2}{n_1} - \sqrt{\frac{n_2^2}{n_1^2} - \sin^2\theta_m}}{1 - \sqrt{1 - \sin^2\theta_m}} \tag{8}$$

where the Pythagorean identity has been used again.

If the objective lens is immersed in air, then $n_1 = n_0 = 1$ and $n_2 = n$, then $\mathrm{NA} = \sin\theta_m$ and Eq. 8 simplifies as follows:

$$\bar{h}' = h\frac{n - \sqrt{n^2 - NA^2}}{1 - \sqrt{1 - NA^2}} \tag{9}$$

By reversing numerator and denominator, the true thickness is obtained as a function of the measured quantity h_{mes} corresponding to $\bar{h}'$

$$h = h_{mes}\frac{1 - \sqrt{1 - NA^2}}{n - \sqrt{n^2 - NA^2}}$$

and consequently the resultant correction factor F is:

$$F = \frac{1 - \sqrt{1 - NA^2}}{n - \sqrt{n^2 - NA^2}} \tag{10}$$

In this study, the correction of the apparent thickness measured with MPEF, by applying Eq.10, enabled to obtain the real thickness of each paint sample.

3.6. Results: thickness measurements on paint layers

Results acquired on acrylic samples on glass are reported firstly (§§ 3.6.1-2). Then, thickness measurements performed on egg-tempera samples are presented (§§ 3.6.3-4). Finally, results on multi-layered samples are shown.

3.6.1. Optical Coherence Tomography (OCT) on acrylic paints

Two OCT profiles were acquired along two perpendicular lines in the middle of each painted surface, in correspondence of the area chosen for MPEF measurements (Figure 18a, red lines and green square, respectively). The real

thicknesses of the paint layers were evaluated as an average of six values, taking into account the refractive index of the medium.

It is worth to mention that all the acquired OCT profiles enabled the visualization of the lower glass/air interface due to the transparency of the acrylic paints at the wavelength of the OCT source of 1550 nm. However, in some cases, no distinction between paint and glass was possible, probably due to the strong scattering from the paint, as shown in Figure 15b for Primary Blue Cyan sample. For that reason, the thickness of the paint layers was assessed taking as reference the glass surface visible at the border of each sample, assuming that 1 pixel corresponds to 1 μm along the in-depth direction and to 5 μm along the scanning direction of the tomographic image.

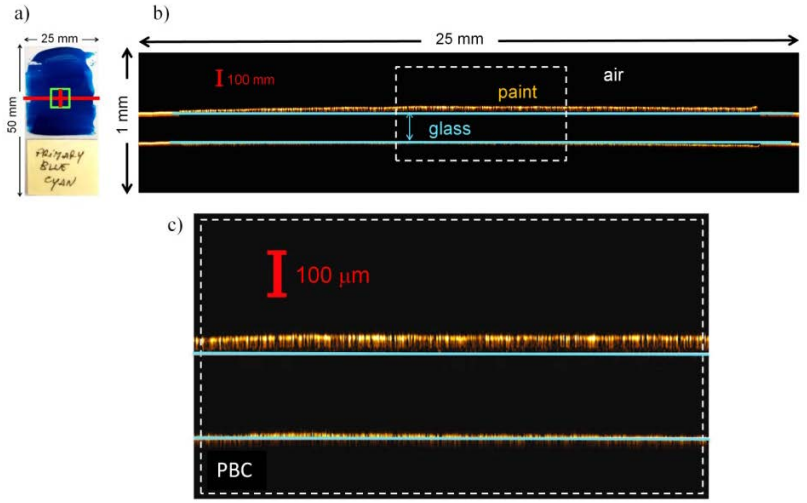

Fig. 15. a) Bright-field image of the Primary Blue Cyan sample showing the position of the two OCT profiles acquired on each sample orthogonally oriented and crossing at the centre of the painted surface: red lines (horizontal: 25 mm scanning length and 1 mm deep; vertical: 5 mm scanning length and 1 mm deep); b) OCT tomogram of PBC paint acquired along the horizontal red line (scale bar = 100 μm in-depth) displaying the paint layer (coloured in yellow) over the glass support (light-blue lines); c) zoom in of the central area, considered for paint thickness evaluation, highlighted by the dotted-line rectangle.

3.6.2. Multi-Photon Excitation Fluorescence (MPEF) on acrylic paints

To define the most adequate excitation wavelength, the laser was set at 800 nm and 1040 nm, depending on the setup used. The best signal quality and agreement with OCT were observed using the 800 nm excitation wavelength. Furthermore, both backward and forward configurations were tested, and z-profiles were acquired by moving the focus of the laser beam through the specimen from top to bottom (lower surface), and vice versa. Nevertheless, in view of application on real cases, final results were acquired in reflection mode, with up-to-down focus movement. MPEF signals were collected on a 5×5 mm^2 area, approximately located in the middle of each sample, in order to ensure a proper comparison with the OCT tomograms. For each measured area, the fluorescence intensity profile resulted from the average of 3 acquisitions. In addition, three measurements were performed in three adjacent points on the sample surface, and the average value was calculated for the thickness estimation. Based on previously analysed signal intensities, measurements were optimized in each case by setting the laser power to the most suitable range, although never exceeding 15 mW to avoid damaging the samples.

First measurements performed in Madrid revealed a nearly-symmetric trend of all the acquired z-profiles (PBC reported as an example in Fig. 16). The normalized MPEF curves were processed with Lorentzian fitting and the apparent thickness of the paint layer was measured as the full width at half maximum the interpolated curve. Then, the apparent depth was corrected according to the formula (10). Despite the overall relatively low Signal-to-Noise Ratio (SNR), these very first tests served to define the most suitable laser power below the threshold of damage of each paint, provided that a suitable SNR was obtained. Furthermore, it was observed that the magnitude of the signals varied with the degree of transparency of each paint to the laser excitation wavelength. As an example, the MPEF signals from the highly

absorbing PG and PB paints resulted around one order of magnitude lower than the signal measured in the rest of paints.

The second measurement campaign, performed in Florence, involved a higher number of acquisitions, thus providing a more representative dataset. The Signal-to-Noise Ratio resulted overall higher and MPEF z-profiles showed an asymmetric trend[40] that made it necessary the application of the 2DSD processing. It is worth underlying that, despite the different trends, z-profiles measured with the two setups gave the same thickness values, once corrected for the respective factor. The different shape of the MPEF curves is probably due to the acquisition system (collective lens numerical aperture and photomultiplier) of each setup. Deeper investigations on the dependence of the z-response on the instruments optics are envisaged in future studies. The results here reported concern the second measurement campaign, with the application of the 2DSD method.

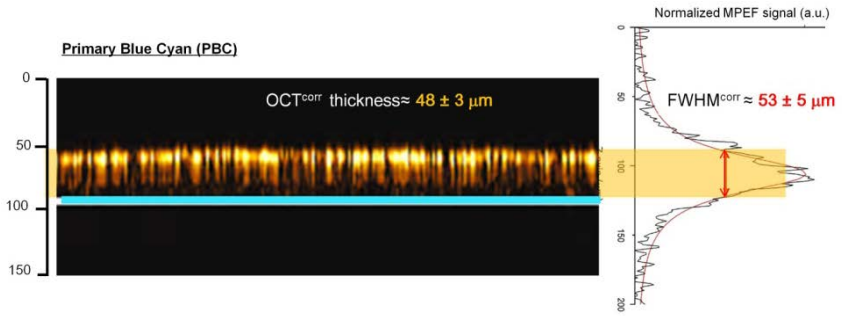

Fig. 16. MPEF z-profile of PBC acquired with the nonlinear microscope equipped with the NA = 0.42 objective (Madrid Lab.), showing a symmetric trend that allows for the Lorentzian fitting.

Basing on literature, for each excitation wavelength a plausible range of refractive indexes was used for the application of the correction formula. The corresponding variations of factor *F* are reported in the graph in Fig. 17, showing a nearly linear dependence of the two variables. Moreover, the

correction factor significantly increases when using high numerical aperture lens (NA > 0.8, Fig. 18), showing the exponential behaviour for refractive indexes 1.5 (blue line), 2 (red line) and 2.5 (green line).

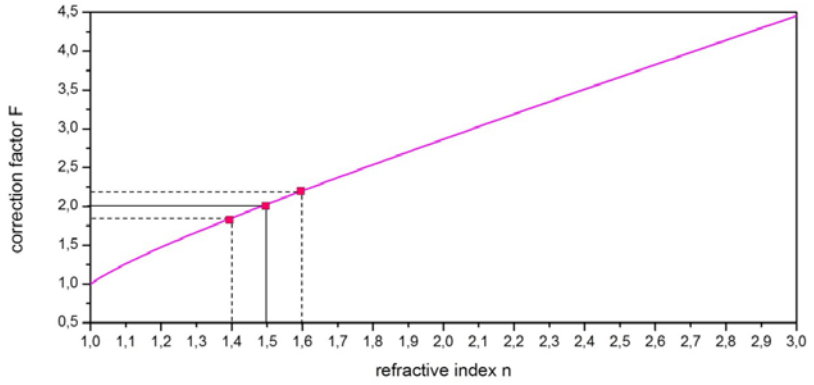

Fig. 17. Correction factor *F* as a function of the refractive index of the analysed material.

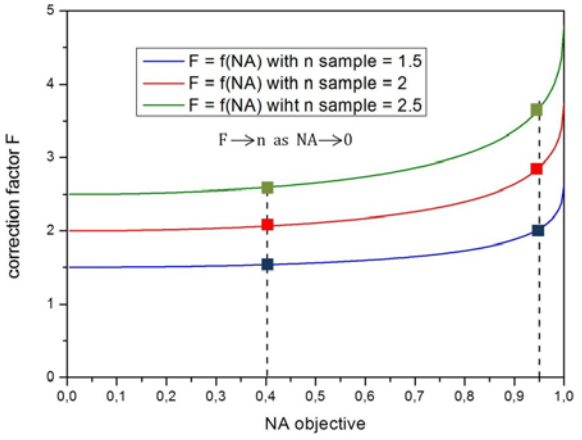

Fig. 18. Correction factor *F* as a function of the numerical aperture of the microscope's objective lens, at different refractive indexes of the analysed material (n = 1.5, blue line; n = 2, red line; n = 2.5, green line).

As expected from equation (10), for very low numerical apertures (NA ↛ 0) the correction factor tends to the refractive index of the material.

As an example of MPEF measurements with the application of 2DSD method, the results obtained on Primary Blue Cyan (Fig. 19) with the CNR-INO setup are reported in comparison with the OCT tomogram (Fig. 20).

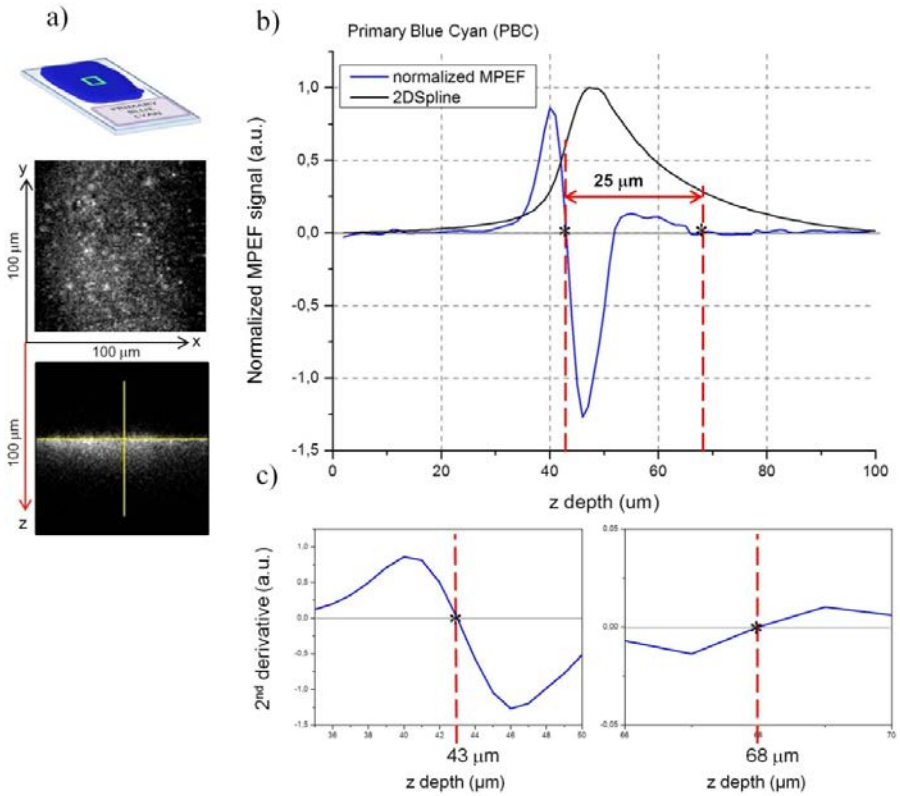

Fig. 19. a) From top: Primary Blue Cyan sample with the MPEF measurement area highlighted in green; grayscale MPEF intensity image (100×100 µm^2) at 50 µm depth from the top surface; image at depth z = 100 µm; b) profile of the MPEF signal intensity (in black) and second-order derivative (in blue) with inflection points (*) as a function of depth z. The latter defines the apparent thickness of the paint layer (highlighted by the red arrow and resulting equal to 25 µm); c) magnification of the ascending (left) and descending (right) edge transitions of the second-order derivative (inflection points at 43 and 68 µm depth), indicating the upper and lower paint surfaces, respectively.

Table 4 shows the thickness values obtained from the MPEF profile of PBC by applying the 2DSD method: the apparent thickness (distance between the

inflection points of the 2nd order derivative, 2DSD = 25 μm); the real thicknesses (2DSD correct) computed with correction factor *F* calculated for three refractive indexes 1.5, 1.6, 1.7; average thickness (average 2D2D correct = 55 μm with standard deviation = 4.3 μm). The latter result compared with the thickness value measured with OCT (48 mm, standard deviation = 3.2 μm).

Table 4. PBC thickness measured with MPEF in comparison with OCT.

PBC thickness							
2DSD [μm]						**OCT-conf** [μm]	
2DSD	2DSD correct	Average of 2DSD correct	sd dev	n @800 nm	correction factor F	thickness	sd dev
25.0	50.7	**55.0**	**4.3**	1.5	2.03	**48**	**3.2**
	55.0			1.6	2.20		
	59.2			1.7	2.37		

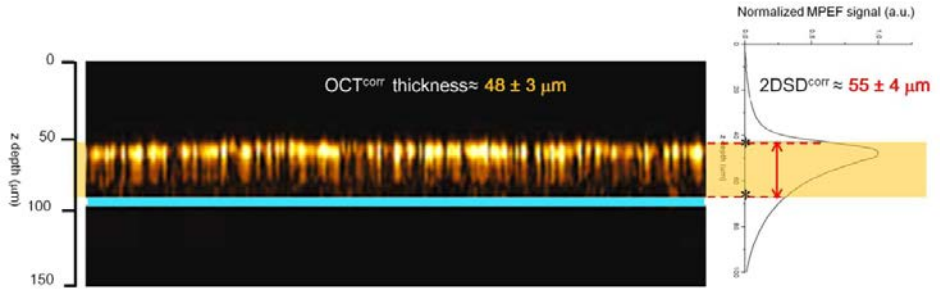

Fig. 20. OCT tomogram of PBC showing the paint thickness (48 ± 3 μm) in comparison with the MPEF z-profile, with the corrected 2DSD value highlighted by the red arrow (55 ± 4 μm).

The thickness of all the analysed acrylic paints are reported in Table 5 (p.117). The results shown are obtained at CNR-INO, but are in agreement with measurements performed at IQFR-CSIC. It is worth mentioning that, in the case of Phthalo Green, Iridescent Silver and Van Dyke Brown the thickness analysis was hindered by the weak intensity of the nonlinear signal. Specifically, it was observed that, when gradually raising the laser power, the fluorescence signal abruptly increased and immediately dropped to zero, causing a concurrent visible damage to the paint (diameter = 1-2 μm). By keeping the power of the

fs-laser at 15 mW, which defined the damage threshold for Phthalo Green, similarly to the other two paints, we were able to acquire a MPEF signal from which the layer thickness was computed as the FWHM of the fitted profile, provided proper correction was applied.

Concerning Zinc White paint (Fig. 21), both the z-profiles acquired with the 800 nm and 1040 nm excitation wavelengths showed good agreement with OCT results. This suggests that for this paint the nonlinear fluorescence emission may be generated by multi-photon absorption through the interaction of both 800 nm and 1040 nm radiation.

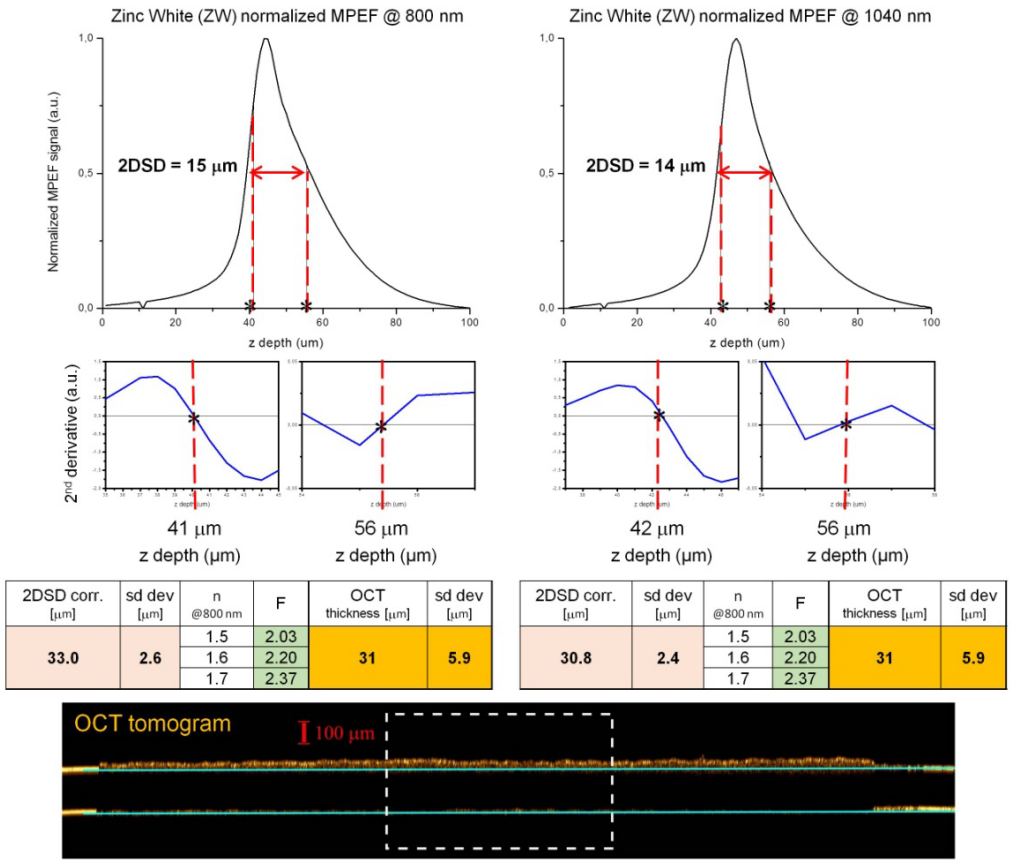

2DSD corr. [µm]	sd dev [µm]	n @800 nm	F	OCT thickness [µm]	sd dev [µm]
33.0	2.6	1.5	2.03	31	5.9
		1.6	2.20		
		1.7	2.37		

2DSD corr. [µm]	sd dev [µm]	n @800 nm	F	OCT thickness [µm]	sd dev [µm]
30.8	2.4	1.5	2.03	31	5.9
		1.6	2.20		
		1.7	2.37		

Fig. 21. MPEF profiles of Zinc White paint, acquired with the 800 nm (left) and 1040 nm (right) excitation wavelength; 2DSD values are compared with OCT results.

Differently, for most of the other paints, the results obtained with the two excitation wavelengths showed some inconsistencies. Specifically, it was observed that with 1040 nm excitation, in most cases the measured thicknesses resulted overestimated with respect to OCT measurements.

Table 5. Acrylic samples thickness measured with MPEF and OCT.

Acrylic paint layers thickness							
	2DSD (μm)					**OCT-conf (μm)**	
paint	2DSD	Mean 2DSD correct	sd. dev.	n @800nm	correction factor F	Mean thickness	sd. dev.
CBC	**19.0**	**45.0**	**3.2**	1.6	2.20	**49**	**4.3**
				1.7	2.37		
				1.8	2.54		
CBH	**14.0**	**30.8**	**2.4**	1.5	2.03	**28**	**2.8**
				1.6	2.20		
				1.7	2.37		
CeB	**14.0**	**28.4**	**2.4**	1.4	1.85	**31**	**2.1**
				1.5	2.03		
				1.6	2.20		
CR	**11.0**	**31.5**	**1.8**	1.9	2.70	**30.5**	**3.9**
				2.0	2.87		
				2.1	3.03		
CY	**17.0**	**45.9**	**2.8**	1.8	2.54	**43**	**1.8**
				1.9	2.70		
				2.0	2.87		
IB	**19.0**	**41.8**	**3.3**	1.5	2.03	**39**	**2.4**
				1.6	2.20		
				1.7	2.37		
LY	**21.0**	**46.2**	**3.6**	1.5	2.03	**47**	**3.7**
				1.6	2.20		
				1.7	2.37		
PBC	**25.0**	**55.0**	**4.3**	1.5	2.03	**48**	**3.2**
				1.6	2.20		
				1.7	2.37		
PBL	**20.0**	**44.0**	**3.4**	1.5	2.03	**38**	**2.8**
				1.6	2.20		
				1.7	2.37		
PG	**39.0** (FWHM)	**60.1** (FWHM^{corr})	**4.2**	1.4	1.43	**53**	**4.1**
				1.5	1.54		
				1.6	1.65		

PGL	**23.0**	**50.6**	**3.9**	1.5	2.03	**54**	**1.8**
				1.6	2.20		
				1.7	2.37		
PRM	**13.0**	**30.8**	**2.2**	1.6	2.20	**30**	**2.8**
				1.7	2.37		
				1.8	2.54		
TW	**20.0**	**73.3**	**3.2**	2.4	3.51	**70**	**5.3**
				2.5	3.67		
				2.6	3.83		
UB	**21.0**	**46.2**	**3.6**	1.5	2.03	**40**	**1.8**
				1.6	2.20		
				1.7	2.37		
ZW @800	**15.0**	**33.0**	**2.6**	1.5	2.03	**31**	**5.9**
				1.6	2.20		
				1.7	2.37		
ZW @1040	**14.0**	**30.8**	**2.4**	1.5	2.03	**31**	**5.9**
				1.6	2.20		
				1.7	2.37		

3.6.3. Cross-section analysis on egg tempera paints

In-depth OCT analysis did not allow for thickness measurement in egg tempera samples, due to the limited visibility under the painted surface possibly related to the intense scattering of pigments particles, both hampering the penetration of the incident radiation and weakening the generated interference signal. For this reason, micro-samples were taken from the edge of each sample in order to perform stratigraphic analysis[xix] by using a modular microscope from Carl Zeiss MicroImaging equipped with a Colibri LED light source system and an externally coupled metal halide (HXP) white light source. Throughout this study, an invasive technique has been applied only this time.

According to cross-sectional images (Fig 22 b), the thickness of the painted layers of samples RA2, YA2, BA2 (egg tempera without superficial varnish, Fig. 22 a) resulted 48 ± 3 μm, 53 ± 7 μm, and 98 ± 7 μm, for RA2, YA2 and BA2, respectively. Nonlinear measurements were firstly performed on these

[xix] Opificio delle Pietre Dure (OPD- Scientific Laboratory).

samples, in order to collect exclusively the nonlinear signal from the painting, avoiding any interference due to other fluorescence emitters (varnishes).

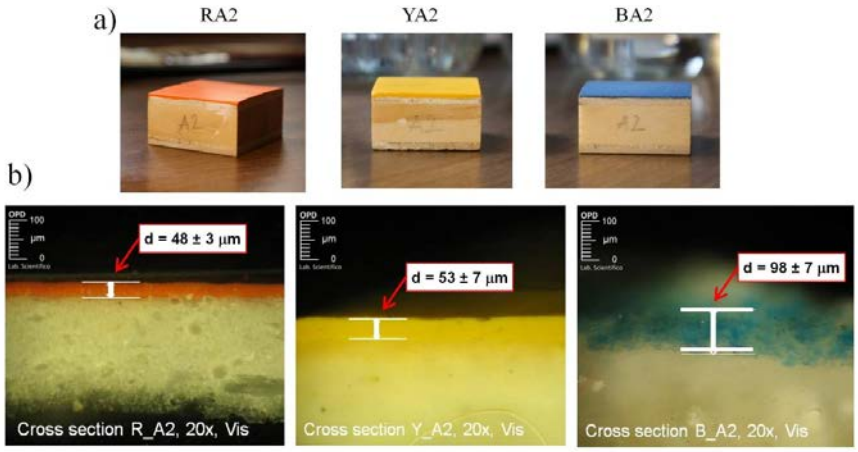

Fig. 22. a) Bright-field images of RA2, YA2, BA2 samples and b) respective cross sections (visible light, magnification 20x), showing the thickness of the painted layers.

3.6.4. Multi-Photon Excitation Fluorescence (MPEF) on egg-tempera paints

Thickness measurements performed in 2016 by using the old version of the nonlinear microscope at CNR-INO (740 nm laser excitation wavelength), resulted considerably underestimated for all the analysed paints. Specifically, the paint thickness in samples RA2, YA2 and BA2 resulted around 5 µm, 4 µm and 10 µm, respectively (Fig. 23 a). Even with increasing the beam power, no deeper detection was obtained. The lack of signal detection over 15 µm depth was attributed to the 740 nm excitation wavelength used. Presumably, the nonlinear absorption was generated inside the material at deeper depth than 15 µm, but the emitted fluorescence underwent attenuation before reaching the external surface. Concerning the discrimination of the protective layers on the other samples, no distinction between the protective materials and the paint layers was possible with MPEF imaging, probably due to both the detector sensitivity and the excitation wavelength used. In general, no significant results

were obtained, except for samples R7, Y7, B7, presenting a protective layer made of white egg laid over the paint layer. The intensity fluorescence images (Fig. 23 b) showed different micro-morphologies for the three pigments, which are possibly related to the pigment particle size and the drying process of pictorial layer in presence of the white-egg coating.

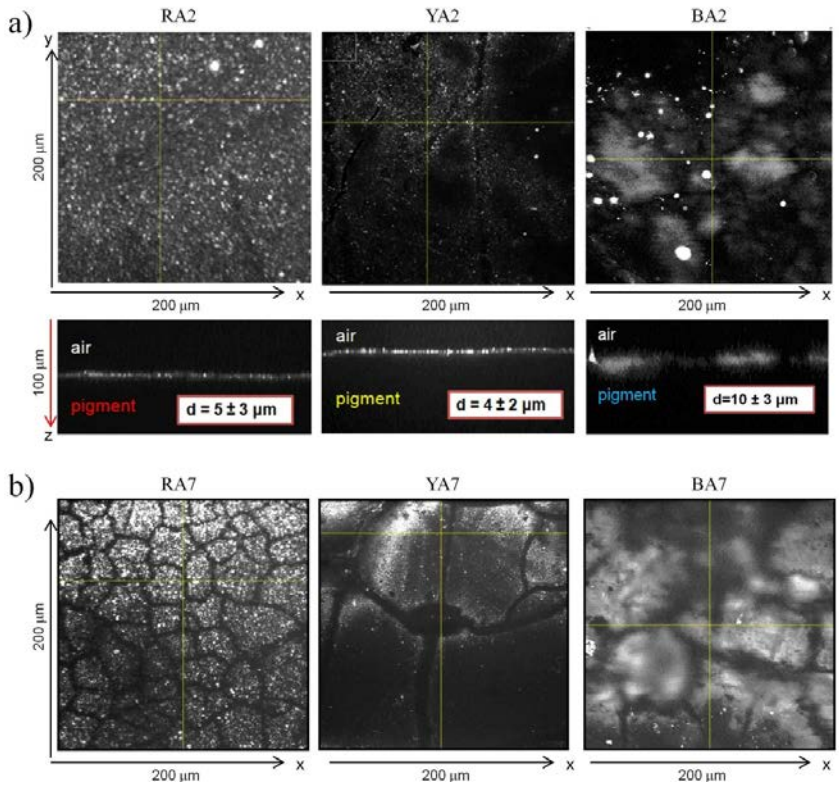

Fig. 23. a) MPEF intensity XY images of RA2, YA2, and BA2 egg-tempera samples with 740 nm excitation wavelength. The thickness of the paint layer (visible on the z-stacks) results significantly underestimated with respect to the stratigraphic analysis. b) MPEF images of samples RA7, YA7 and BA7, presenting a layer of white egg laid over the paint layer. The micro-morphology of the material is well visible on the three samples.

The thickness analysis was repeated in 2018 with the upgraded version of the nonlinear microscope at CNR-INO. Longer excitation wavelengths were used (800 nm and 1040 nm), and the 2DSD method was applied on the acquired

MPEF z-profiles. As a preparatory step, measurements were performed on the egg-tempera paints laid on glass, in order to verify the efficiency of MPEF signal on mono-layered systems. The analysis was then applied to the paint laid on wood, using the same excitation wavelengths. We observed that the 800 nm excitation was successful only for Minium, whereas the thickness of Cadmium yellow and Egyptian blue paints was measured by setting the laser at 1040 nm. The MPEF results acquired on Cadmium yellow (YA2) are reported as an example (Fig. 24).

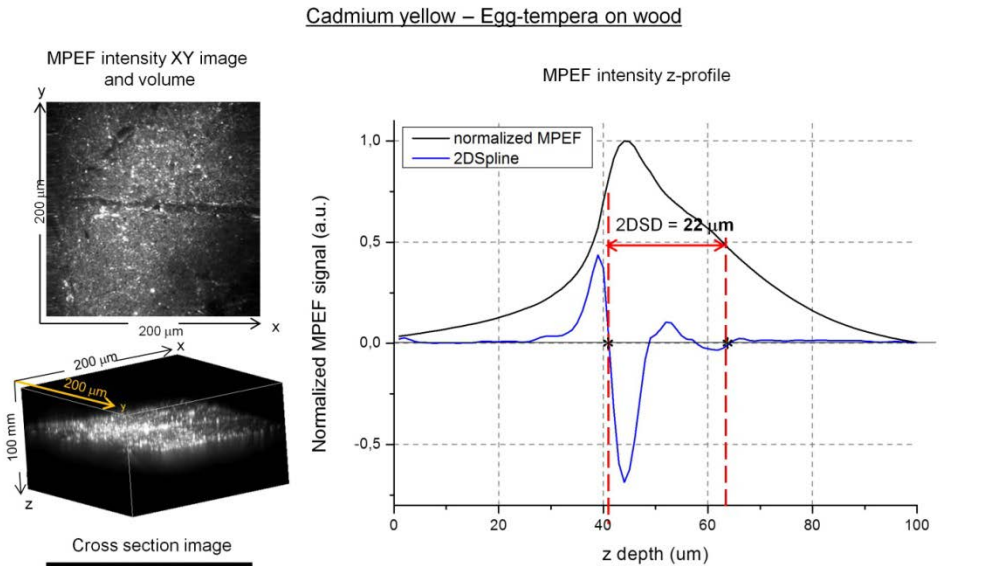

YA2 thickness @1040nm									
2DSD [µm]						OCT-conf		cross section [µm]	
2DSD	2DSD correct	Average of 2DSD correct	sd dev	n @800 nm	F	thickness	sd dev	thickness	sd dev
22.0	52.1	55.8	3.7	1.7	2.37	//	//	52.7	6.8
	55.8			1.8	2.54				
	59.4			1.9	2.70				

Fig. 24. MPEF intensity images (XY slice and volume view) acquired on cadmium yellow egg-tempera laid on wood and cross section analysis. Results are shown in the table.

With respect to the previous version of the setup, the use of longer wavelength (800 and 1040 nm instead of 740 nm) enabled the in-depth visualization of the

egg-tempera samples, due to both the higher penetration of the laser beam and low attenuation of the emitted fluorescence. The improved visualization can be related to the high numerical aperture of the objective lens (NA = 0.95 instead of 0.75), allowing for a confined excitation volume and, thus, higher axial resolution. In Table 6, MPEF, OCT and cross section results are reported showing very good correspondence between the measured thickness on each egg-tempera sample (on glass and wooden support).

Table 6. Thickness of egg-tempera samples measured with MPEF, in comparison with OCT and cross section analysis. The excitation wavelength at 800 nm was efficient for the measurement on red lead, whereas cadmium yellow and Egyptian blue required the use of 1040 nm wavelength.

	Thickness (t) measurements [µm]					
	Egg-tempera paints ON GLASS			**Egg-tempera** paints ON WOOD		
	MPEF^{corr}		**OCT^{corr}**	**MPEF^{corr}**		**Cross section**
	λ_{exc} = 800 nm	λ_{exc} = 1040 nm		λ_{exc} = 800 nm	λ_{exc} = 1040 nm	
Red Minium	**t = 40.3** sd = 2.9	✘	**t = 38** sd = 3.5	**t = 45** sd = 3.2	✘	**t = 48** sd = 2.6
Cadmium Yellow	✘	**t = 48.2** sd = 3.2	**t = 52** sd = 7.4	✘	**t = 55.8** sd = 3.7	**t = 52.7** sd = 6.8
Egypian Blue	✘	**t = 81.4** sd = 6.3	**t = 88** sd 10.7	✘	**t = 96.8** sd = 7.5	**t = 98** sd = 6.6

3.6.5. Paint thickness measurements: acrylic and egg-tempera paints on glass, covered with varnish

These final MPEF measurements were aimed at distinguishing the protective layer (varnish) from the underlying paint. As a preliminary step, the analysis was performed on a single layer of dammar and mastic resins laid over a glass cover-slip, in order to characterize the fluorescent emission. As expected, the nonlinear signal generated by varnish little conveyed the loss of intensity and resolution due to spherical aberration, which was observed in paint layers. This

improved detection is related to the homogeneity and transparency of the material, inducing limited scattering and auto-absorption effects on the transmitted signal. Moreover, the refractive index mismatch at the air/varnish interface, which is lower than at the air/paint interface, causes minor changes in the optical path of the incident laser beam, thus resulting in a more symmetric shape of the MPEF z-response. A representative example is given by mastic (Fig. 25) for which the 2DSD value (apparent thickness, t'= 85 μm) corresponds precisely to the FWHM value of the normalized intensity curve.

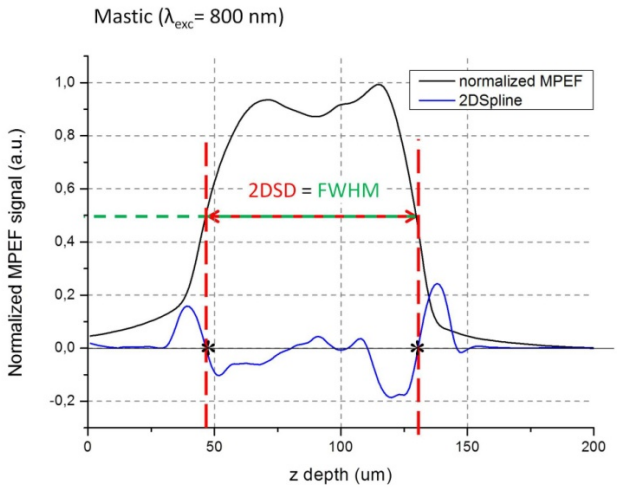

Fig. 25. MPEF z-profile of mastic resin laid on glass. The apparent thickness measured with the 2DSD method (85 μm) corresponds to the FWHM of the normalized intensity curve. The real thickness t = 172.55 μm, after the correction with F = 2.028, results in agreement with OCT measurements (t = 170 μm, st. dev. = 5.7 μm).

Subsequently, the analysis on the double-layered samples (paint and mastic varnish) were performed. In Fig. 26 and 27 the results obtained on Egyptian blue egg tempera and Primary Red Magenta acrylic paint[xx], both laid on the glass cover-slip and covered with a layer of mastic, are reported.

[xx] Measurement performed at IESL-FORTH.

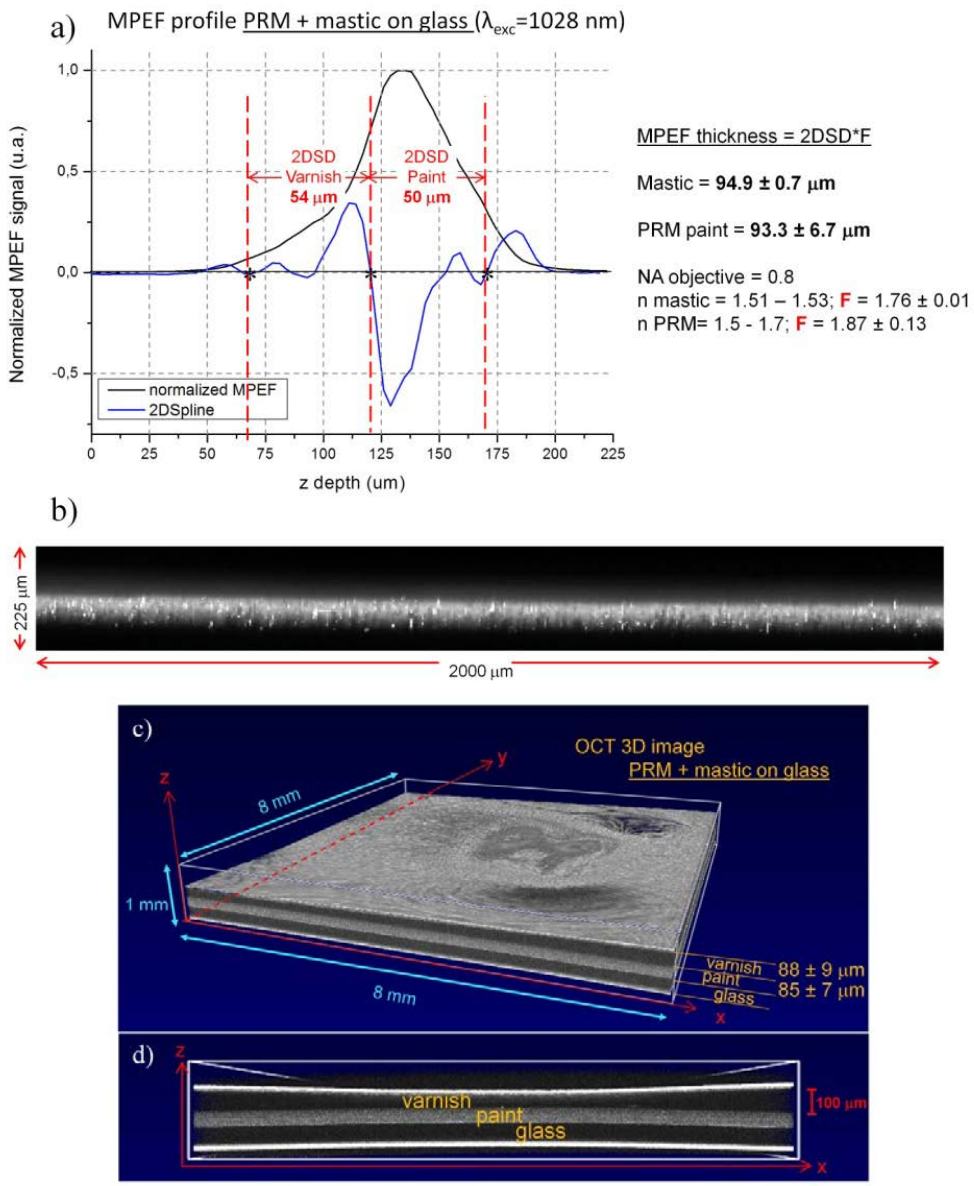

Fig. 26. MPEF analysis on Primary Red Magenta acrylic paint, laid on glass and covered with mastic resin: a) in-depth MPEF intensity profile with 2DSD values indicating the apparent thickness of the mastic layer (54 µm) and the paint layer (50 µm); real thicknesses, corrected for F, are reported on the right; b) scaled MPEF XZ image (x = 2000 µm; z = 225 µm) acquired with a z-step of 3 µm; (c) tomographic volume (8×8×1 mm^3) and (d) section acquired with Sd-OCT Thorlabs, showing the thickness of the analysed layers.

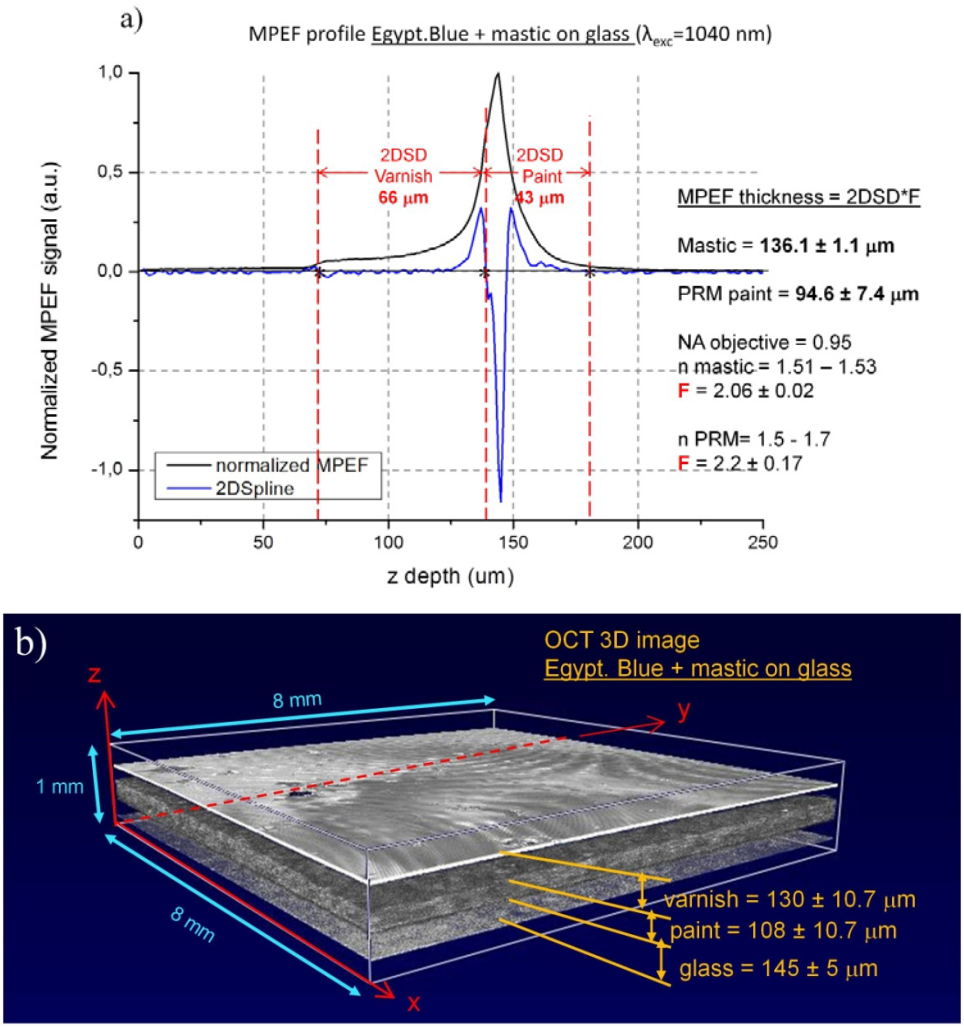

Fig. 27. MPEF analysis of Egyptian Blue egg tempera paint, laid on glass and covered with mastic resin: a) in-depth MPEF intensity profile with 2DSD values indicating the apparent thickness of the mastic layer (66 µm) and the paint layer (43 µm); b) real thicknesses, corrected for F and reported on the right, show good agreement with values measured with OCT.

The distinction between the different materials was feasible through the application of the 2SDS method, enabling the detection of the interfaces through the identification of the inflection points of the 2nd order derivative of the acquired MPEF profiles. The distance between the inflection points

corresponds to the apparent thickness, which in some cases cannot be measured with OCT, due to the optical properties of opaque materials. These results show that, despite the severe drop of the signal intensity with the increasing depth and the different transmission properties of the superimposed materials (varnish and paint), it is possible to perform the stratigraphy of paintings by means of MPEF analysis, based on proper interpretation of the nonlinear fluorescence responses.

References

[1] CIE (1974a). CIE44: 1979, Absolute methods for reflection measurements.

[2] R. G. Kuehni, Color: An Introduction to Practice and Principles, Wiley, New York, USA (1997).

[3] G. Kuehni, Color Space and Its Division, Wiley, New York, USA (2003).

[4] N. Khandekar, C. Mancusi-Ungaro, H. Cooper, C. Rosenberger, K. Eremin, K. Smith, J. Stenger and D. Kirby, A technical analysis of three paintings attributed to Jackson Pollock, Stud. Conserv., 55, 204–215 (2010).

[5] C. Defeyt and D. Struvay, PB15 as 20th and 21st artists' pigments: conservation concerns, e-Preservation Science (e-PS) 11, 6-14, ISSN: 1581-9280, web edition (2014).

[6] F. H. Moser and A. L. Thomas, Phthalocyanine Compounds, J. Chem. Edu., 41 (5), 245-249 (1964).

[7] F. Rosi, C. Grazia, F. Gabrieli, A. Romani, M. Paolantoni, R. Vivani, B. G. Brunetti, P. Colomban, C. Miliani, UV-Vis-NIR and micro Raman spectroscopies for the non destructive identification of Cd1−xZnxS solid solutions in cadmium yellow pigments, Microchem. J., 124, 856–867 (2015).

[8] G. Accorsi, A. Verri, M. Bolognesi, N. Armaroli, C. Clementi, C. Miliani, and A. Romani, The exceptional near-infrared luminescence properties of cuprorivaite (Egyptian blue), Chem. Commun., 1-3, 1 (2009) doi:10.1039/b902563d.

[9] H. Edwards, J. M. Chalmers, Raman spectroscopy in archaeology and art history, RSC Analytical Spectroscopy Series, The Royal Society of Chemistry, ISBM, 978-0-85404-522-8, London (2005).

[10] E. Cloutis, L. Norman, M. Cuddy and P. Mann, Spectral Reflectance (350–2500 nm) Properties of Historic Artists' Pigments. II. Red–Orange–Yellow Chromates, Jarosites, Organics, Lead(–Tin) Oxides, Sulphides, Nitrites and Antimonates, J. Near Infrared Spectrosc., 24, 119-140 (2016) https://doi.org/10.1255/jnirs.1207.

[11] M. Marinelli, A. Pasqualucci, M. Romani, G. Verona-Rinati, Time resolved laser induced fluorescence for characterization of binders in contemporary artworks, J. Cult. Herit., 23, 98-105 (2017) doi.org/10.1016/j.culher.2016.09.005.

[12] E. R. de la Rie, Fluorescence of paint and varnish layers (Part I, II, III). Stud. Conserv., 27, 1-7; 65-69; 102-108 (1982).

[13] D. Anglos, M. Solomidou, I. Zergioti, V. Zafiropulos, T. Papazoglou, C. Fotakis, Laser-Induced Fluorescence in Artwork Diagnostics: An Application in Pigment Analysis, Appl. Spectrosc., 50, 1331-1334 (1996).

[14] A. Nevin, G. Spoto, D. Anglos, Laser spectroscopies for elemental and molecular analysis in art and archaeology, Appl. Phys. A, 106, 339–361 (2012) doi:10.1007/s00339-011-6699-z.

[15] R. Mercatelli, F. Ratto, F. Rossi, F. Tatini, L. Menabuoni, A. Malandrini, R. Nicoletti, R. Pini, F. S. Pavone, R. Cicchi, Three-dimensional mapping of the orientation of collagen corneal lamellae in healthy and keratoconic human corneas using SHG microscopy, J. Biophotonics, 10, 75–83 (2017) doi:10.1002/jbio.201600122.

[16] H. Liang, Advances in multispectral and hyperspectral imaging for archaeology and art conservation, Appl. Phys. A, 106, 309-32 (2012) doi:10.1007/s00339-011-6689-1.

[17] C. Bonifazzi, P. Carcagnı`, R. Fontana, M. Greco, M. Mastroianni, M. Materazzi, E. Pampaloni, L. Pezzati, D. Bencini, A scanning device for VIS-NIR multispectral imaging of paintings. J. Opt. A Pure Appl. Opt. 10, 064011 (2008).

[18] L. Burgio, R. Clark, Library of FT-Raman spectra of pigments, minerals, pigment media and varnishes, and supplement to existing library of Raman spectra of pigments with visible excitation, Spectrochim. Acta Part A, 57, 1491-1521 (2001).

[19] M. C. Caggiani, A. Cosentino, A. Mangone, Pigments Checker version 3.0, a handy set for conservation scientists: A free online Raman spectra database, Microchem. J., 129, 123-132 (2016) doi: 10.1016/j.microc.2016.06.020.

[20] N. Marchettini, A. Atrei, F. Benetti, N. Proietti, V. Di Tullio, M. Mascalchi, I. Osticioli, S. Siano, I. Turbanti Memmi, Non-destructive characterisation of fourteenth century painting by

means of molecular spectroscopy and unilateral NMR, Surf. Eng., 29:2, 153-158 (2013) doi: 10.1179/1743294412Y.0000000065.

[21] C. S. Nadim, S. Zumbuehl, F. Delavy, A. Fritsch, R. Kuehnen, Spectrochim. Acta A, Synthetic organic pigments of the 20th and 21st century relevant to artist's paints: Raman spectra reference collection, 73, 505-524 (2009) doi.org/10.1016/j.saa.2008.11.029.

[22] B. W. Singer, D. J. Gardiner and J. P. Derow, Analysis of white and blue pigments from watercolors by Raman microscopy, Paper Conservator: Journal of the Institute of Paper Conservation, 17:13–19 (1993) https://doi.org/10.1080/03094227.1993.9638401, published online 2010.

[23] G. Poldi and S. Caglio, Phthalocyanine identification in paintings by reflectance spectroscopy. A laboratory and in situ study, Opt. Spectrosc., 114, 929–935 (2013).

[24] V. Spizzichino, F. Angelini, L. Caneve, F. Colao, R. Corrias, L. Ruggiero, In situ study of modern synthetic materials and pigments in contemporary paintings by laser-induced fluorescence scanning, Stud. Conserv. 60, S178–S184 (2015).

[25] R. Fantoni, L. Caneve, F. Colao, L. Fiorani, A. Palucci, R. Dell'Erba, V. Fassina, Laser-induced fluorescence study of medieval frescoes by Giusto de' Menabuoi J. Cult. Herit., 14S, S59–S65 (2013) https://doi.org/10.1016/j.culher.2012.10.025.

[26] M. Romani, F. Colao, R. Fantoni, M. Guiso, M. L Santarelli, Hyperspectral Fluorescence for Organic Pigment Characterization in Contemporary Artwork, J. Appl. Las. Spectrosc., 1, 29–36 (2014).

[27] Y. Zhou, J. Long, Q. Gu, H. Lin, H. Lin, and X. Wang, Photoinduced reactions between Pb3O4 and organic dyes in aqueous solution under visible light, Inorg. Chem., 51 12594-12596 (2012).

[28] C. Grazia, F. Rosi, F. Gabrieli, A. Romani, M. Paolantoni, R. Vivani, B. G. Brunetti, P. Colomban, C. Miliani, UV–Vis-NIR and microRaman spectroscopies for investigating the composition of ternary CdS1−xSex solid solutions employed as artists' pigments, Microchem. J. 125, 279-289 (2016).

[29] G. Pozza, D. Ajò, G. Chiari, F. De Zuane, M. Favaro, Photoluminescence of the inorganic pigments Egyptian blue, Han blue and Han purple, J. Cult. Heritage, 1, 393-398 (2000).

[30] A. Pelagotti, L. Pezzati, N. Bevilacqua, V. Vascotto, V. Reillon, C. Daffara, A study of UV fluorescence emission of painting materials, in Proceedings of Art'05 — 8th International Conference on Non Destructive Investigations and Microanalysis for the Diagnostics and

Conservation of the Cultural and Environmental Heritage, 15-19 May, Lecce, Italy, ed. C. Parisi, G. Buzzanca and A. Paradisi, Rome (2005) electronic resource.

[31] A. Cosentino, Effects of different binders on technical photography and infrared reflectography of 54 historical pigments, IJCS, 6, 3, 287-298 (2015).

[32] M. Thoury, J. K. Delaney, E. R. Rie, M. Palmer, K. Morales, J. Krueger, Near-infrared luminescence of cadmium pigments: In situ identification and mapping in paintings, Appl. Spectrosc. 65 939-951 (2011) doi:10.1366/11-06230.

[33] S. W. Hell, E. H. K. Stelzer, Lens aberrations in confocal fluorescence microscopy. Handbook of Biological Confocal Microscopy, Plenum Press, New York, 347-354 (1995).

[34] C. J. de Grauw, J. M. Vroom, H. T. M van der Voort, H. C. Gerritsen, Imaging properties in two-photon excitation microscopy and effects of refractive-index mismatch in thick specimens, App. Optics, 38, 28, 5995-6003 (1999).

[35] H. Jacobsen, S. W. Hell, Effect of the specimen refractive index on the imaging of a confocal fluorescence microscope employing high aperture oil immersion lenses, Bioimaging, 3, 39-47 (1995).

[36] S. Hell, G. Reiner, C. Cremer, E. H. K. Stelzer, Aberrations in confocal fluorescence microscopy induced by mismatches in refractive index, J. Microsc., 169, 391–405 (1993).

[37] S. H. Wiersma, T. D. Visser, Defocusing of a converging electromagnetic wave by a plane dielectric interface, J. Opt. Soc. Am. A, 13, 320–325 (1996).

[38] V. Dhayalan, T. Standnes, J. J. Stamnes, H. Heier, Scalar and electromagnetic diffraction point-spread functions for high-NA microlenses, Pure Appl. Opt. 6, 603–615 (1997).

[39] A. Diaspro, F. Federici, M. Robello, Influence of refractive-index mismatch in high-resolution three-dimensional confocal microscopy. Appl. Opt. 41, 685–690 (2002).

[40] L. C. Kuypers, W. F. Decraemer, J. J. J. Dirckx, J.-P. Timmermans, A procedure to determine the correct thickness of an object with confocal microscopy in case of refractive index mismatch, J. Microsc., 218, 1, 68–78 (2005).

[41] H. Brismar, A. Patwardhan, G. Jaremko, J. Nyengaard, Thickness estimation of fluorescent sections using a CLSM., J. Microsc., 184, 106–116 (1996).

[42] G.W. White, Improving the accuracy of vertical measurements under the microscope, Microscope, 18, 51–9 (1970).

PART 3. PhotoAcoustic analysis and results

1. Introduction

The terms PhotoAcoustics (PA) and OptoAcoustics (OA) usually refer to the generation of acoustic waves by modulated optical radiation. The first description of the photoacoustic effect as a physical phenomenon dates back to 1880,[1] with the discovery that audible sound is produced when chopped sunlight is incident on optically absorbing materials.[2] Since then, it took almost a century for the introduction of photoacoustic microscopy in scientific research, i.e. after the advent of ultrasonic transducers and lasers. Specifically, in 1971, Kruezer and Patel[3] observed that ultra-trace[xxi] gas constituents could be detected by laser-induced PA generation. In the last decades, PA imaging has been drawing increasing attention from various research fields, mainly biomedicine, but also chemistry, material science, physics.[4-6] The widespread application of this technique is mainly due to the possibility to overcome the penetration limit into scattering media, which instead affects other imaging modalities – i.e. pure optical techniques, such as Confocal Microscopy, Two-Photon Microscopy, and Optical Coherence Tomography. The combination of high ultrasonic resolution and strong optical contrast in a single modality[7] enables *in vivo* imaging of biological substrates, ranging from cells to organs. Noteworthy are the preclinical applications of PA imaging to the investigation of metabolic disorders through the mapping of oxygen saturation in haemoglobin,[8,9] the analysis of drug release processes,[10,11] and the detection of cancer cells.[12,13]

In more recent years, PhotoAcoustic Spectroscopy (PAS), which is based on the acquisition of photoacoustic spectra obtained after irradiation of the specimen at

[xxi] At the sub-part-per billion level.

different laser wavelengths, has been introduced in artwork diagnostics. The spectral dependence of the emitted acoustic waves makes it possible to identify the absorbing species.[14] Specifically, PAS has proven effective for pigment analysis in different types of Cultural Heritage items, including archaeological ceramics, paintings and frescos.[15-17] In 2017 Near Infrared PhotoAcoustic Imaging[18] (NIR-PAI) was introduced for the disclosure of hidden features such as underdrawings or original sketches underneath the painted surface of artworks.

In the framework of this project, PhotoAcoustic Signal Attenuation Analysis (PAcSAA), a novel method based on the photoacoustic attenuation effect was tested for thickness measurement of thin painting acrylic layers with micrometric precision. *Ad hoc* designed samples consisting of acrylic paint layers (Primary Red Magenta, Cadmium Yellow, Ultramarine Blue) of various thickness laid on glass substrates were realized for the specific application. Ultrasonic attenuation models were obtained for each pigment and used to fit the data acquired on a purposely inhomogeneous painted mock-up simulating a real canvas painting. Thickness measurements obtained with PAcSAA were were validated by comparison with Optical Coherence Tomography (OCT) and cross-section analysis. The observed agreement between the two techniques demonstrated the reliability of frequency-dependent ultrasonic attenuation analysis in providing thickness information for different pigments, overcoming light scattering and absorption effects affecting optical techniques. These features make PAcSAA well-suited for Cultural Heritage diagnostics, contributing to a deeper knowledge of artworks' internal structure.[19]

A further development of photoacoustic analysis on paintings is the introduction of a novel method demonstrating the imaging capabilities of PAcSAA, named PhotoAcoustic Signal Attenuation Imaging (PAcSAI),

allowing the direct comparison with other currently applied imaging techniques (e.g. OCT) for the acquisition of in-depth information on broad regions of the examined artwork. PAcSAI was applied in combination with Near Infrared PhotoAcoustic Imaging (NIR-PAI) for the visualization of high-absorbing materials underneath the painted surface. Using the fundamental and second harmonic wavelength of a Nd:YAG laser source, it was possible to acquire both cross-sectional information of painted layers and high resolution images of features underneath the painted surface, such as hidden drawings. The so-obtained imaging data were validated by comparison with Optical Coherence Tomography.[20]

1.2. Photoacoustic principle and attenuation effect

The photoacoustic phenomenon can be expressed through the wave-like photoacoustic equation[21]

$$\left(\nabla^2 - \frac{1}{u_s^2}\frac{\partial^2}{\partial t^2}\right) p(\vec{r},t) = -\frac{\beta}{C_P}\frac{\partial H(\vec{r},t)}{\partial t} \qquad (1)$$

where $p(\vec{r},t)$ is the spatiotemporal pressure function; $H(\vec{r},t)$ the heating function defined as the thermal energy converted per unit volume and unit time following light exposure; u_s the speed of sound in the propagation medium; β the thermal coefficient of volume expansion; C_P the specific heat capacity at constant pressure. The PA waves propagation in an medium is described by the left term of Eq. (1), whereas the waves source is represented by the right term.[6] The equation shows that the propagation of a PA wave is proportional to the first time derivative of the heating function: the thermoelastic expansion of the medium will then produce PA waves propagation only when the heating changes over time. This latter effect is typically obtained with pulsed or

intensity modulated lasers.[22] The efficiency of the process relies on the presence of absorbers with high-absorption cross section (σ_a), which is related to their absorption coefficient (μ_a) and density (N_a) by $\sigma_a = \mu_a/N_a$. For instance, larger molecules generally present greater absorption cross sections, and systems like nanoparticles with surface plasmon resonance are characterized by larger absorption cross sections than most organic dye molecules.[23]

The PA effect also relies on the thermal conversion efficiency η_{th} – i.e. the percentage of absorbed energy, which is converted into heat – and on the non-radiative relaxation of excited molecules to the ground state. Therefore, by minimizing radiative relaxation, such as fluorescence and phosphorescence, it is possible to increase the efficiency of the PA signal generation.[6]

As generated photoacoustic waves are transmitted through lossy media, a portion of acoustic energy is gradually degraded into thermal energy due to the occurrence of two physical mechanisms: a) heat diffusion, and b) momentum exchange among the vibrating molecules.[24] Heat diffusion takes place when thermal energy flows spontaneously from the compression regions of rapid average molecular motion and temperature, towards rarefaction regions characterized by a lower temperature. The molecular momentum transfer is a result of the internal friction (viscosity) between adjacent regions of the propagation medium with differing motion. Similarly to optical radiation or x-rays, the attenuation of a plane monochromatic acoustic wave is described by an exponential decay equation[25]

$$p(z) = p(0)e^{-a(f)z} \tag{2}$$

where $p(z)$ is the pressure amplitude of the acoustic wave at distance z, $p(0)$ the initial pressure, and $a(f)$ the frequency-dependent acoustic attenuation coefficient, usually expressed in dB/cm for 1 MHz wide frequency bands. For

many common media such as polymers or biological tissues, the latter coefficient has a nearly linear dependence on frequency,[24,25] entailing a stronger attenuation effect on the higher frequency components of the propagating acoustic wave, which results broadened and reduced in amplitude.[26] Extensive mathematical analysis of this effect has shown that the exact knowledge of the photoacoustic attenuation model together with the respective attenuation coefficients could be used to determine the thickness of an object.[27,28]

2. PhotoAcoustic Attenuation Signal Analysis (PAcSAA)

2.1. Samples

A set of acrylic tempera samples (Fig. 1) was prepared using three Extra-fine Acrylic colours (Maimeri Brera©, IT): Primary Red Magenta PV19 – 73900 (Quinacridone [$C_{20}H_{12}N_2O_2$], organic); Cadmium Yellow PY35–77205 (Cadmium Sulfide [CdS], inorganic); Ultramarine Blue PB29 – 77007 (Sodium Polysulphide-Aluminosilicate [Na_3P, $xAl_2O_3.ySiO_2$], inorganic). The set consists of nine samples on glass cover-slips (2.5×3 cm^2, 140 μm thickness). Each colour was laid in three different thicknesses using a tape 50 μm thick (Kapton© cypress) as reference: 50, 100 and 200 μm paint thicknesses were obtained by superimposing, on the border of the glass, one, two or four layers of tape, respectively. The paint was laid as homogeneously as possible using a glass spatula.

A mock-up simulating a real acrylic-tempera painting was also realized on cotton canvas, which was prepared with a gypsum-based layer. The tempera was obtained by dispersion of Ultramarine Blue 4503 powder (Kremer©) in an

acrylic binder (copolymer butyl-methacrylate – i.e. Lascaux© Acrylic Adhesive 498 HV- in aqueous solution), and applied on the canvas by brush.

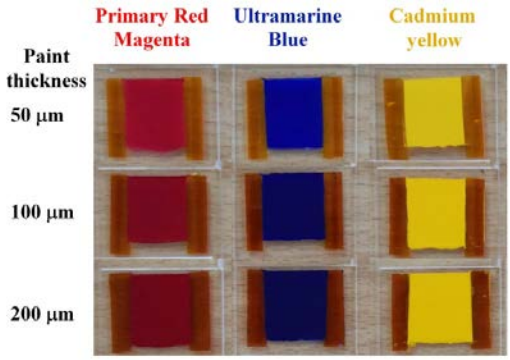

Fig. 1. Set of acrylic paint on glass with different thickness.

2.2. Methods

2.2.1. Optical Coherence Tomography

The tomographic analysis, used for assessing PAcSAA results, was performed using the time-domain confocal OCT prototype (operating wavelength: 1550 nm; axial resolution: 10 μm in air; lateral resolution: 2.5 μm).[xxii] For each sample, an OCT in-depth profile was acquired (20 mm length, 5 μm sampling step and 1 mm length, 1 μm sampling step in the y and z scanning directions, respectively), resulting in a 4000×1000 pixel tomographic image. For measuring the paint thickness, the signal from the glass support outside the painted region was taken as a reference, considering that 1 pixel corresponds to 1 and 5 μm on z and y axis of the tomographic image, respectively.

[xxii] Detailed description reported in Appendix 1.

2.2.2. PAcSAA experimental setup

The PAcSAA experimental apparatus (Fig. 2a) is based on a diode-pumped Q-switched Nd:YAG laser emitting at 1064 nm (QIR-1064-200-S, CrystaLaser LC, Reno, NV, USA; pulse energy: 29.4 μJ, pulse duration: ~ 8 ns, selected repetition rate: 5 kHz, M^2 value: 1.2). The beam is focused on a Lithium triborate (LBO) second harmonic generation crystal to be partially transformed into visible light at 532 nm, which is highly absorbed by the paint layers under investigation and leads to the excitation of photoacoustic waves. A parallel monochromatic beam, generated by a collimating lens and a narrow band-pass optical filter (FF01-531/40-25, Semrock, Rochester, NY, USA) placed after the LBO crystal, is expanded by a 6X magnification telescope consisting of two positive lenses. Visible radiation is attenuated using a set of neutral density filters and reflected into a modified inverted optical microscope (Labovert, Leitz, Wetzlar, Germany). A low numerical aperture air-immersion objective lens (Achromat 8X, LOMO, St. Petersburg, Russia; NA: 0.2) focuses the beam on the backside of the sample, at the interface between the paint layer and the substrate. The pulse energy at the focal point is estimated 200 nJ and 640 nJ for the glass coverslip and canvas samples, respectively. Each sample is placed into an optically transparent Petri dish filled with distilled water, ultrasound gel (Transound, EF Medica Srl, Appiano, Italy) or a water-based gel of cellulose ether (carboxymethyl cellulose gel - CMC 3%), acting as coupling medium to ensure an efficient transmission of the laser-induced ultrasound signals. CMC was used in this case, being an inert material well-suited for artworks' diagnostics, widely used for the cleaning of the painted surfaces due to its safety features, wide availability, and low cost. The Petri dish is fixed on a high-precision motorized xy micrometric stage (8MTF-75LS05, Standa, Vilinius, Lithuania) used to select the region to be measured, whereas the focal plane positioning is performed by the built-in manual z-control of the

microscope. For the detection of the generated photoacoustic waves, a single element spherically-focused broadband ultrasonic transducer (HFM28, SONAXIS, Besancon, France; Central frequency: 73 MHz, Focal distance: 4.53 mm) is immersed into water in a confocal and coaxial configuration.

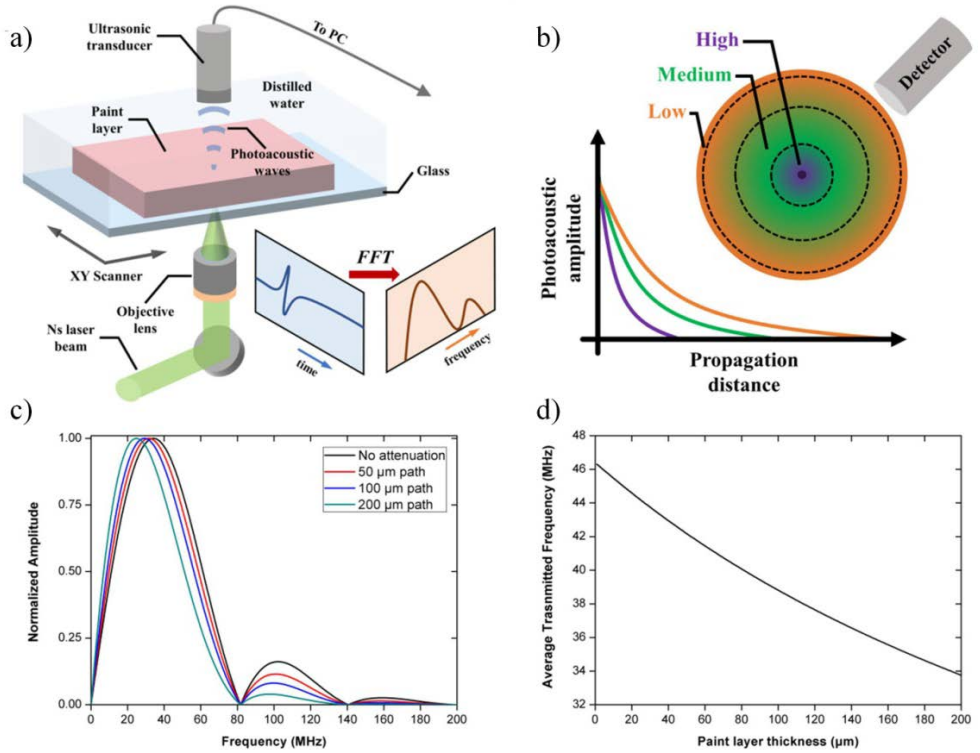

Fig. 2. PAcSAA experimental setup and photoacoustic signal attenuation simulation. a) Schematics of the photoacoustic detection apparatus during the measurement of a paint layer on glass sample. Post-processing of the acquired time-domain data through a Fast Fourier Transform (FFT) operation reveals the relative attenuation of each frequency component in the original photoacoustic signal. b) Visual representation of low, medium and high frequency components propagation as a function of the distance from the detector. c) Simulation of the frequency-dependent photoacoustic signal attenuation in a typical medium with attenuation coefficient equal to 1 dB cm^{-1}, for different transmission path lengths. The simulated signals are generated from a homogeneous spherical absorber with a diameter equal to the FWHM of the diffraction limited ultrasonic transducer's acoustic focus (~ 26 µm), following the excitation through a 5 ns Gaussian pulse. d) Plot of the Average Transmitted Frequency (ATF – see Eq. 4) within the range of 0-200 MHz, as a function of propagation path length, using the previous simulation parameters.

The acquired time-domain signal is enhanced using a low noise RF amplifier (AU-1291, Miteq, NY, USA; Gain: 63dB), transmitted to a high-speed data acquisition card (PCIe-9852, ADLINK, Taipei, Taiwan; sampling rate: 200 MS/s), digitized and recorded by a computer using custom-made scripts developed in MATLAB environment. In order to improve the Signal to Noise Ratio (SNR), for each measurement sequential photoacoustic waveforms were averaged over 128 or 1024 incident laser pulses, depending on the signal levels.

2.3. Results

2.3.1. Simulation of photoacoustic attenuation

Photoacoustic signal propagation through paint layers of different thickness was simulated prior to PAcSAA measurements in order to optimize the experimental parameters. The frequency-dependent attenuation of the generated ultrasonic waves along the detection path (Fig. 2b) was approximated by the time-domain solution of the general photoacoustic equation for a homogeneous spherical absorber,[22] with a diameter equal to the acoustic diffraction limited focus of the employed transducer (~ 26 μm). The simulated impulse-excited signal was further convolved with a Gaussian function having a full width at half maximum equal to 5 ns, accounting thus for the finite pulse duration effect on photoacoustic excitation. A typical 1 dB cm^{-1} acoustic attenuation coefficient was considered for wave propagation through acrylic layers,[29] with thickness of 50, 100, and 200 μm, respectively. Fast Fourier Transformation of the convoluted waveforms was performed to provide a normalized amplitude spectrum revealing the relative contribution of each frequency component for different transmission paths, in the 0-200 MHz range (Fig. 2c). The simulation shows the decay within the bands 80-140 and 140-200 MHz, as well as the red-

shift of the predominant band between 0 and 80 MHz towards lower frequencies.

To estimate the ultrasonic attenuation through paint layers of various thicknesses, we have calculated the average transmitted frequency (ATF) was calculated using the previous simulation settings. ATF is introduced as representative measure of the overall photoacoustic attenuation within a given detection bandwidth, by taking into account the relative amplitude contribution of each frequency composing the signal. This weighted average value is representative of the mean frequency component that has survived the uneven acoustic attenuation during wave propagation, and is expected to decrease as a function of path length. More specifically, ATF was calculated by the equation

$$ATF = \frac{\sum_{i=0}^{N} A_i f_i}{\sum_{i=0}^{N} A_i} \tag{3}$$

where A_i is the normalized amplitude of each frequency component f_i, and f_N is the upper frequency limit, which in this case was set equal to 200 MHz. Fig. 2d shows the plot of ATF as a function of layer thickness z within the range 0-200 μm (step of 1 μm), revealing an exponential decrease response ($ATF = y = y_0 + Ae^{-Rx}$). This is described by the relation

$$ATF = 23.88 + 22.48e^{-4.09\times10^{-3}z} \tag{4}$$

following a nonlinear curve fitting of the simulation points (R^2>0.999). It is worth mentioning that such observed behaviour is expected as a result of the characteristic exponential decay of acoustic amplitude during propagation in lossy media. This simulation predicts more than 8 MHz ATF difference between acrylic paint layers 50 and 200 μm thick, which can be easily detected

by a standard broadband transducer. The preliminary evaluation of PAcSAA capabilities through the adopted simple physical model showed that the proposed technique is in principle sensitive enough to provide micrometric precision in thickness measurements, with a resolution limited only by the effective detection bandwidth.

After OCT analysis, the Primary Red Magenta samples (50, 100 and 200 μm paint thickness) were measured with PAcSAA, based on the intense superficial absorption of the incident radiation by the pigment.[30] The recorded time-domain signals (Fig. 3a-c) were shifted into Fourier domain, to generate a normalized photoacoustic amplitude spectrum for each measured layer (Fig. 3d-f). The predominant spectral bands (10-80 MHz) were nonlinearly fitted with 4th order polynomial curves (colour curves in amplitude spectra in Fig. 3g) to detect their peak frequencies.

For all thicknesses, the amplitude spectrum consists of two well-distinct frequency bands with upper limits at 80 and 140 MHz respectively. These frequency limits are mainly determined by the excitation (optical) and detection (ultrasonic) parameters, which remain unchanged during the measurement process. Nevertheless, a consistent shift towards lower frequencies can be detected in the predominant spectral band versus an increasing layer thickness, as it is clear from the estimated maximum amplitude frequency values (43.76 MHz for the 50 μm layer, 41.44 MHz for the 100 μm layer and 35.37 MHz for the 200 μm layer). These results are in excellent agreement with simulation predictions, validating thus the correctness of the experimental procedures.

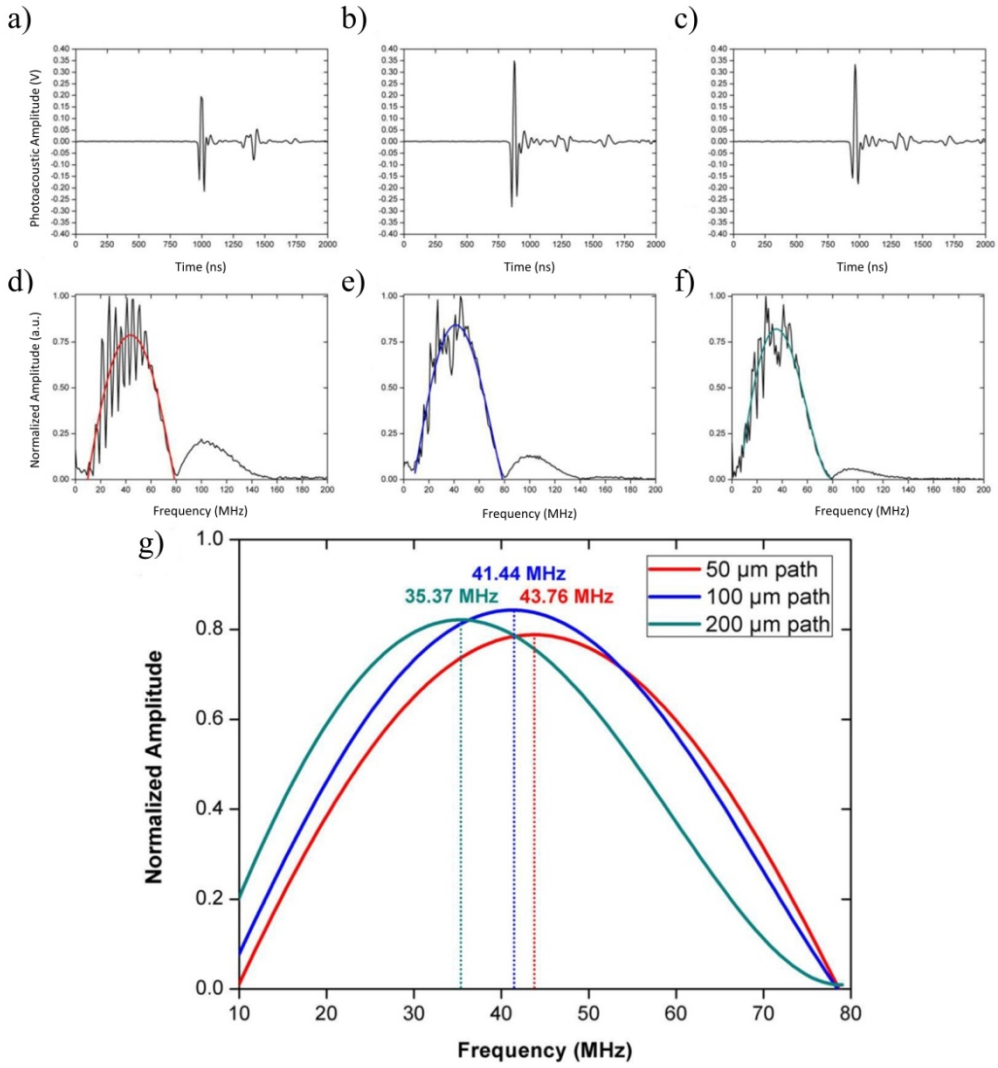

Fig. 3. Photoacoustic signal attenuation effect on Primary Red Magenta paint layer samples of different thickness. a-c) Time-domain photoacoustic signals recorded from 50, 100 and 200 µm Primary Red Magenta paint layers. d-f) Normalized amplitude spectrum of the previous signals following a FFT. Coloured curves indicate a 4th order polynomial fitting for the detected predominant spectral band (10-80 MHz). g) Aggregate plot of the fitted polynomial curves showing the peak frequencies of the predominant band.

Based on the good agreement between theoretical simulations of photoacoustic signal attenuation and experimental results on Primary Red Magenta samples, the ATF analysis was applied to all the samples. Scatter plots of the ATF values

in the effective detection band 10-130 MHz versus layers' thickness are shown in Fig. 4.a-c for the three investigated acrylic paints. Black line corresponds to the fitting of the experimental points (ATF values) by the exponential decay function $y = y_0 + Ae^{-Rx}$. Error bars represent the standard deviation calculated on five sequential ATF measurements in different areas of the sample around the central region. The thickness of each layer was compared with the results from OCT imaging, which revealed the profile of the paint surface at high spatial resolution (Fig. 4 d-f).

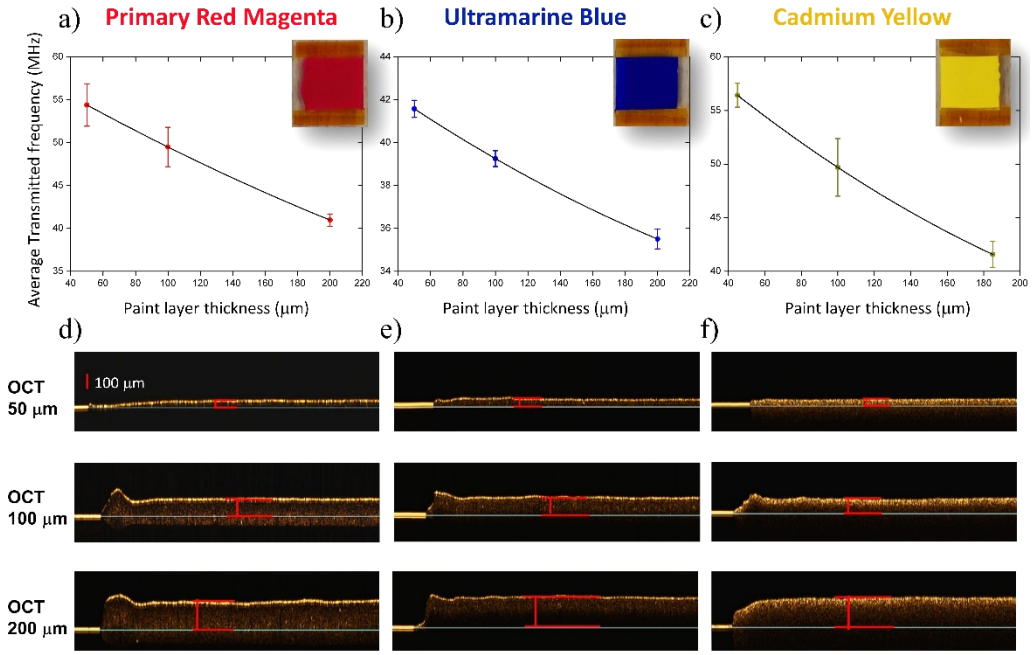

Fig. 4. Average transmitted frequency (ATF) correlation and OCT tomograms in Primary Red Magenta, Ultramarine Blue and Cadmium Yellow layers. a) Plot of ATF versus OCT measured thickness for three Primary Red Magenta layers. Error bars correspond to the standard deviation calculated on five sequential ATF measurements at different regions of the sample. Black line represents the exponential fitting of the experimental points. d) OCT profiles of three paint layers (50, 100 and 200 μm). Similar data are presented for Ultramarine Blue (b, e) and Cadmium Yellow (c, f) samples. Bright-field images of the samples are displayed on each respective ATF graphs (up-left).

The estimated fitting parameters for the three pigments are summarized in Table 1. In all cases, the quality of the exponential fitting is very high (R^2>0.999), confirming an excellent accordance with theoretical predictions. It is noteworthy that fitting parameters for the three pigments differ significantly, especially in case of Ultramarine Blue, as a result of their diverse acoustic and optical properties.

Table 1: Parameters for the exponential decay fitting ($ATF = y = y_0 + Ae^{-Rx}$) of the average transmitted frequency (ATF) measured as a function of thickness for the three analysed paints.

	ACRYLIC PAINTS		
ATF fitting parameters	Primary Red Magenta	Ultramarine Blue	Cadmium Yellow
y_0 (offset, MHz	-3.10×10^{-2}	7.54	-3.38
A (amplitude, a.u.)	59.82	36.19	65.46
R (decay constant, μm^{-1})	1.89×10^{-3}	1.29×10^{-3}	2.03×10^{-3}

2.3.2. PAcSAA measurement on the canvas sample

PAcSAA methodology was then tested on the canvas mock-up covered with a layer of Ultramarine Blue (Fig. 5a). A bright-field microscope cross-sectional image, taken at the edge of the canvas, is shown in Fig. 5b. An average painting thickness of 200 μm was evaluated from the cross-section. The sample was irradiated from its back side using an inert ultrasound gel as coupling medium, which can be considered compatible with painting materials. The recorded time-domain photoacoustic waveform is presented in Fig. 5c, averaged over 1024 measurements for SNR improvement. In this case, the maximum photoacoustic amplitude (Fig. 5c) is about two orders of magnitude lower compared to the time-domain signals of Primary Red (Fig. 3), due to the strong

scattering of the preparation layer, which drastically reduces the energy fluence reaching the paint. The respective amplitude spectrum (Fig. 5d) provided an ATF value equal to 35.28 MHz within the effective detection bandwidth (10-130 MHz). It has to be mentioned that the low frequency noise in the region 0-10 MHz appears probably due to the imperfect electrical grounding of the detection scheme, which may produce some observable impact in case of low signals. On the other hand, the high frequency components at around 140 MHz can be attributed to slight electronic noise/interference effects, usually appearing in such sensitive measurements.

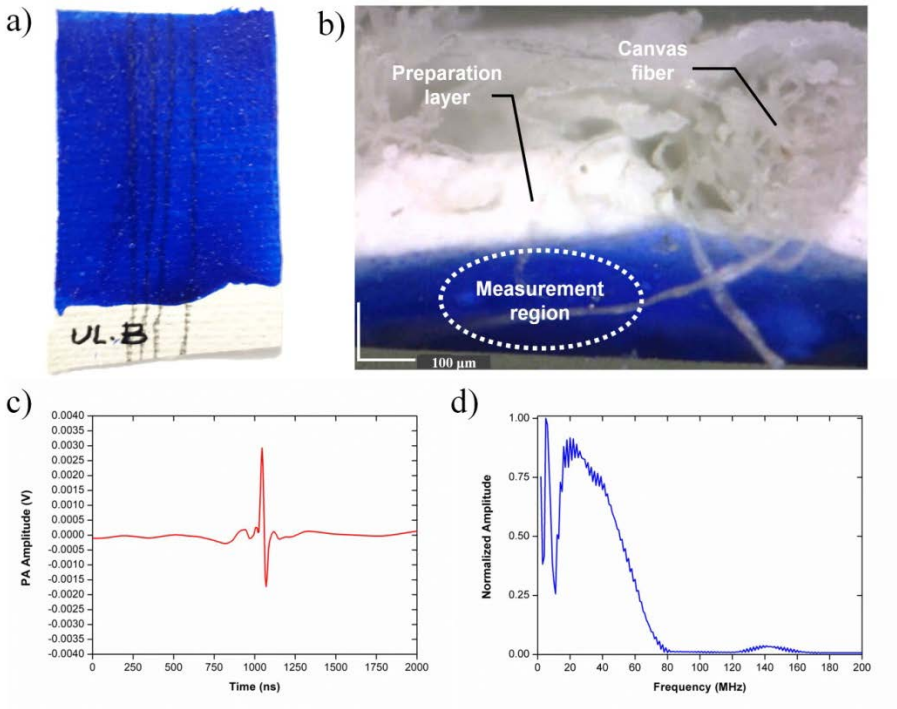

Fig. 5. Thickness measurement of Ultramarine Blue layer applied on canvas with PAcSAA method: a) Bright-field image; b) Cross-section bright-field image at sample's edge; c) Time-domain photoacoustic waveform; d) Normalized amplitude spectrum.

The measured value of ATF corresponds to a paint layer thickness of nearly 210 μm, using the previously shown exponential function for Ultramarine Blue pigment (Fig. 4b), which is in very good agreement with the value estimated by the cross-section image (Fig. 5b).

3. Combined photoacoustic imaging: PAcSAI and NIR-PAI

3.1. Samples

Four canvas samples (3×3 cm^2) were prepared for the specific application (Fig. 6a). Four different geometric patterns, simulating the underdrawing, were sketched with graphite pencil in the central area of each sample on the industrially prepared gypsum-ground covering the canvas support (Fig. 6). The overlaying paint layers were realized with four already described acrylic paints, Primary Red Magenta, Cadmium Yellow, Ultramarine Blue, plus Permanent Green Light (PG7 – 74260, PW6 – 77891, PY97 – 11767. The acrylic paints were laid using Kapton© tape as a reference (two superimposed layers of 50 μm thickness each), in order to obtain for all the same thickness of around 100 mm.

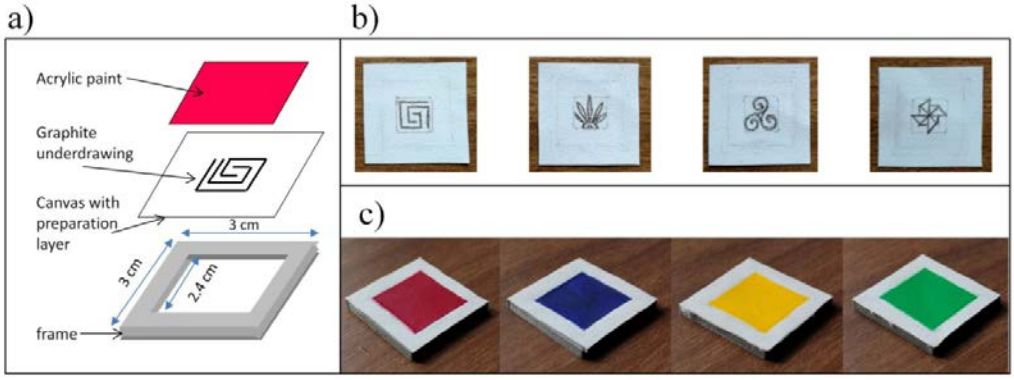

Fig. 6. Set of samples analysed with NIR-PAI: a) scheme and size; b) graphite underdrawings; c) acrylic paints (from the left: Primary Red Magenta, Ultramarine Blue, Cadmium Yellow, Permanent Green Light), laid over the graphite pattern.

3.2. Methods

3.2.1. Combined-imaging setup

The combined-imaging setup (Fig. 7) is a modified version of the previously described setup used for PAcSAA. The main difference is the excitation source, which is based on a diode-pumped Q-switched Nd:YAG laser at 1064 nm (QIR-1064-200-S, CrystaLaser LC, Reno, NV, USA; pulse energy: 29.4 µJ, pulse duration: ~ 8 ns, selected repetition rate: 5 kHz, M^2 factor: 1.2) whose Second Harmonic (at 532 nm) is generated by focusing the beam on a Lithium triborate crystal. To switch between infrared and visible photoacoustic excitation, two bandpass filters (FL1064-10, Thorlabs, Newton, New Jersey, U.S. and FF01-531/40-25, Semrock, Rochester, New York, U.S.) are used, which are mounted on a filter wheel.

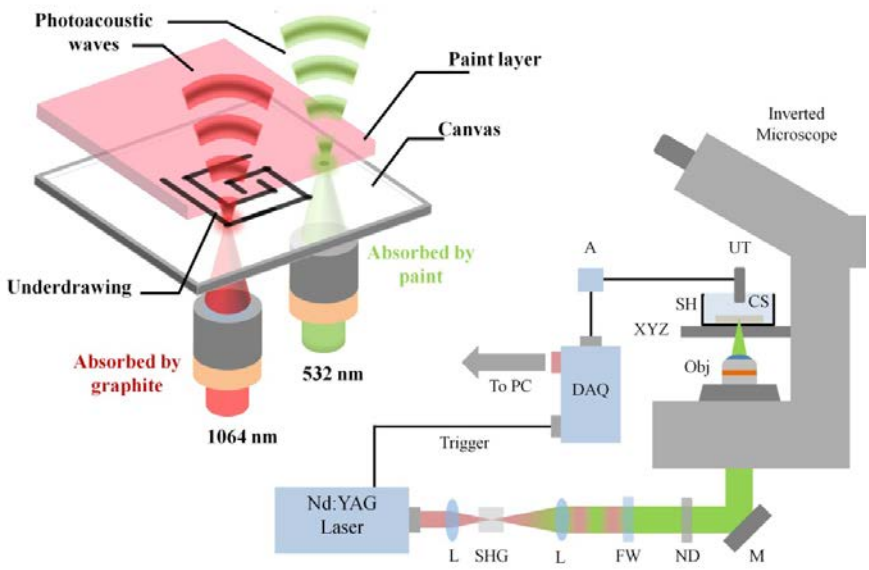

Fig. 7. Photoacoustic microscopy setup for the combined imaging (PAcSAI and NIR-PAI) of painting samples. L, lens; SHG, second-harmonic generation crystal; FW, filter wheel; ND, neutral density filters; M, mirror; Obj, objective lens; XYZ, 3D translational stage; SH, sample holder; CS, canvas sample; UT, ultrasonic transducer; A, amplifier; DAQ, data acquisition card.

As in the previous setup, the beam was focused on the backside of the sample, at the interface between the paint layer and the substrate, by the same air immersion objective lens (Achromat 8X, LOMO, St. Petersburg, Russia; NA: 0.2), after proper attenuation. The sample was placed into an optically transparent Petri dish filled with carboxymethyl cellulose gel - CMC 3%, acting as coupling medium to ensure an efficient transmission of the laser-induced ultrasound signals. In this upgraded setup, the Petri dish was fixed on a high-precision motorized xy micrometric stage (8MTF-75LS05, Standa, Vilinius, Lithuania) enabling the point-by-point scanning over the region of interest, whereas the focal plane positioning was performed by the built-in manual z-control of the microscope. As in the previous version of the setup, for the detection of the generated photoacoustic waves, a single element spherically-focused broadband ultrasonic transducer (HFM28, SONAXIS, Besancon, France; central frequency: 73 MHz, focal distance: 4.53 mm) was immersed into CMC in a confocal and coaxial configuration with respect to the optical axis.

3.2.2 Optical Coherence Tomography

The Spectral-domain OCT Thorlabs Telesto II[xxiii] was used for the in-depth imaging of the sample. Tomographic cubes (size: 9×9×1 mm^3) were acquired with sampling step of 5 μm on x and y, and 3.55 μm on z, enabling the visualization of the graphite underdrawing (Fig. 8b), this latter for comparison with the Near Infrared PhotoAcoustic Imaging session. A clearer cross-sectional visualization of the paint layer was obtained with the Time-Domain confocal-OCT prototype operating at 1550 nm (axial resolution: 10 μm in air; lateral resolution: 2.5 μm). The thickness of each paint layer resulted 82 ± 12

[xxiii] Detailed description of the device in Appendix 1.

μm for Primary Red Magenta (see Fig. 4.c), 85 ± 11 μm for Ultramarine Blue, 93 ± 10 μm for Cadmium Yellow, and 92 ± 6 μm for Permanent Green Light.

3.2.3. Near Infrared - PhotoAcoustic Imaging (NIR-PAI)

The samples were firstly analysed with NIR-PAI. Strong light scattering generates a broad illumination spot, inducing the generation of photoacoustic waves in the highly absorbing regions of the underdrawing pattern. Since the NIR transparent overlying paint layers have a virtually zero contribution in the image formation, the signals reveal exclusively the hidden sketch at a high contrast level. The photoacoustic signal is detected by a spherically focused ultrasonic transducer immersed in a layer of carboxymethyl cellulose (CMC) gel layer (see §§ 3.2.1) applied on the front surface of the painting and serving as an immersion medium for the effective ultrasound wave propagation from the substrate to the detector. The detection bandwidth of the generated photoacoustic waves is centred at 20 MHz, providing thus an effective trade-off between signal to noise ratio and spatial resolution. The photoacoustic image is generated by raster scanning of the painting using a motorized XY stage to achieve a point-by-point data acquisition over the region of interest. The samples were irradiated from their backside (scanning area: 10×10 mm^2, 750 averaging measurements per point), exploiting the high absorption of graphite at 1064 nm and the relative transparency of the overlying paint layer at this spectral region. Following the irradiation, the photoacoustic waves are generated in correspondence of the underdrawing pattern and then transmitted through the paint, thus revealing exclusively the hidden sketch. In Fig. 8, the NIR photoacoustic images of the underdrawings (c) are reported in comparison to Spectral-OCT images (b). The two techniques provide effective results for the visualization of the underdrawings, with some differences in terms of measurements procedure and images resolution. On one hand, PA images show

high contrast between the graphite and the background, enabling the visualization of the texture pattern of the canvas support, which is not so distinguishable in OCT images. On the other hand, OCT analysis presents the advantage to perform the measurement without the need of a coupling medium to enhance the signal transmission (CMC for PA analysis), thus fully respecting the non-invasiveness requirement for CH object diagnostics.

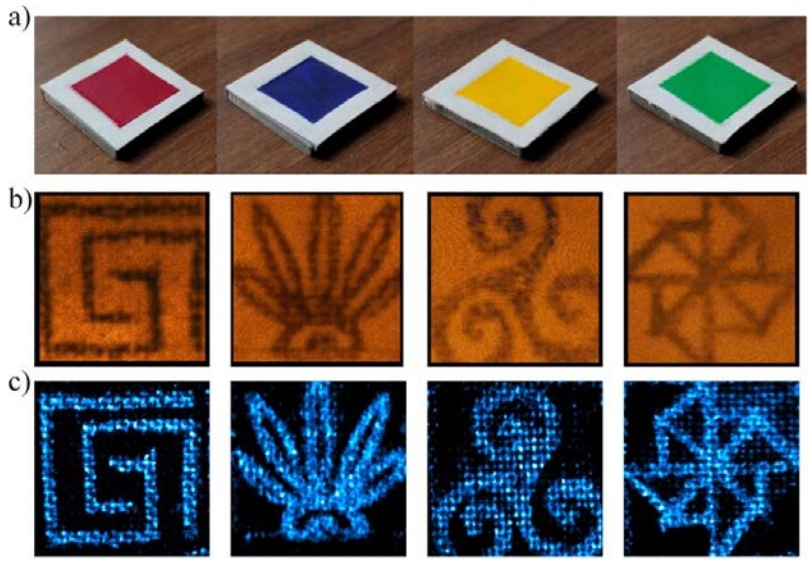

Fig. 8. a) Bright-field images of the four canvas samples; b) underdrawing visualization though Spectral-OCT (images size 9×9 mm^2, sampling step of 5 μm on x and y, and 3.55 μm on z); c) NIR photoacoustic imaging (scanning area: 10×10 mm^2, 750 averaging measurements per point).

3.2.4. PAcSAI test application

The PhotoAcoustic Signal Attenuation Imaging (PAcSAI) method was firstly tested on a multi-layer sample consisting of a number of superimposed black tape layers producing an increasing thickness, on a glass support (cover-slip 2.5×2.5 cm; 150 μm thick). The thickness of each area (1 to 5 tape layers) was preliminarily assessed by a micro-profilometer (Perthometer S5P, Mahr,

Göttingen, Germany) with one single tape measured at 110 ± 5 μm (Fig. 9a). The sample was irradiated from the back side with the 2nd harmonic of the Nd:YAG laser beam. The generated time-domain photoacoustic signal was recorded point by point over a scanning area of 16 mm^2 resulting in a 200 by 200 pixels image.

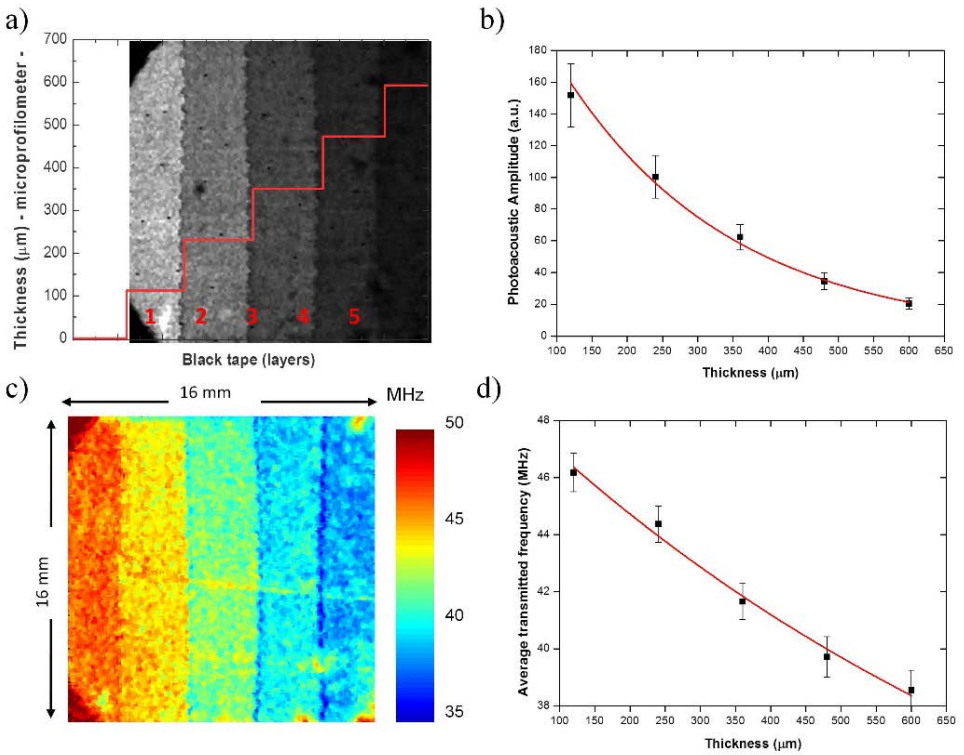

Fig. 9. PhotoAcoustic Signal Attenuation Analysis (PAcSAA) of the black tape sample. a) Maximum amplitude projection photoacoustic image in greyscale showing the different layers, with the respective thickness values obtained with microprofilometer (red line); b) Plot of the average photoacoustic amplitude as a function of thickness; c) Average Transmitted Frequency (ATF) image displayed within the range 35-50 MHz; d) Plot of the average ATF values as a function of total layer thickness.

Data were processed in MATLAB and ImageJ environments for the reconstruction of the photoacoustic amplitude image (Fig. 9a) where, for each

pixel, the brightness value corresponds to the maximum amplitude projection obtained by averaging 128 waveforms, which are recorded for SNR enhancement. The amplitude values were calculated as an average on selected areas of ~ 4600 pixel at the centre of each region of different thickness, and then plotted as a function of thickness. The best fitting curve demonstrates an exponential decay of the photoacoustic amplitude with the propagation length through the sample's volume (decay constant: 4.18×10^{-3}, R^2=0.992) (Fig. 9b). Finally, an Average Transmitted Frequency (ATF) colour-scale image was generated within the acoustic band of 10-100 MHz, following a FFT of the acquired time-domain photoacoustic waveforms (Fig. 9c). Similarly to the amplitude image, the ATF values were calculated as the average on the previously selected areas for each tape layer and plotted together with an exponential fitting curve (decay constant: 1.08×10^{-3}, R^2 =0.982) as a function of layer thickness (Fig. 9d).

3.3. Results

Based on these preliminary results, the effectiveness of PAcSAI was evaluated on the Primary Red Magenta sample and compared with OCT analysis.

The tomographic cubes ($9\times9\times1$ mm^3), acquired with sampling step of 5 μm on x and y, and 3.55 μm on z, clearly show the graphite underdrawing (Fig. 10b). The OCT image was acquired with 5 μm and 1 μm sampling step in y and z directions (image size 25 mm length and 1mm in-depth). The paint thickness was computed by averaging 12 measurements along the selected profile, resulting in 82 ± 12 μm (Fig. 10b).

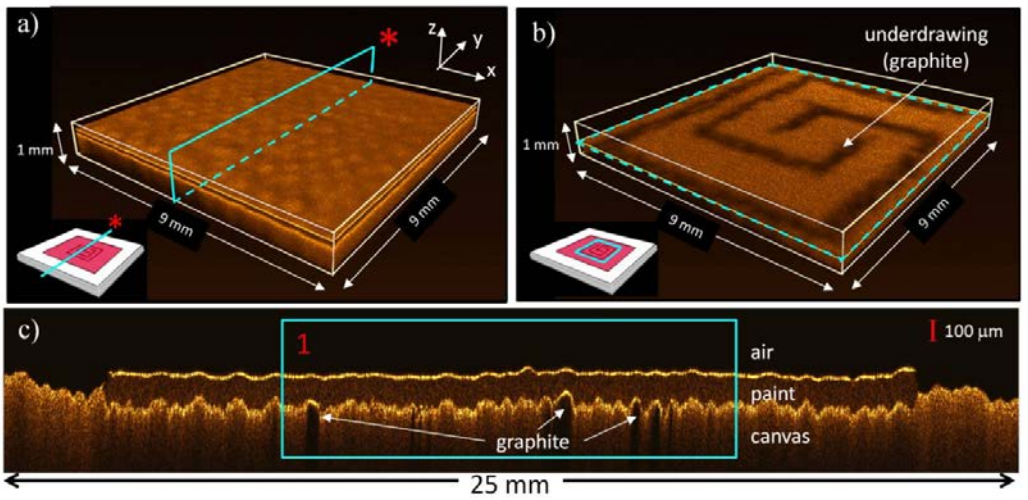

Fig. 10. OCT results. a) Tomocube showing the position of the tomographic image (light blue rectangle) acquired for the evaluation paint's thickness; b) x-y section of the tomocube showing the underdrawing; c) Tomographic image (average paint thickness: 82 ± 9 µm).

NIR-PAI was subsequently tested for the visualization of the underdrawing (Fig. 11a), as described in the previous section. Following the Near Infrared PhotoAcoustic Imaging, the evaluation of the paint's thickness was performed with PAcSAI (Fig. 11b). The sample was scanned in the previously analysed region using the 532 nm wavelength, by averaging over the same number of measurements for SNR improvement. Since light at 532 nm is absorbed by both graphite and red paint, the photoacoustic waves are generated over the entire scanned area and are attenuated according to the local thickness of the paint layer. The two amplitude images acquired at 1064 nm and 532 nm were merged in one single image as red and green channels respectively (Fig. 11c). Finally, to provide a map of paint thickness over the scanned region, we shifted the time domain waveforms recorded at 532 nm to the frequency domain, and estimated the ATF values for each point within the range of 10-130 MHz. Acoustic signals originated by the underdrawing regions are excluded from the analysis

since they are generated through the absorption of light by the graphite rather than the overlying paint. We used the exponential decay fitting parameters previously defined for Primary Red Magenta[19] to relate the estimated ATF values (MHz) with layer thickness x (μm) according to the relation

$$x = -529 \times ln\left(\frac{ATF + 0.03}{59.82}\right) \quad [5]$$

generating a PAcSAI map corresponding to the overlying paint layer thickness (Fig. 11d).

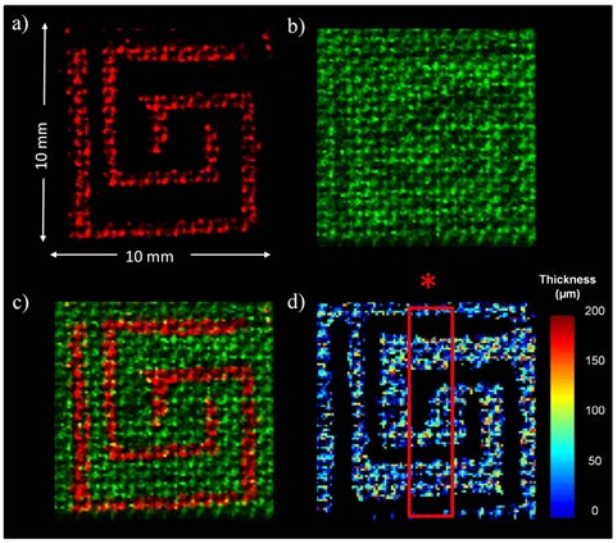

Fig. 11. Results of combined PA-imaging: a) Maximum Amplitude Projection (MAP) photoacoustic image at 1064 nm (red channel); b) MAP image at 532 nm (green channel); c) combined MAP images at 1064 and 532 nm; d) PAcSAI image with estimated paint thickness values on the colour-scale. The considered area for mean thickness measurement is highlighted by the red rectangle *.

To validate the capabilities of PAcSAI for thickness measurements in paint layers, the mean thickness was estimated for a representative area (outlined by the red rectangle in Fig. 11d) and compared it with the recorded OCT profiles. It has to be noted that all computed values smaller than the theoretical axial

resolution of the transducer (~ 15 μm)[31] were excluded from the analysis as measurement artefacts. The obtained thickness for the selected area (686 pixel) was 77.8 ± 1.9 μm, where measurement uncertainty corresponds to the standard error of the mean. PAcSAI results are in good agreement with OCT thickness (~ 82 μm), demonstrating the reliability of the proposed technique.

4. Discussion

Photoacoustic signal attenuation was investigated in acrylic paint layers of different thickness and chemical composition. Preliminary simulations allowed for the estimation of an Average Transmitted Frequency (ATF) function, applicable to ultrasonic attenuation through typical paint layers of various thicknesses. The simulation ensured the in-depth micrometric precision requested for painted artworks analysis. PhotoAcoustic Signal Attenuation Analysis (PAcSAA) on *ad hoc*-prepared samples enabled the calculation of fitting parameters for the exponential ATF function. The thickness of the three different acrylic paints was measured, showing excellent accordance with theoretical predictions. The reliability of the so obtained thickness values was assessed by comparison with OCT tomographic images.

PAcSAA methodology was then applied on a multi-layered mock-up simulating real paintings on canvas. The generated amplitude spectrum provided the ATF calculation for the assessment of paint layer thickness. Such measurement was validated by cross-sectional microscopy, revealing excellent agreement between the data obtained through the two modalities.

The quality of the results suggests the high potential of PAcSAA in the diagnosis of real artworks. Further experiments on different pigments would provide a deeper understanding of the deviations of the different paints' acoustic attenuation models. PAcSAA should be also evaluated for thickness

measurements on transparent or semi-transparent layers, for example, aged varnishes and *patinas* in general.

It was shown that the combination of PAcSAI and NIR-PAI modalities represents a promising diagnostic tool for the analysis of painted artworks. Here, for the specific application, measurement parameters for irradiation, acquisition, and scanning systems were optimized. All the results were validated with standard imaging techniques and pros/cons with respect to optical coherence tomography were highlighted. The possibility of high-resolution imaging to disclose the underdrawing, as well as stratigraphic information of paint layers using the same setup, turns definitely useful in case of conservation studies and restoring operations. The use of different laser's wavelengths would enable to extend the analysis to a variety of drawing materials and paint layers containing different pigments and binding media. Moreover, displaying the results as an image easies their interpretation by final users (restorers, curators, art historians) directly involved in conservation interventions.

A comprehensive study on PAcSAI of mixed paint layers constitutes a future research work, which will demonstrate the potential of this novel modality in Cultural Heritage diagnostics. In order to detect the thickness of a single layer in a multi-layered system, a proper wavelength should be selected, which is absorbed by the layer of interest and not by the other layers. This would confine the generation of photoacoustic wavelengths to that particular layer, while enabling the transmission of the radiation through the other layers. In principle, by tuning the wavelength according to each layer and knowing the attenuation coefficients of the materials, a complete stratigraphy would result. This issue will be one of our next goals, together with the study of mixtures.

Finally, a more direct comparison between PAcSAI and OCT profiles will be performed in a future study involving an upgraded experimental apparatus

(different scanning/excitation geometries, multi-wavelength excitation, high repetition rate lasers, acoustic frequency detection >120 MHz) and improved data processing procedures, taking into account the signal's time of flight. Under such conditions, PAcSAI 3D or cross-sectional imaging could be compared with high resolution OCT images.

For application on works of art, where non-invasiveness is a prerogative, an alternative solution to water-based media for the efficient transmission of the laser-induced ultrasound signals can be found. CMC (carboxy methyl cellulose) was used in this study based on the fact that it has been broadly employed as inert gelling agent for the cleaning of various types of artefacts due to its wide availability, low cost and safety features.[32.34] Such approach showed excellent results in terms of measurement quality and preservation of artwork's integrity. Nevertheless, other more sophisticated media, specifically formulated for art objects such as nanomaterials and complex colloids, could also be considered.[35,36] An immersion-medium-free approach is still feasible, by integrating a technologically advanced detection scheme, including fully non-contact interferometric ultrasonic detectors,[37,38] or, in some cases, air-coupled transducers[39] of high efficiency. The evaluation of contactless detection methods and their integration in an upgraded setup constitute future targets for research.

Finally, a future perspective includes the design and development of a portable PAcSAA device, enabling in situ analysis of real art objects. This implementation would fully provide cultural heritage hand-users/stakeholders with a powerful tool for the study of the complex internal structure of artworks.

References

[1] A. G. Bell, On the production and reproduction of sound by light, Amer. J. Sci., 20, 305-324 (1880).

[2] A. C. Tam, Applications of photoacoustic sensing techniques, Reviews of Modern Physics, 58, 2 (1986).

[3] L. B. Kreuzer, C. K. N. Patel, Nitric Oxide Air Pollution: Detection by Optoacoustic Spectroscopy, Science, 173, 3991, 45-47 (1971), doi:10.1126/science.173.3991.45.

[4] J. M. Yang, C. Favazza, R.M. Chen, J.J. Yao, X. Cai, K. Maslov, Simultaneous functional photoacoustic and ultrasonic endoscopy of internal organs in vivo, Nat Med, 18(8), 1298-303 (2012).

[5] C. Kim, C. Favazza, L.H.V. Wang, In vivo photoacoustic tomography of chemicals: high-resolution functional and molecular optical imaging at new depths, Chem Rev, 110(5), 2756-82 (2010).

[6] J. Yao, L.V. Wang, Photoacoustic tomography: fundamentals, advances and prospects, Contrast Media Mol Imaging, 6(5), 332-45 (2011).

[7] L. V. Wang, Tutorial on Photoacoustic Microscopy and Computed Tomography, IEEE J. Sel. Top. Quantum Electron, 14, 1 (2008).

[8] L. V. Wang and S. Hu, Photoacoustic tomography: In vivo imaging from organelles to organs, Science, 335(6075), 1458-1462 (2012) doi:10.1126/science.1216210.

[9] X. Wang, X. Xie, G. Ku, L. V. Wang, G. Stoica, Noninvasive imaging of hemoglobin concentration and oxygenation in the ratbrain using high-resolution photoacoustic tomography, J. Biomed. Opt., 11(2), 024015 (2006).

[10] S. Kim, Y.-S. Chen, G.P. Luke, and S.Y. Emelianov, In vivo three-dimensional spectroscopic photoacoustic imaging for monitoring nanoparticle delivery, Biomed. Opt. Express, 2(9), 2540-2550 (2011) doi:10.1364/BOE.2.002540.

[11] H. J. Lee, Y. Liu, J. Zhao, M. Zhou, R.R. Bouchard, T. Mitcham, M. Wallace, R.J. Stafford, C. Li, S. Gupta, M.P. Melancon, In vitro and in vivo mapping of drug release after laser ablation thermal therapy with doxorubicin-loaded hollow gold nanoshells using fluorescence and photoacoustic imaging, J. Control. Release, 172(1), 152-158 (2013) doi:10.1016/j. jconrel.2013.07.020.

[12] S. Mallidi, T. Larson, J. Tam, P. P. Joshi, A. Karpiouk, K. Sokolov and S. Emelianov, Multiwavelength photoacoustic imaging and plasmon resonance coupling of gold nanoparticles for selective detection of cancer, Nano Lett. 9(8), 2825-2831, (2009) doi:10.1021/nl802929u.

[13] A. Taruttis and V. Ntziachristos, Advances in real-time multispectral optoacoustic imaging and its applications. Nat. Photonics, 9, 219-227 (2015) doi:10.1038/nphoton.2015.29.

[14] D. C. Dumitra, D. C. Dutu, C. Matei, A. M. Magureanu, M. Petrus, C. Popa, Laser photoacoustic spectroscopy: principles, instrumentation, and characterization, JOAM, 9, 12, 3655-3701 (2007).

[15] J. F. Asmus, Non-divestment laser applications in art conservation, J Cult. Herit., 4 (SUPPL. 1), 289-293 (2003).

[16] E. L. Von Aderkas, M.M. Barsan, D.F.R. Gilson, I.S. Butler, Application of photoacoustic infrared spectroscopy in the forensic analysis of artists' inorganic pigments, Spectrochim. Acta A, 77 (5), 954 (2010).

[17] J. L. Jimenez-Perez, J. Jimenez-Perez, A.B. Cruz, A. Cruz-Orea, J.G. Mendoza-Alvarez, Photoacoustic analysis of pigments from archeological ceramics, Int. J. Thermophys., 25 (2), 503 (2004).

[18] G. J. Tserevelakis, I. Vrouvaki, P. Siozos, K. Melessanaki, K. Hatzigiannakis, C. Fotakis, G. Zacharakis, Photoacoustic imaging reveals hidden underdrawings in paintings, Sci. Rep.,7(1), 747, (2017).

[19] G. J. Tserevelakis, A. Dal Fovo, K. Melessanaki, R. Fontana, G. Zacharakis, Photoacoustic signal attenuation analysis for the assessment of thin layers thickness in paintings, J. Appl. Phys. 123, 123102-9 (2018) doi:10.1063/1.5022749.

[20] A. Dal Fovo, G. J. Tserevelakis, A. Papanikolaou, G. Zacharakis, R. Fontana, Combined photoacoustic imaging to delineate the internal structure of paintings, Opt. Letters 44, 4, pp. 919-922 (2019) https://doi.org/10.1364/OL.44.000919.

[21] L. V. Wang, H.-I Wu, Biomedical Optics: Principles and Imaging, J. Biomed. Opt., Book Review, 13, 4 (2008).

[22] G. J. Tserevelakis, M. Tsagkaraki, G. Zacharakis, Hybrid photoacoustic and optical imaging of pigments in vegetative tissues, Journal of Microscopy, 263(3), 300-6 (2016) doi:10.1111/jmi.12396.

[23] X. M. Yang, E.W. Stein, S. Ashkenazi, L.H.V. Wang, Nanoparticles for photoacoustic imaging, Wiley Interdiscip. Rev. Nanomed. Nanobiotechnol., 1(4), 360–8 (2009).

[24] B. E. Treeby, B.T. Cox, Progress in Biomedical Optics and Imaging - Proceedings of SPIE 7177, 717716 (2009).

[25] S. R. Cherry, R.D. Badawi, J. Qi, Essentials of In Vivo Biomedical Imaging, CRC Press, Boca Raton, FL, USA, 105 (2016).

[26] X. L. Deán-Ben, D. Razansky, V. Ntziachristos, The effects of acoustic attenuation in optoacoustic signals, Phys.Med. Biol., 56, 18, 6129 (2011).

[27] H. Ammari, E. Bretin, V. Jugnon, A. Wahab, Photoacoustic imaging for attenuating acoustic media, Mathematical modeling in biomedical imaging II, Springer, Heidelberg, Germany (2012).

[28] H. Ammari, E. Bretin, J. Garnier, A. Wahab, Time reversal in attenuating acoustic media. Mathematical and statistical methods for imaging, American Mathematical Society, Providence, RI, USA (2011).

[29] P. E. Bloomfield, Experimental study of the acoustical properties of polymers utilized to construct PVDF ultrasonic transducers and the acousto-electric properties of PVDF and P(VDF/TrFE) films, IEEE Trans. Ultrason. Ferroelectr. Freq. Control., 47 (6), 1397 (2000).

[30] B. Champagne, V. Liégeois, F. Zutterman, Pigment violet 19–a test case to define a simple method to simulate the vibronic structure of absorption spectra of organic pigments and dyes in solution, Photochem. Photobiol. Sci., PPS, 14 (2), 444 (2015).

[31] J. Yao and L.V. Wang, Photoacoustic Microscopy, Laser Photon. Rev. 7(5), 1-36, (2013) doi:10.1002/lpor.201200060.

[32] L. A. Goldberg, A Fresh Face for Samuel Gompers: Methyl Cellulose Poultice Cleaning, AIC, 28(1), 19-29 (1989).

[33] C. A. Baker, Methylcellulose and sodium carboxymethylcellulose: an evaluation for use in paper conservation through accelerated aging, Stud. Cons., 29, 55 (1984).

[34] A. Casoli, A., Z. Di Diego, C. Isca, Cleaning painted surfaces: evaluation of leaching phenomenon induced by solvents applied for the removal of gel residues, Environ. Sci. Pollut. R., 21(23), 13252 (2014) doi:10.1007/s11356-014-2658-5.

[35] P. Baglioni, E. Carretti, D. Chelazzi, Nanomaterials in Art Conservation, Nature Nanotech., 10(4), 287 (2015).

[36] P. Baglioni, D. Berti, M. Bonini, E. Carretti, L. Dei, E. Fratini, R. Giorgi, Micelle, microemulsions, and gels for the conservation of cultural heritage, Adv. Colloid Interface Sci., 205, 361-371 (2014).

[37] Y. Wang, C. Li, R.K. Wang, Noncontact photoacoustic imaging achieved by using a low-coherence interferometer as the acoustic detector, Opt. Letters, 36(20), 3975 (2011).

[38] A. Hochreiner, J. Bauer-Marschallinger, P. Burgholzer, B. Jakoby, T. Berer, Non-contact photoacoustic imaging using a fiber based interferometer with optical amplification, Biomed. Opt. Express, 4(11), 2322 (2013).

[39] X. L. Deán-Ben, G.A. Pang, F. Montero De Espinosa, D. Razansky, Non-contact optoacoustic imaging with focused air-coupled transducers, Appl. Phys. Letters, 107(5), 051105 (2015) doi:10.1063/1.4928123.

Conclusions and perspectives

In this research, the applicability of NonLinear Optical techniques (MPEF, THG and SHG) for in-depth analysis of wood, protectives, consolidants and paint layers was demonstrated, and the reliability of thickness measurements was verified by comparison with OCT analysis. Despite the advantages offered by OCT – e.g. possibility to measure larger areas and/or longer profiles (up to 2.5 cm with the prototype used) with respect to the few mm length of the NLOM acquisitions, availability of portable devices, signal detection in backward configuration – its application is confined to low scattering and semi-transparent materials, thus hampering the analysis of real painted objects and strongly reflecting varnishes. By contrast, NLOM has proven capable of probing opaque paints laid over different support materials and covered by protectives, enabling cross-sectional measurements with micrometric resolution. Another significant advantage of non-linear microscopies (SHG, THG, MPEF) is that they can be applied jointly to provide complementary information (morphological, structural, compositional) on the analysed material in one single measurement, with the use of a femtosecond laser as excitation source. The benefit of such a multi-modal approach adds up to the non-destructive nature of NLOM, which is crucial in artworks diagnosis.

THG cross-sectional images obtained through THG resulted directly comparable with OCT tomograms, both enabling the micrometric thickness measurement of transparent materials (protectives and glues) basing on the visualization of the interfaces. Nevertheless, being the detection of THG signals favoured in the forward configuration, further research must be carried out to explore the possibility of backward detection in order to expand its application on paintings and other non-transparent materials.

Combined MPEF and SHG measurements were applied successfully on wood samples for the visualization of microstructures and for the discrimination of NL signal emitters (i.e. lignin emitting nonlinear fluorescence, cellulose and starch generating second harmonic signal). One perspective is to perform polarization-resolved SHG imaging to determine the orientation of cellulose microfibrils and to improve their visibility in cell walls. Future applications of MPEF/SHG are planned for the analysis of wood deterioration on real artworks, as well as for the recognition of different wood species based on the visualization of their micro-morphology.

Concerning MPEF application to painting layers, it was observed that, despite the severe drop of the signal intensity with increasing depth and the different transmission properties of the superimposed materials (varnish and paint), the evaluation of the stratigraphy with micrometric precision is feasible, provided a proper interpretation of the nonlinear fluorescence response. Moreover, the possibility to perform MPEF measurement in the reflection mode enlarges its applicability to a wide range of real cases – i.e. painting materials laying on opaque substrates (board, wood, canvas, etc.) – also for in situ studies.

It was also demonstrated that through the combined application of well-established (linear) and the new (nonlinear) optical techniques it is possible to obtain chemical and physical information on a variety of artistic materials, without endangering the integrity of the artworks. Each technique provides information that can be used both to address other investigations and to complement further results.

Next step will be the systematic assessment of the damage thresholds for MPEF analysis on painting materials in view of its application on real paintings. The effects of the high-intensity laser pulses can be assessed by comparing the optical properties of the analysed surface before and after the irradiation – i.e. changes in the reflectance behaviour (through FORS), fluorescence emission

(LIF) and photoacoustic generation after light absorption (PAcSAI) – besides the monitoring of induced morphological and chemical variations by means of microscope analysis and micro-Raman spectroscopy.

PhotoAcoustic Signal Attenuation Analysis (PAAcSAA) and Imaging (PAcSAI) were proven effective for the in-depth thickness measurement of acrylic paint laid on glass cover-slips and canvas support. The quality of the results, verified by comparison with OCT, suggests the high potential of PAcSAI in the diagnosis of artworks. It was also demonstrated that the combination of PAcSAI and Near Infrared PhotoAcoustic Imaging (NIR-PAI) represents a promising diagnostic tool for the analysis of painted artworks. The possibility of high-resolution imaging to disclose the underdrawing, as well as stratigraphic information on paint layers, using the same setup, turns definitely useful in case of conservation studies and restoring operations. A comprehensive study on the PAcSAI of mixed paint layers constitutes a future research work, which will demonstrate the potential of this novel modality in cultural heritage diagnostics.

To ensure the efficient transmission of the laser-induced ultrasound signals in real case study, an alternative to water-based media or medium-free approach can be found, by using non-contact interferometric ultrasonic detectors or air-coupled transducers of high efficiency. The detailed evaluation of these contactless acoustic detection methods and their integration in an upgraded setup constitute future targets for this research. The development of a portable device is as well envisaged to enable in situ measurements on real artworks.

Appendix 1. Instrumentation: Linear optical techniques

Micro-Raman Spectroscopy

Raman spectra were collected using a Ranishaw InVia 0310-02 System based on a continuous Nd:YAG laser excitation source at 532 nm that illuminated the surface of the paint layer with a spot diameter of 1 μm. The system, equipped with a Leica microscope and an electrically refrigerated CCD camera, has a wavenumber resolution of 4 cm^{-1}. Measurements were performed with 10 s acquisition time and low laser power (0.15 – 0.3 mW) to prevent any sample damage.

Fibre Optics Reflectance Spectroscopy (FORS)

FORS spectra were acquired with a Zeiss Multi-Channel Spectrometer, including a MCS 521 VIS NIR-extended module and a MCS 511 NIR 1.7 module with spectral sensitivity in the 304 - 1100 nm and 950 - 1700 nm ranges, with spectral resolution of 3.2 nm and 6.0 nm, in the visible and IR region, respectively. The illumination/observation geometry is 45°/0°. For measurements, each sample was placed on a 100 % reflecting background (Spectralon) and each spectrum was averaged over three acquisitions from each of three measurements points that were selected for each sample (9 acquisitions per point). The output signal was processed through a dedicated software, providing also CIEL*a*b* coordinates with standard D65 illuminant and 2° observer.

Laser Induced Fluorescence (LIF)

LIF analysis was performed with a Q-switched Nd:YAG laser (15 ns pulse duration, and 1 Hz repetition rate) working at its 4th harmonic 266 nm. The luminous emission was collected and dispersed by a 0.30 m spectrograph with a

300 lines/mm grating (TMc300, Bentham) coupled to an intensified CCD (2151, Andor Technologies). The temporal gate (width of 3 μs) was fixed at zero time delay with respect to the arrival of the laser pulse to the surface of the sample.

Vis-NIR Scanning Multispectral Reflectography (Vis-NIR SMR)

The transparency of the different materials was investigated by means of the Multi-spectral Vis–NIR Scanner developed by the INO Heritage Science Group for in situ analysis. The scanner works in the visible (380 – 750 nm, 20 – 30 nm spectral resolution) and in the Near Infrared (750 – 2500 nm, 50 – 100 nm spectral resolution) regions, providing simultaneously single-point spectral data, and high-definition monochromatic images of the entire analysed surface. The 32 images (16 Vis + 16 NIR images are acquired with 250 μm spatial sampling. An autofocus system[xxiv] keeps the optimal target-lens distance during the entire scanning, providing a set of perfectly overlapping monochromatic images free from metrical aberrations.

Optical Coherence Tomography (OCT)

OCT analysis was performed using two different devices, a time-domain (Td) confocal-OCT and a spectral-domain (Sd) OCT.

Time-domain (Td)-confocal OCT

The Td confocal-OCT is a prototype developed at the Istituto Nazionale di Ottica (CNR-INO) - CH Group, combining an aspheric collimator made of two lenses with OCT setup (Fig. 1). The source consists of two coupled superluminescent light-emitting diodes (SLED) with central wavelength λ = 1550 nm and 100 nm bandwidth). The 50/50 fiber optic coupler, which splits

[xxiv] P. Targowski *et al.*, Laser Chemistry 2006, Article ID 35373 (2006).

the beam into two beams of equal intensity, acts as beam splitter in the standard Michelson interferometer configuration. The signal is collected by the detector (InGaAs photodiode), amplified, filtered, and converted into digital format (8 bit image). After proper calibration, the instrument characteristics are the following: axial resolution 10 μm in air and lateral resolution 2.5 μm, working distance 3 mm and working range 1 mm.

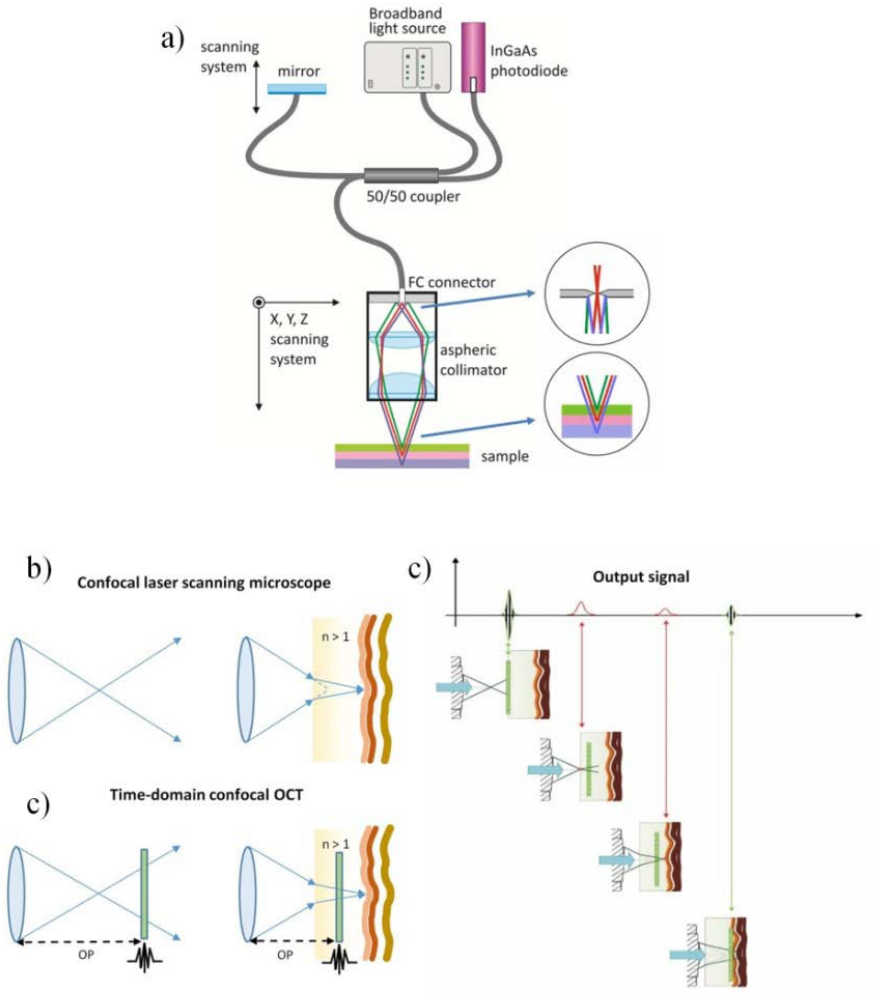

Fig. 1. (a) Schematics of the confocal-OCT prototype; (b) changes in the radiation optical path (OP) in confocal microscopy and in Td-confocal OCT; (c) schematic representation of the output signal in confocal-OCT.

Spectral-domain (Sd) OCT

In spectral-domain OCT systems the detector consists of a spectrograph equipped with a diffraction grating and a fast camera. The spectrum of the light source is modulated by interference fringes of frequency corresponding to the position of the reflective or scattering layer in the object: the deeper the layer, the higher the modulation frequency.[xxiv] Information, encoded in the frequency signal, is decoded by Fast Fourier Transformation (FFT). The device used in this study is a Thorlabs Telesto-II (Fig. 2), equipped with a superluminescent diode (central wavelength: 1300 nm and about 170 nm of bandwidth) with axial resolution of 5.5 µm in air, lateral resolution of 7 µm and 3.5 mm imaging depth. The system is controlled via 64-bit software preinstalled on a high-performance computer. The 3D scanning path probe with integrated video camera allows for high-speed imaging (76 kHz) for rapid volume acquisition and live display. The sample stage provides XY translation and rotation of the sample along with axial travel of the probe.

Fig. 2. Spectral-Domain OCT Thorlabs Telesto-II during measurements.

Appendix 2. Instrumentation: Nonlinear optical techniques

Nonlinear microscope developed at CNR-INO (Italy)

The setup consists of a custom-made laser-scanning nonlinear microscope for Multi-Photon Excitation Fluorescence (MPEF), Second and Third Harmonic Generation (SHG and THG) and Fluorescence Lifetime Imaging Microscopy (FLIM). The device, originally developed for biological applications at CNR-INO,[xxv] was implemented and upgraded during the three-years research. The excitation source used for the first measurement campaign was a mode-locked Ti:Sapphire laser (Mira 900 F, Coherent Inc., CA, US). The beam was focused on the specimen by a 20x objective (Nikon Plan Apo, NA 0.75 Air). A narrow band-pass filter centred at 370 ± 10 nm (HQ420BP, Chroma Technology Corporation) was used for the detection of SHG signal. The excitation wavelength was set to 740 nm, with a pulse duration of 120 fs and a repetition rate of 80 MHz, with a power of about 5 mW on the specimen. Nonlinear signals from the sample were detected by two different systems, for intensity and lifetime images, respectively (Fig. 1). Nonlinear fluorescence intensity data were acquired using a photomultiplier tube (Hamamatsu H7422), with a 190-900 nm spectral sensitivity, by assigning to each pixel an intensity value (grey level) proportional to the amount of fluorescence photons reaching the detector from each surface point scanned by the laser. TPEF images were acquired with a field of view of 200×200 μm^2, a resolution of 512×512 pixel, z-step of 2 μm for an acquisition time of about 5 sec. Using ImageJ (National Institutes of Health, Bethesda, VA, US) *Orthogonal Views* plug-in, 3D reconstructions from the stacks were obtained.

FLIM was performed using a fast photon-counting detector (Becker & Hickl PMH-100), with 400 – 600 nm spectral sensitivity.

[xxv] R. Mercatelli *et al.*, J. Biophotonics, 10 75–83 (2017).

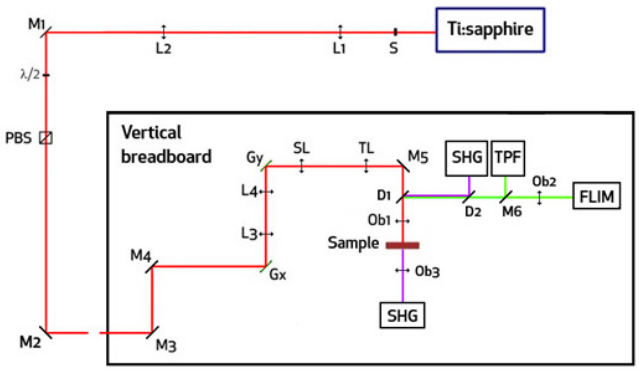

Fig. 1. Scheme of the experimental setup of the laser-scanner nonlinear microscope: laser source (Ti:Sapphire), optics (L 1 – 4, lens; TL, tube lens; SL, scanning lens; M 1 – 6, mirrors; Ob 1 – 3, shutters; Gx, Gy, galvanometric mirrors) and detection system (SHG, TPF, FLIM detectors).

The output data – i.e. the decay curves and the related FLIM images – are reconstructed pixel-by-pixel from individual time measurements. Based on Time-Correlated Single-Photon Counting (TCSPC) principle, the arrival time of the individual photons is recorded with respect to the excitation pulse. Data processing and display are performed by means of SPC-Image software (Becker & Hickl GmbH, Germany). The SPC-Image is coded in a false-colour scale image, in which each point represents the average fluorescence lifetime calculated through mono, bi- or tri-exponential fit of the related fluorescence decay curve, which can be visualized positioning the cursor in points of interest on the image.

Finally, a fast 16-channel photon counting photomultiplier (PML-16C Becker & Hickl GmbH) provides 16 fluorescence decay curves at 16 different narrow spectral bands for each point of the FLIM image. In this mode, the emitted light is sent to a spectrograph, it reaches the 16-channel photomultiplier with a transit time spread typical value of 150 ps, and then it is processed by the FLIM (Fluorescence Lifetime Imaging Microscopy) apparatus. Therefore, for each

point of the measured area, 16 FLIM images are provided, containing the xy maps of the fluorescence decay, which are recorded with a spectral resolution of 12,5 nm within 400-600 nm spectral detection range, thus enabling the detection of specific emitting molecular species.

The final measurement campaign was performed with the last upgrade version of the setup, comprising an Optical Parametric Oscillator (OPO) pumped by a Yb-based fiber fs-laser (Camaleon Discovery, Coherent Inc., Santa Clara, CA, US, Fig. 2), with dual output: the first, tunable, ranging between 660 to 1320 nm excitation wavelength, 100 fs pulse duration, 80 MHz repetition rate; the second, fixed at 1040 nm (140 fs pulse duration, 80 MHz repetition rate).

Fig 2. Dual output tunable femtosecond laser Chamaleon Discovery - Santa Clara, CA (https://www.coherent.com, 27/08/2018).

The beam is focused onto the specimen by a 40x objective (Zeiss Apochromat, NA 0.95, air immersion). A motorized stage enables the movement of the specimen on the xy plane. The movement of the focus in Z direction is achieved with a digitally controlled piezo-objective scanner system (PIFOC®), with 400 μm travel range. The signal is collected in backward direction, passing through the same objective of the incident beam, and/or in forward direction by a second objective (Nikon Fluor 40x, NA 0.8, water immersion). A 665 nm long-pass filter is placed in front of the first objective enabling the transmission of the excitation wavelength (800-1040 nm). The MPEF and SHG signals coming from the sample are instead reflected by the filter and directed to the

photomultiplier (Hamamatsu Photonics, Photosensor module H7422-40, high-sensitivity range 300-720 nm, sensitivity peak at 580 nm).
Images were acquired with a field of view of 200×200 μm^2 or 100×100 μm^2, depending on the area, as an average of 10 acquisitions, with a resulting resolution of 256×256 pixels, z-step of 1 μm. 3D reconstructions from stacks were obtained with ImageJ (National Institutes of Health, Bethesda, VA, US) *Orthogonal Views* plug-in. Z-profiles were extracted from each stacks in order to measure the thickness of the analysed material.

Nonlinear microscope developed at IQFR-CSIC (Spain)

The second setup used is a modified nonlinear microscope developed at IQFR-CSIC (Spain), which allows for the collection of the MPEF signals from the focal volume at the sample plane in the reflection mode. The setup is depicted in Fig. 3. The excitation light source is a mode-locked Ti:Sapphire femtosecond laser emitting at 800 nm, with average power of 680 mW, releasing 70 fs pulses at a repetition rate of 80 MHz. A variable neutral density filter (NDC-50C-2M, Thorlabs) was used to control the laser power reaching the sample. The laser beam was focused on the sample by a microscope objective lens (M Plan Apo HL 50X, Mitutoyo, NA 0.42) by using a dichroic beam splitter (FF750-SDi02-25x36, Semrock) with high reflection at 800 nm. The laser focal plane was selected with motorized translation xyz stages (Standa 8MVT100-25-1 for XY and Standa 8MTF for Z). The lateral and in-depth resolutions are 1 and 2 μm, respectively. A Lab View interface was used to control both scanning and data acquisition procedures. The MPEF signals were collected in the backward direction through the microscope objective lens and a beam splitter (70/30) and measured using a photomultiplier tube (9783B, ET Enterprises) connected to a lock-in amplifier (SR810 DSP, Stanford Research Systems) to ensure high

amplification and signal-to-noise ratio. A short pass filter (335-610 nm, Thorlabs FGB37S) was placed at the entrance of the photomultiplier to cut off the reflected laser light. The remaining 30% of the MPEF signal was sent to a CCD camera (Thorlabs DCC1645C) for online visualization of the sample surface and the signal collection process. For the measurements, the average power was in the range of 1-15 mW to ensure absence of damage on the paint layers.

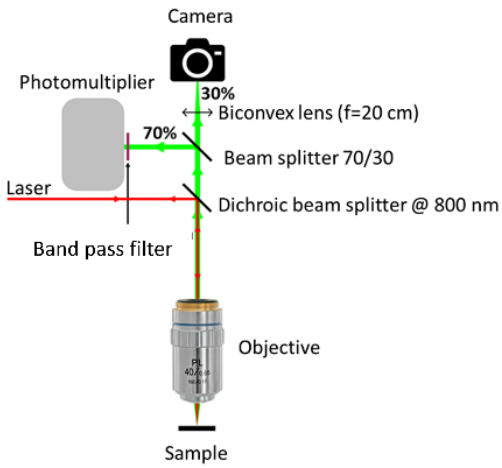

Fig. 3. Layout of the nonlinear optical microscope used for MPEF measurements.

Nonlinear microscope developed at IESL-FORTH (Greece)

The instrument used for THG analysis is a custom-built laser scanning microscope (Fig. 4) developed at the Nonlinear microscopy Laboratory at FORTH. The excitation source is a fs laser (T-Pulse, Amplitude) with central wavelength 1028 nm, repetition rate 50 MHz, 800 mW power, pulse duration 200 fs. A modified Nikon upright microscope (Eclipse ME600D) is used as a platform for the imaging system. The radiation intensity is attenuated through a set of neutral density filters (ND) and a 20x, 0.8 NA objective lens (O, Carl Zeiss, Plan Apochromat, 0.55 mm working distance, air immersion) is used for

tight focusing the beam, whereas a 100X, 1.4 NA condenser lens (Carl Zeiss, Plan Apochromat, 0.17 mm working distance, oil immersion) is used for collecting the forward-propagating THG signals (C). Multi-photon excitation florescence microscopy can be also performed, being MPEF signal simultaneously collected in reflection mode by the objective lens of the microscope using a dichroic mirror (DM). The scanning is performed with a pair of galvanometric mirrors (GM), (CambridgeTech.6210H) and the focal plane is selected with a motorized translation stage (Standa 8MT167-100). THG and MPEF signals are detected with two sensitive photomultiplier tubes (PMT Hamamatsu H9305-04), following spectral filtering using suitable bandpass optical filters (F1, F2) to cut off the reflected laser light and solely detect nonlinear signals from the sample.

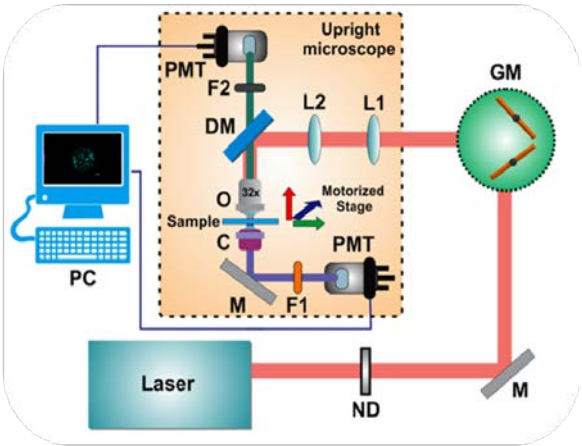

Fig. 4. Nonlinear microscopy setup for THG and MPEF measurements: neutral density filters (ND); mirror (M), galvo mirrors (GM), lenses (L1, L2), dichroic mirror (DM), short pass filter (F2), objective (O), sample (S), condenser lens (C), photomultiplier (PTM), personal computer (PC).

List of Acronyms

1PEF: One-Photon Excitation Fluorescence

2DSD: Second Derivative Spline Distance

2PEF: Two-Photon Excitation Fluorescence

3PEF: Three-Photon Excitation Fluorescence

AFP: Actual Focus Position

ATF: Average Transmitted Frequency

CB: Cobalt Blue

CBH: Cobalt Blue Hue

CeB: Cerulean Blue

CH: Cultural Heritage

CML: Compound Middle Lamella

CR: Cadmium Red

CRM: Confocal Raman Microscopy

Cu-Pc: Copper Phthalocyanines

CY: Cadmium Yellow

FFT: Fast Fourier Transformation

FORS: Fibre Optics Reflectance Spectroscopy

FWHM: Full Width at Half Maximum

IB: Indanthrene Blue

IC: Internal Conversion

IEM-CSIC: Instituto de Estructura de la Materia – Consejo Superior de Investigaciones Cientificas

IESL–FORTH: Institute of Electronic Structure and Laser – Foundation for Research and Technology Hellas

IPERION: Integrated Platform for the European Research Infrastructure ON Cultural Heritage

IQFR–CSIC: Instituto de Quimica Fisica Rocasolano – Consejo Superior de Investigaciones Cientificas

IRF: Instrument Response Function

IS: Iridescent Silver

ISC: Inter-System Crossing

LIBS: Laser Induced Breakdown Spectroscopy

LIF: Laser Induced Fluorescence
LY: Lemon Yellow
MAP: Maximum Amplitude Projection
MPEF: Multi-Photon Excitation Fluorescence
NFP: Nominal Focus Position
NIR: Near Infrared
NIR-PAI: Near Infrared - PhotoAcoustic Imaging
NLOM: Nonlinear Optical Microscopies
NMR: Nuclear Magnetic Resonance
OA: Opto Acoustics
OCT: Optical Coherence Tomography
PA: Photo Acoustics
PAcSAA: PhotoAcoustic Signal Atteuation Analysis
PAcSAI: PhotoAcoustic Signal Attenuation Imaging
PAS: PhotoAcoustic Spectroscopy
PB: Phthalo Blue
PBC: Primary Blue Cyan
PBL: Permanent Blue Light
PG: Phthalo Green
PGL: Permanent Green Light
PMMA: Poly-Metil-Metacrylate
PRM: Primary Red Magenta
PSF: Point Spread Function
PVAc: Poly-Vinyl Acetate
SHG: Second Harmonic Generation
SNR: Signal-to-Noise Ratio
THG: Third Harmonic Generation
TW: Titanium White
UB: Ultramarine Blue
VDB: Van Dyke Brown
Vis-NIR SMR: Visible-Near Infrared Scanning Multispectral Reflectography
XRF: X-Ray Fluorescence
ZW: Zinc White

List of publications related to the PhD research

A. Dal Fovo, G. J. Tserevelakis, A. Papanikolaou, G. Zacharakis, R. Fontana, Combined photoacoustic imaging to delineate the internal structure of paintings, Opt. Letters 44, 4, pp. 919-922 (2019) https://doi.org/10.1364/OL.44.000919.

A. Dal Fovo, M. Oujja, M. Sanz, A. Martínez-Hernández, M. V. Cañamares, M. Castillejo, R. Fontana, "Multianalytical non-invasive characterization of phthalocyanine acrylic paints through spectroscopic and non-linear optical techniques", Spectrochimica Acta A, Molecular and Biomolecular Spectroscopy, Elsevier, 208, 262-270, https://doi.org/10.1016/j.saa.2018.09.040, 2018.

G. J. Tserevelakis, A. Dal Fovo, K. Melessanaki, R. Fontana, G. Zacharakis, "Photoacoustic signal attenuation analysis for the assessment of thin layers thickness in paintings", Journal of Applied Physics, 123, 123102, https://doi.org/10.1063/1.5022749, 2018.

J. Striova, C. Ruberto, M. Barucci, J. Blažek, D. Kunzelman, A. Dal Fovo, E. Pampaloni, R. Fontana, "Spectral Imaging and Archival Data in Analysing Madonna of the Rabbit Paintings by Manet and Titian", Angewandte Chemie, Int. Ed. 2018, 57,7408 –7412; Special Issue: Heritage Science Plus Analytical Chemistry, Spectroscopy and Bioanalysis, 7408-7412, https://doi.org/10.1002/anie.201800624, 2018.

J. Striova, A. Dal Fovo, V. Fontani, M. Barucci, E. Pampaloni, M. Raffaelli, R. Fontana, "Modern acrylic paints probed by Optical Coherence Tomography and Infrared Reflectography", Microchemical Journal, 138 65-71, https://doi.org/10.1016/j.microc.2017.12.027, 2018.

S. R. Amato, A. Burnstock, M. Cross, K. Janssens, F. Rosi, L. Cartechini, R. Fontana, A. Dal Fovo, M. Paolantoni, C. Grazia, A. Romani, A. Michelin, C. Andraud, A. Tournié, J. Dik, "Interpreting technical evidence from spectral imaging of paintings by Édouard Manet in The Courtauld Gallery", X Ray Spectrometry, 1-11, https://doi.org/10.1002/xrs.2828, 2018.

A. Dal Fovo, R. Fontana, J. Striova, E. Pampaloni, M. Barucci, M. Raffaelli, R. Mercatelli, L. Pezzati, R. Cicchi, "Nonlinear optical imaging techniques (NLO) for painting investigation", Lasers in the Conservation of Artworks XI, Proceedings of LACONA XI, P. Targowski et al. (Eds), NCU Press Torun, doi: 10.12775/3875-4.10, 2017.

Presentations to conferences in the framework of the PhD research

Lacona 12th Conference, Lasers in the Conservation of Artworks (10th -14th September 2018, Paris, France)
Oral presentation: "Multianalytical characterization of phthalocyanine acrylic paints through spectroscopic, interferometric and non-linear optical microscopy techniques", Dal Fovo A., Oujja M., Sanz M., Martínez-Hernández A., Cañamares M.V., Castillejo M., Fontana R.
Oral presentation: "Listening to laserlight interactions with objects of art: a novel photoacoustic diagnostic approach", Tseverelakis G., Dal Fovo A., Tsagkaraki M., Vrouvaki I., Siozos P., Melessanaki K., Fontana R., Pouli P., Zacharakis G.

European Material Research Society (E-MRS) Spring Meeting and Exhibit (18th -22nd June 2018, Strasbourg, France)
Oral presentation: "Multiphoton excitation fluorescence microscopy for non-destructive analysis of painting substrates", Dal Fovo A., Martínez-Hernández A., Sanz M., Oujja M., Fontana R., Castillejo M.

AIAr Italian Association of Archeometry, Thematic Conference on Cultural Heritage (8th-10th March 2017, Florence, Italy)
Oral presentation: "Non-linear techniques for the disclosure of paintings internal structure", Dal Fovo A., Striova J., Barucci M., Raffaelli M., Pampaloni E., Cicchi R., Mercatelli R., Quercioli F., Fontana R.

INO Annual Symposium 2017- Shedding light on the quantum world (8th-10th February 2017, National Institute of Optics, Trento, Italy)
Oral presentation: "Non-linear techniques for the disclosure of paintings internal structure", Dal Fovo A., Striova J., Barucci M., Raffaelli M:, Pampaloni E., Cicchi R., Mercatelli R., Quercioli F., Fontana R.

Lacona 11th Conference, Lasers in the Conservation of Artworks (19th-23th September 2016, Krakow, Poland)
Oral presentation: "Non-linear imaging techniques (NLO) for painting investigation", Dal Fovo A., Striova J., Barucci M., Raffaelli M., Pampaloni E., Cicchi R., Mercatelli R., Quercioli F., Fontana R.
Oral presentation and poster: "Thinning oxalate patina with Er:YAG laser stand-alone and in combination with Agar and Carbogel systems", Dal Fovo A., Striova J., Raffaelli M., Felici A., Barucci M.,Pampaloni E., Marconi E., Fontana R.

1st Annual Meeting Iperion CH, Integrated Project for the European Research Infrastructure on Cultural Heritage (12nd-15th April 2016, Berlin, Germany)
Advanced non-linear imaging microscopy for the Cultural Heritage. Oral presentation: "Task 6.1 Preparation of painting samples".

Acknowledgements

The research leading to these results was funded by the EU Community's H2020 Research Infrastructure program under the Parthenos Project (GA 654119), IPERION CH Project (GA 654028) and by H2020 Laserlab Europe – Transnational Access (EC-GA 654148).

I would like to thank my supervisor, Raffaella Fontana, for having believed in me in this 3-years work. Thanks for supporting me, for giving me many opportunities and for teaching me a lot, both in professional and human terms.

I sincerely thank Marta Castillejo and the whole group of IQFR-CSIC, Mohamed Oujja, Mikel Sanz, Alejandro Martinez-Hernandez, for the beautiful and enriching experience I lived in Madrid and for the rewarding collaboration work.

I would like to thank George Tserevelakis of IESL-FORTH for the relevant and fruitful work collaboration and for the time spent together in Crete. Special thanks to Vassilis Tsafas for the valuable contribution to this thesis in THG measurements. Many thanks to George Filippidis, Giannis Zacharakis, Paraskevi Pouli for the LaserLab project at FORTH.

Thanks to all the staff of the National Institute of Optics, especially to the CH Group, i.e. Jana Striova, Marco Barucci, Enrico Pampaloni, Marco Raffaelli.

Many thanks to Riccardo Cicchi, Raffaella Mercatelli, Enrico Baria, Sara Mattana, and Marco Marchetti, for the nonlinear microscopy measurements, and to Franco Quercioli and Vincenzo Greco for the advices on the interpretation of the MPEF results.

Thanks to the staff of the Opificio delle Pietre Dure and in particular to Alberto Dimuccio for the help in the realization of the wooden supports and the samples' cases.